# COUPLED ELECTROMAGNETIC AND DEVICE LEVEL INVESTIGATIONS OF METAL-INSULATOR-SEMICONDUCTOR INTERCONNECTS

A DISSERTATION

SUBMITTED TO THE PROGRAM IN SCIENTIFIC COMPUTING AND

COMPUTATIONAL MATHEMATICS

AND THE COMMITTEE ON GRADUATE STUDIES

OF STANFORD UNIVERSITY

IN PARTIAL FULFILLMENT OF THE REQUIREMENTS

FOR THE DEGREE OF

DOCTOR OF PHILOSOPHY

Gaofeng Wang

February 2001

I certify that I have read this dissertation and that in my opinion it is fully adequate, in scope and quality, as dissertation for the degree of Doctor of Philosophy.

Robert W. Dutton, Principal Advisor

I certify that I have read this dissertation and that in my opinion it is fully adequate, in scope and quality, as dissertation for the degree of Doctor of Philosophy.

S. Simon Wong

I certify that I have read this dissertation and that in my opinion it is fully adequate, in scope and quality, as dissertation for the degree of Doctor of Philosophy.

Umran S. Inan

Approved for the University Committee on Graduate Studies:

# ABSTRACT

Due to dense, large IC chips with higher clock rates, effects of on-chip interconnects are becoming a limiting factor to the performance of integrated circuits. Metal-insulator-semiconductor (MIS) interconnects are the most fundamental component in the modern integrated circuits. Their electrical performance is of critical importance. Slow-wave properties and electronic controllability of such interconnects can also be employed to reduce the size and cost of distributed elements used in radio frequency applications to implement delay lines, variable phase shifters, voltage-tunable filters, etc. On the other hand, interconnect effects such as losses, dispersion, and substrate noise and nonlinearity may degrade both analog and digital circuit performance.

Most existing approaches for analysis of MIS interconnects are solely based on using Maxwell’s equations with the semiconductor substrate modeled as a lossy medium. The nonlinear nature of semiconductor substrate has been generally ignored by previous research. In order to understand the physical mechanisms behind effects such as field-carrier interactions, substrate noise, semiconductor nonlinearity, losses, dispersion, slow-wave behavior, and external bias dependence, it is necessary to describe the semiconductor as nonlinear solid state plasma. In this thesis, device level frequency domain (DLFD) simulation is proposed for studying wave propagation along MIS interconnects. Based on these device level simulations, a rigorous circuit extraction scheme is then developed for modeling MIS interconnects. An energy-based approach is used to establish equivalence between DLFD simulation results and the equivalent circuit model.

Nonlinearity of semiconductor substrates is included by combining the motion equations of charged carriers and Maxwell’s equations. The set of combined nonlinear equations is then transformed into the frequency domain, which leads to sets of nonlinear equations for the fundamental mode and its harmonics. Finally, the sets of nonlinear equations in the frequency domain are discretized using the finite element method and solved using Newton’s iterations. Special numerical enhancements are implemented to speed up the computational convergence and handle the boundary layer nature of the problem under study. This device level simulation provides knowledge on field-carrier interactions, semiconductor substrate losses and nonlinearity, as well as slow-wave, external bias, and screening effects of charged carriers. In particular, this device level simulation enables a rigorous full wave study of nonlinearity effects that arise from semiconductor substrates.

Based on the device level simulation results, a rigorous circuit model of MIS interconnects is extracted using an energy-based approach. This new equivalent circuit model consists of an equivalent transmission line, which mimics the energy transport characteristics of the actual MIS interconnect. Moreover, the new equivalent circuit model, which retains information about the semiconductor substrate effects obtained from the device level simulation, provides a generalized nonlinear and electronically tunable circuit model, suitable for both small-signal and large-signal analyses.

Numerical examples for practical material and geometrical parameters are included to illustrate capabilities and efficiency of both the proposed device level simulation and circuit extraction schemes. Good agreement is observed between the results obtained from the proposed schemes and those from the measurements or the published data from previous research.

# ACKNOWLEDGMENTS

I would like to express my deep gratitude to my advisor, Professor Robert W. Dutton, for his guidance, inspiration, support, and enthusiasm through all my years at Stanford. Conversations with him have always been stimulating and enlightening, and are the sources of new ideas and creative thoughts.

I am deeply indebted to Professor Gene Golub and Professor George Papanicolaou for their supports and personal generosity, in addition to the wonderful lectures that they gave us in the classes.

I would like to thank Professors Simon Wong, Umran Inan, and James Harris for being on the committees and spending precious time on reading my dissertation.

I am very glad to have the privilege of knowing and working with many current and former members of Dutton's TCAD group. I am deeply indebted to Dr. Zhiping Yu for many productive technical discussions as well as personal advice. I am also deeply indebted to Dr. Conor Rafferty at Bell Laboratories for many good suggestions to my research.

I am deeply grateful to Professor Jiechang Hou and Professor Deguang Feng at Wuhan Univeristy for initially introducing me into the kingdom of scientific research.

I am grateful to Professors Walter Murray, Andrew Stuart, and Joseph Oliger for their dedication to students in the SCCM program. I am indebted to Fely Barrera and Evelyn Boughton for their administrative assistance and many enjoyable chats.

I would like to thank my fellow students in both the TCAD group and the SCCM program for their friendships: Ian Mitchell, Nhat Nguyen, Ron Yu, Xiaoning Qi, James Yang, Dan Yergeau, Yong Sun, Krist Buschelman, Edward Chan, Yi-Chang Lu, Xin-Yi Zhang, and SoYoung Kim.

Finally, I am deeply indebted to my family: my parents, Xiaoqing, and Wavelet for their loves, supports, and patience.

# DEDICATION

To the people who have loved, inspired, and supported me through all the years

# TABLE OF CONTENTS

# LIST OF TABLES

# LIST OF FIGURES

*Number* *Page*

# CHAPETR 1: INTRODUCTION

Section 1.1 gives a survey on the related research work and elucidates motivation for the current research. Section 1.2 outlines how this dissertation is organized.

## 1.1: BACKGROUND AND MOTIVATIONS

Electrical performance of on-chip interconnects is increasingly important for high-speed integrated circuits. As the circuit density steadily increases, the operating frequencies and clock rates get higher, and the die size has also been increasing, effects of on-chip interconnects become limiting factors to the overall circuit performance [1, 2]. The device performance improves with each new chip generation. On the other hand, the higher level of integration brings more and longer wiring interconnections on the chip. On-chip wiring delays are now a significant portion of the total chip delay. Interconnect effects such as loss, dispersion, substrate noise, and semiconductor nonlinearity all can degrade the performance of integrated circuits.

Metal-insulator-semiconductor (MIS) interconnects, being one of the most elementary components in the modern integrated circuits, have been of fundamental interest. Slow-wave propagation in MIS and Schottky-contact interconnects has been both experimentally observed and theoretically explained from different points of view [3-21]. The slow-wave properties and electronic controllability of such interconnects can be employed to reduce the size and cost of distributed elements to implement delay lines, variable phase shifters, voltage-tunable filters, etc [7-10, 22-24]. On the other hand, energy dissipation in both semiconductor layers and conductor lines can have a significant impact on performance of MIS interconnects [25, 26]. Moreover, the nonlinear nature of semiconductor substrate may degrade quality of electrical signals and introduce unwanted signal waveform distortions. In order to understand mechanisms behind various effects such as substrate noise, semiconductor nonlinearity, slow-wave effect, loss, and dispersion, it is necessary to accurately simulate the MIS interconnect structures.

Analytical or empirical lumped circuit models [4, 6, 11, 26-28] have been used to provide fast calculation and first-hand insight to the performance of MIS interconnects. However, they are applicable to only a few simplified problems and provide limited information about the inhomogeneous and distributed nature of MIS interconnects. Nevertheless, the lumped circuit models can be employed to initialize more powerful numerical algorithms.

More accurate analysis of MIS interconnects requires the solution of the electromagnetic field problems. Numerical schemes for electromagnetic simulation of MIS interconnects include: the mode-matching method [29-31], the spectral domain analysis (SDA) method [30, 32-35], the method of lines [35], the transmission line matrix (TLM) method [36], the finite-difference time-domain (FDTD) method [37], and the finite element method [38-40]. In these purely electromagnetic simulation models, the semiconductor effects are accounted for simply by virtue of conductivity or complex dielectric constant of the semiconductor material.

When an electromagnetic wave propagates along the MIS interconnect, screening effects of the charged carriers prohibit the electromagnetic field from penetrating deep into the semiconductor, in addition to the attenuation arising from energy dissipation. In order to describe the behavior of the semiconductor as solid state plasma, the motion equations of charged carriers should be included directly in the simulation [41]. In other words, a formula combining the motion equations of charged carriers and Maxwell’s equations is required in the device level simulation in order to include the interactions between the electromagnetic field and the charged carriers in semiconductor.

In [42], the propagation property of the fundamental mode in a biased parallel-plate MIS waveguide was investigated using a transport-based analysis. A formulation incorporating Maxwell's equations and the motion equations of charged carriers was first linearized and then solved using the finite difference scheme. The approach in [42] enabled the investigation of carrier accumulation and depletion under the influence of an external dc bias as well as the screening effect of charged carriers. The approach in [42] is, however, applicable only to small-signal analysis due to its linearization of the equations.

The nonlinear nature of the semiconductor substrates has been generally ignored in most previous work. The question of when to include the semiconductor nonlinearity, however, has not been answered quantitatively. In order to address the nonlinear characteristics of the carrier motion equations, more comprehensive simulations are required.

To construct equivalent circuit models for the interconnects, a contour integral based approach has been widely employed (e.g., [7, 17, 43]). Integrals of the electromagnetic fields over appropriate contours are used as a convenient definition of voltage and current. These definitions of voltage and current are valid, however, only for TEM waves. When losses are important, the presence of a longitudinal electric field implies that the transverse field components no longer satisfy the static equations. Thus, the definitions for voltage and current in terms of contour integrals of the field components become invalid. In [44], an energy-based approach has been proposed, which abandons the approach based on intuitively chosen contour integrals. Rather, it builds an equivalent circuit model based on power equivalence between the circuit model and the original waveguide.

In this work, a device level simulation based on Maxwell's equations and the motion equations of charged carriers is first presented to study the propagation characteristics of MIS interconnects. The nonlinearity in the motion equations of charged carriers is preserved and included in the simulation. Thus, this approach is suitable for both small-signal and large-signal analyses. In order to provide a fast and robust simulation, advanced numerical algorithms such as finite element discretization, sparse matrix scheme, matrix balancing, and multi-dimensional Newton's iterations are utilized. Unlike the iterative algorithm in [42], where the equations were sequentially and separately solved at each iteration, this approach solves all the equations simultaneously, which reduces the number of iterations considerably. In addition, the boundary layer nature of the set of equations under study will be manifested theoretically and treated in a numerically consistent manner. This approach is able to provide detailed insight to field-carrier interactions, semiconductor substrate losses and nonlinearity, and slow-wave, external bias, and screening effects of charged carriers.

Based on the device level simulation, a rigorous circuit model of MIS interconnects is then established. The energy-based approach is employed to construct the equivalent circuit model from the device level simulation results. The equivalent circuit model retains information about the semiconductor substrate effects obtained from the device level simulation. The nonlinearity in the motion equations is preserved in the simulation, which makes the equivalent circuit model a generalized nonlinear and electronic tunable circuit model suitable for both small-signal and large-signal analyses. Moreover, the model provides formulae for the entire frequency-conductivity domain, valid across a wide range of frequencies and substrate doping.

## 1.2: OUTLINE

Chapter 2 introduces the basic theory for analysis of MIS interconnects by virtue of electromagnetic theory and semiconductor physics. Maxwell's equations govern the electromagnetic fields, whereas the concentrations of charged carriers are determined by their motion equations. Formulae for analyzing MIS interconnects are established by combining Maxwell’s equations and the motion equations of charged carriers. Both the time-domain and frequency-domain formulae are developed.

Chapter 3 presents the device level frequency domain (DLFD) simulation scheme for studying the characteristics of wave propagation along MIS interconnects. This device level simulation is based on the general frequency domain formulae established in Chapter 2. By virtue of the finite element scheme and multi-dimensional Newton’s method, the wave propagation characteristics, electromagnetic fields, and carrier concentrations are solved from the frequency domain formulae under appropriately specified boundary conditions. The nonlinearity in the motion equations of carriers is preserved and included in the simulation.

Chapter 4 develops a rigorous equivalent circuit model for MIS interconnects based on the device level simulation results. The energy-based approach is employed to construct the equivalent circuit model, which results in a generalized nonlinear and electronic tunable model suitable for both small-signal and large-signal analyses.

Chapter 5 describes the computer software realization for device level frequency domain (DLFD) simulation as well as the extraction of equivalent circuit models.

Numerical results are presented in Chapter 6 to validate the computer software implementations and demonstrate capabilities of the device level simulation scheme as well as the circuit model extraction. The numerical results are compared with both the measurements and the previously published data. Chapter 6 also reveals some new characteristics of MIS interconnects, which can be studied only by the device level approach.

Chapter 7 gives a brief summary of contributions from the current research and suggestions for future work.

# CHAPTER 2: BASIC THEORY

In this chapter, the theory for analysis of MIS interconnects is introduced based on general electromagnetic theory (e.g., [45-49]) and semiconductor physics (e.g., [50-52]). Propagation properties of electrical signals along MIS interconnects can be investigated in a microscopic level through field-carrier interactions between electromagnetic fields and charged carriers in the semiconductor substrate. Maxwell's equations govern the electromagnetic fields, whereas the activities of charged carriers are determined by their motion equations. Formulae for analyzing MIS interconnects are established by combining Maxwell's equations and the motion equations of the charged carriers.

The field-carrier interactions, by very nature, induce nonlinear phenomena. The set of coupled electromagnetic and carrier transport equations is essentially nonlinear. The nonlinearity can introduce signal distortions which in turn can be represented by a series of harmonics in the frequency domain. In this chapter, the frequency domain formulae for the harmonic representation of the problem are developed.

## 2.1: MAXWELL'S EQUATIONS

The basic equations of electromagnetic theory are represented by Maxwell's equations. Maxwell's equations are fundamental laws governing the behavior of electromagnetic fields (e.g., [45-49]). In a homogeneous medium, Maxwell's equations take the following form:

$$\nabla \times \mathbf{E}(\mathbf{r},t) = -\mu \frac{\partial \mathbf{H}(\mathbf{r},t)}{\partial t} \tag{2.1a}$$

$$\nabla \times \mathbf{H}(\mathbf{r},t) = \varepsilon \frac{\partial \mathbf{E}(\mathbf{r},t)}{\partial t} + \mathbf{J}(\mathbf{r},t) \qquad (2.1b)$$

$$\nabla \cdot \mathbf{E}(\mathbf{r},t) = \frac{\rho(\mathbf{r},t)}{\varepsilon} \qquad (2.1c)$$

$$\nabla \cdot \mathbf{H}(\mathbf{r},t) = 0 \qquad (2.1d)$$

where **E** and **H** are, respectively, the electric and magnetic fields, **J** is the conduction current density, $\rho$ is the (net) electric charge density, and $\varepsilon$ and $\mu$ are, respectively, the permittivity and permeability of the medium.

Equation (2.1d) can be viewed as a direct consequence of (2.1a), whereas (2.1b) and (2.1c) imply the current continuity:

$$\nabla \cdot \mathbf{J}(\mathbf{r},t) + \frac{\partial \rho(\mathbf{r},t)}{\partial t} = 0 \qquad (2.2)$$

Therefore, the set of independent equations from Maxwell's equations consists of (2.1a), (2.1b), and (2.2).

Maxwell's equations are essentially a mathematical description on how the electromagnetic fields are generated from sources $\rho$ and **J**. In order to completely determine an electromagnetic problem, one also needs to provide a quantitative measure on how charged particles in a material medium act under electromagnetic fields. The constitutive relations, which macroscopically characterize a material medium and describe how the material medium responses to electromagnetic fields, are usually employed to supplement Maxwell's equations.

Alternatively, a microscopic description on the motion of charged particles can be utilized with Maxwell's equations for advanced microscopic analysis on field-particle interactions, which can be expected to provide more detailed information and insight into the problem under study.

## 2.2: MOTION EQUATIONS OF CHARGED CARRIERS

The motion of charged particles results in electric current. The current density of charged particles is the product of the charge quantity per particle, the particle concentration, and the statistically averaged drift velocity of the particles. There are two types of charged carriers in semiconductor materials, i.e., positively charged holes and negatively charged electrons.

In a semiconductor medium, the motion of charged carriers is governed by the following carrier transport equations (e.g., [50-52]):

$$\tau_n \frac{\partial \mathbf{J}_n(\mathbf{r},t)}{\partial t} + \mathbf{J}_n(\mathbf{r},t) = q\mu_n \, n(\mathbf{r},t)\mathbf{E}(\mathbf{r},t) + qD_n \, \nabla n(\mathbf{r},t) \tag{2.3a}$$

$$\tau_p \frac{\partial \mathbf{J}_p(\mathbf{r},t)}{\partial t} + \mathbf{J}_p(\mathbf{r},t) = q\mu_p \, p(\mathbf{r},t)\mathbf{E}(\mathbf{r},t) - qD_p \, \nabla p(\mathbf{r},t) \tag{2.3b}$$

where $p$ and $n$ are, respectively, the hole and electron densities and used in the following as subscripts for quantities related to hole and electron. $\mathbf{J}_n$ and $\mathbf{J}_p$ are the current densities, $\mu_n$ and $\mu_p$ are the effective carrier mobilities, $D_n$ and $D_p$ are the diffusion coefficients, and $\tau_n$ and $\tau_p$ are the average collision times. The elementary charge is given by $q$.

In a semiconductor medium, the electric charge density is given by

$$\rho(\mathbf{r},t) = q\left[p(\mathbf{r},t) - n(\mathbf{r},t) + N(\mathbf{r})\right] \tag{2.4}$$

where $N$ denotes the net doping distribution, which is, respectively, positive or negative for the relative excess of donors or acceptors. Moreover, the total conduction current density is the sum of the electron and hole current densities:

$$\mathbf{J}(\mathbf{r},t) = \mathbf{J}_n(\mathbf{r},t) + \mathbf{J}_p(\mathbf{r},t) \tag{2.5}$$

Considering relations (2.4) and (2.5), the current continuity equation (2.2) is usually written as two equations in terms of $\mathbf{J}_n$ and $\mathbf{J}_p$ as follows:

$$\frac{\partial n(\mathbf{r},t)}{\partial t} = \frac{1}{q}\nabla \cdot \mathbf{J}_n(\mathbf{r},t) - u(\mathbf{r},t) \tag{2.6a}$$

$$\frac{\partial p(\mathbf{r},t)}{\partial t} = -\frac{1}{q}\nabla \cdot \mathbf{J}_p(\mathbf{r},t) - u(\mathbf{r},t) \tag{2.6b}$$

where $u(\mathbf{r},t)$ is the total net recombination rate of electrons and holes.

## 2.3: COUPLED ELECTROMAGNETIC AND CARRIER TRANSPORT EQUATIONS

By combining Maxwell's equations, the carrier transport equations, and the current continuity equations, a set of coupled equations is obtained for solving electromagnetic fields and carrier concentrations in a semiconductor medium.

In summary, equations (2.1a), (2.1b), (2.3a), (2.3b), (2.6a), and (2.6b) lead to a set of coupled electromagnetic and carrier transport equations. This set of coupled equations, along with properly specified boundary conditions, can completely determine the electromagnetic fields and carrier concentrations in a semiconductor material, and thus forms the basic time domain formulae for analyzing MIS interconnect structures.

## 2.4: FREQUENCY DOMAIN FORMULATION

The nonlinear terms $n \cdot \mathbf{E}$ and $p \cdot \mathbf{E}$ in the time-domain formulation introduce signal distortion, which consists of various harmonics in the frequency domain. For a guided wave propagating along the $z$ direction, the fundamental component of an arbitrary variable $v(\mathbf{r},t)$ takes the form $v^{(1)}(x,y)\,e^{-\gamma z + j\omega t}$, where $\omega$ denotes the fundamental (angular) frequency and $\gamma$ represents the propagation factor. Therefore, the product of two fundamental mode quantities $v_1^{(1)}(x,y)e^{-\gamma z + j\omega t}$ and $v_2^{(1)}(x,y)e^{-\gamma z + j\omega t}$ will result in a second harmonic quantity $v_1^{(1)}(x,y)v_2^{(1)}(x,y)e^{-2\gamma z+j2\omega t}$ , and so on. In general, a *(m+n)*-th harmonic quantity $v_1^{(m)}(x,y)v_2^{(n)}(x,y)e^{-(m+n)\,\gamma z+j(m+n)\omega t}$ can be generated from the product of an *m*-th harmonic quantity $v_1^{(m)}(x,y)e^{-\,m\gamma z+jm\omega t}$ and an *n*-th harmonic quantity $v_2^{(n)}(x,y)e^{-n\,\gamma z+jn\omega t}$ .

The above procedure can be rigorously formulated by virtue of Fourier analysis. A guided nonlinear wave $v(\mathbf{r},t)$, propagating along the *z* direction, takes the generalized form as follows:

$$v(\mathbf{r},t)=\tilde{v}\left(x,y,\,t-\frac{z}{\upsilon}\right) \qquad (2.7a)$$

where $\upsilon$ denotes the propagation velocity that is a function of the fundamental frequency. Moreover, $v(\mathbf{r},t)$ is a periodic function with respect to *t* and the period is equal to $2\pi/\omega$. Hence, (2.7a) can be mathematically expanded in terms of Fourier series as follows:

$$v(\mathbf{r},t)=v^{(0)}(x,y)+\sum_{m=1}^{\infty}v^{(m)}(x,y)\cdot e^{-m\gamma z}\cdot e^{jm\omega t} \qquad (2.7b)$$

where $v^{(0)}(x,y)$ denotes the steady state solution, i.e., the static component, $v^{(1)}(x,y)$ is the fundamental mode, and $v^{(m)}(x,y)$ (*m* > *1*) represents the *m*-th harmonic component of the variable under consideration. In a linearized problem, all the higher order harmonics vanish and only the fundamental mode is considered. Thus, the nonlinear wave reduces to a monotonic wave. For a general nonlinear problem, however, all the higher order harmonics can be nonzero and should be included in the analysis.

The harmonics in the expansion (2.7b) should not be confused with the nonlinear wave itself at multiples of the fundamental frequency. The nonlinear wave could exist for the entire frequency range, whereas the harmonics occur only at multiples of the fundamental frequency. Moreover, the harmonics can not exist without the presence of the fundamental mode as the excitation source, that is, the harmonics can not stand alone by themselves. On the other hand, the nonlinear wave can exist in its own right. The propagation factor $\gamma$ that characterizes the propagation property of the nonlinear wave is generally a nonlinear function of the frequency. Therefore, the propagation factor $\gamma(\varpi)|_{\varpi=m\omega}$ of the nonlinear wave at $\varpi = m\omega$ is usually unequal to $m\gamma(\omega)$ and irrelevant to the *z* dependence factor $e^{-m\gamma z}$ of the *m*-th harmonic in the expansion (2.7b).

Substitution of the form (2.7b) into the time domain formulae leads to

$$\begin{aligned}\nabla^2 E_z^{(m)}(x,y)+m^2\left(k^2+\gamma^2\right)E_z^{(m)}(x,y)= {} & jm\omega\mu\left[J_{nz}^{(m)}(x,y)+J_{pz}^{(m)}(x,y)\right]\\ & -\frac{qm\gamma}{\varepsilon}\left[p^{(m)}(x,y)-n^{(m)}(x,y)\right]\end{aligned} \tag{2.8a}$$

$$\begin{aligned}\nabla^2 \mathbf{E}_{xy}^{(m)}(x,y)+m^2\left(k^2+\gamma^2\right)\mathbf{E}_{xy}^{(m)}(x,y)= {} & jm\omega\mu\left[\mathbf{J}_{nxy}^{(m)}(x,y)+\mathbf{J}_{pxy}^{(m)}(x,y)\right]\\ & +\frac{q}{\varepsilon}\nabla\left[p^{(m)}(x,y)-n^{(m)}(x,y)\right]\end{aligned} \tag{2.8b}$$

$$jm\omega n^{(m)}(x,y)=\frac{1}{q}\nabla\cdot\mathbf{J}_{nxy}^{(m)}(x,y)-\frac{m\gamma}{q}J_{nz}^{(m)}(x,y)-u^{(m)}(x,y) \tag{2.9a}$$

$$jm\omega\, p^{(m)}(x,y)=-\frac{1}{q}\nabla\cdot\mathbf{J}_{pxy}^{(m)}(x,y)+\frac{m\gamma}{q}J_{pz}^{(m)}(x,y)-u^{(m)}(x,y) \tag{2.9b}$$

$$\begin{aligned}\left(1+jm\omega\tau_n\right)\mathbf{J}_n^{(m)}(x,y)= {} & q\mu_n\sum_{s=0}^{m}\left[n^{(s)}(x,y)\mathbf{E}^{(m-s)}(x,y)\right]\\ & +qD_n\nabla n^{(m)}(x,y)-\hat{\mathbf{z}}\,qD_n m\gamma\, n^{(m)}(x,y)\end{aligned} \tag{2.10a}$$

$$\begin{aligned}\left(1+jm\omega\tau_p\right)\mathbf{J}_p^{(m)}(x,y)= {} & q\mu_p\sum_{s=0}^{m}\left[p^{(s)}(x,y)\mathbf{E}^{(m-s)}(x,y)\right]\\ & -qD_p\nabla p^{(m)}(x,y)+\hat{\mathbf{z}}\,qD_p m\gamma\, p^{(m)}(x,y)\end{aligned} \tag{2.10b}$$

and

$$jm\omega \mathbf{H}^{(m)}(x,y) = -\frac{1}{\mu}\left[\nabla \times \mathbf{E}^{(m)}(x,y) + \hat{\mathbf{x}} m\gamma E_y^{(m)}(x,y) - \hat{\mathbf{y}} m\gamma E_x^{(m)}(x,y)\right] \tag{2.11}$$

where $k = \omega\sqrt{\mu\varepsilon}$ is wave number in the medium, $\mathbf{J}_{xy}^{(m)}(x,y) = \hat{\mathbf{x}} J_x^{(m)}(x,y) + \hat{\mathbf{y}} J_y^{(m)}(x,y)$, and $\mathbf{E}_{xy}^{(m)}(x,y) = \hat{\mathbf{x}} E_x^{(m)}(x,y) + \hat{\mathbf{y}} E_y^{(m)}(x,y)$. During the derivation of (2.8a) and (2.8b), the magnetic field has been eliminated from (2.1a) and (2.1b), and the divergence equation is exploited as follows:

$$\nabla \cdot \mathbf{E}_{xy}^{(m)}(x,y) - m\gamma E_z^{(m)}(x,y) = \frac{q}{\varepsilon}\left[p^{(m)}(x,y) - n^{(m)}(x,y)\right] \tag{2.12}$$

Theoretically, (2.8a) and (2.8b) are the equations needed for determining the electrical field components. However, numerical analysis of (2.8a) and (2.8b) may lead to spurious solutions [53-56], which fail to satisfy the divergence condition (2.12).

In a numerical analysis such as the finite element method the basis functions for expanding the unknowns are merely required to be continuous but not differentiable. Hence, a numerical solution satisfies the governing differential equations only in a weak sense. Due to the lack of sufficient differentiability, the implication of (2.12) by (2.8a) and (2.8b) no longer holds. As a consequence, a weak solution of (2.8a) and (2.8b) may not meet the divergence condition (2.12). Such a weak solution is called a spurious solution. To prevent spurious solutions, it is a common practice to explicitly incorporate the divergence condition (2.12) into the basic equation (2.8b) during the course of numerical analysis.

The complete formulae in the frequency domain consist of equations (2.8a), (2.8b), (2.9a), (2.9b), (2.10a), (2.10b), and (2.11). Careful examination on these equations reveals that any given harmonic depends on the lower order harmonics only. Therefore, the harmonics can be recursively evaluated from a lower order harmonic to a higher order harmonic, starting from the static solution.

The solution to the static equations can be readily attained using the standard approach [51, 52], in which a scalar potential $\phi$ is introduced through $\mathbf{E}^{(0)} = -\nabla\phi$ and solved along with the static carrier concentrations $n^{(0)}$ and $p^{(0)}$. The external bias has a significant impact on the static solution, which in turn affects the fundamental mode and high order harmonics.

## 2.5: SUMMARY

In this chapter, the basic theory for analysis of MIS interconnects has been established upon electromagnetic theory and semiconductor physics. In order to investigate field-carrier interactions between electromagnetic fields and charged carriers, semiconductor substrates have been described as solid state plasmas. Maxwell’s equations govern the electromagnetic fields, whereas the activities of charged carriers are determined by their motion equations. By combining Maxwell’s equations and the motion equations of charged carriers, device level formulae for analyzing MIS interconnects were developed.

The nonlinearity in the motion equations gives rise to signal distortions, which are best studied using harmonics in the frequency domain. By using Fourier analysis, the frequency domain formulae for various harmonics have been derived from the time domain formulae. The frequency domain formulae possess a nice property that any given harmonic depends on the lower order harmonics only. Hence, the frequency domain formulae can be recursively solved in a manner from a lower order harmonic to a higher order harmonic, starting from the static solution.

# CHAPTER 3: DEVICE LEVEL SIMULATION OF WAVE PROPAGATION

In this chapter, a device level frequency domain (DLFD) simulation is presented to study the wave propagation along MIS interconnects. This device level simulation is based on the general frequency domain formulae established in the preceding chapter. By virtue of the finite element scheme and multi-dimensional Newton’s method, the wave propagation characteristics, electromagnetic fields, and carrier concentrations are solved from the frequency domain formulae under appropriately specified boundary conditions.

The nonlinearity in the motion equations of charged carriers is preserved and included in the simulation. Thus, this approach is suitable for both small-signal and large-signal analyses. In order to provide a fast and robust simulation, advanced numerical algorithms such as the finite element discretization, sparse matrix scheme, matrix balancing, and multi-dimensional Newton’s iterations are utilized. Moreover, the boundary layer nature of the equations under study will be manifested theoretically and treated in a numerically consistent manner. This approach is able to provide detailed information on field-carrier interactions, semiconductor substrate loss and nonlinearity, slow-wave behavior, external bias dependence, screening effect of charged carriers.

## 3.1: BASIC EQUATIONS FOR MIS WAVEGUIDE STRUCTURES

Figure 3.1 illustrates a typical MIS interconnect structure, which consists of a strip conductor, thin insulation layer, the semiconductor substrate, and the ground plane. In practice, the insulator layer is very thin so that edge effects of the strip conductor can be neglected. For simplicity, the interconnect is modeled as a parallel-plate waveguide structure for the device level simulation (see Figure 3.2).

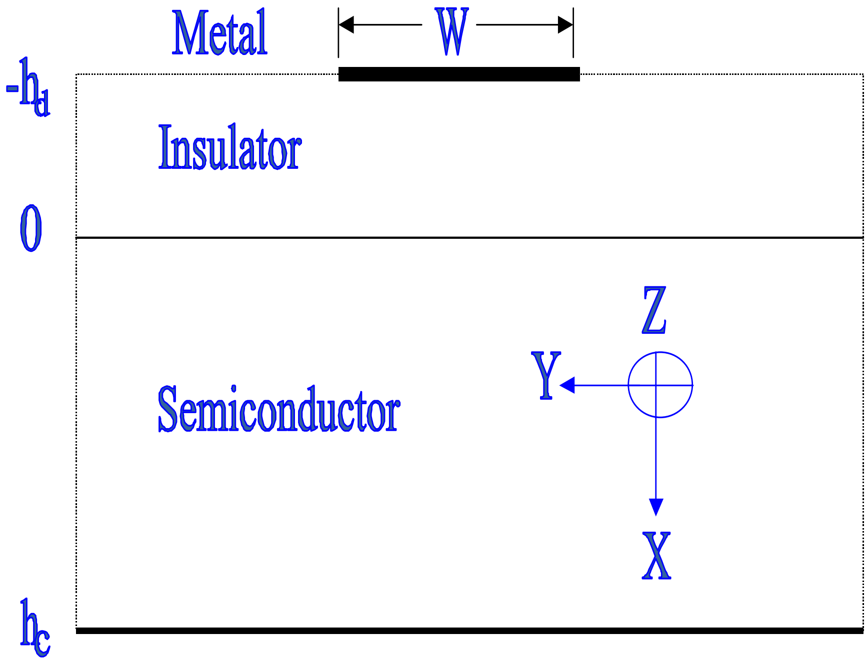

Figure 3.1: Configuration of an MIS interconnect structure

The parallel-plate waveguide structure extends from $y = -\infty$ to $y = \infty$. All physical quantities are assumed to be uniform in the $y$ direction. Moreover, the dominant mode in a parallel-plate waveguide is a transverse magnetic (TM) mode [46, 48, 49]. For TM modes, the magnetic field has only a $y$ component, whereas the electric field has no $y$ component as implied by (2.11). Hence, equations (2.8a), (2.8b), (2.9a), (2.9b), (2.10a), (2.10b), and (2.11) lead to

$$\frac{\partial^2 E_z^{(m)}(x)}{\partial x^2} + m^2\left(k_c^2 + \gamma^2\right)E_z^{(m)}(x) = jm\omega\mu\left[J_{nz}^{(m)(r)}(x) + J_{pz}^{(m)(r)}(x)\right] - \frac{qm\gamma}{\varepsilon}\left[p^{(m)}(x) - n^{(m)}(x)\right] \tag{3.1a}$$

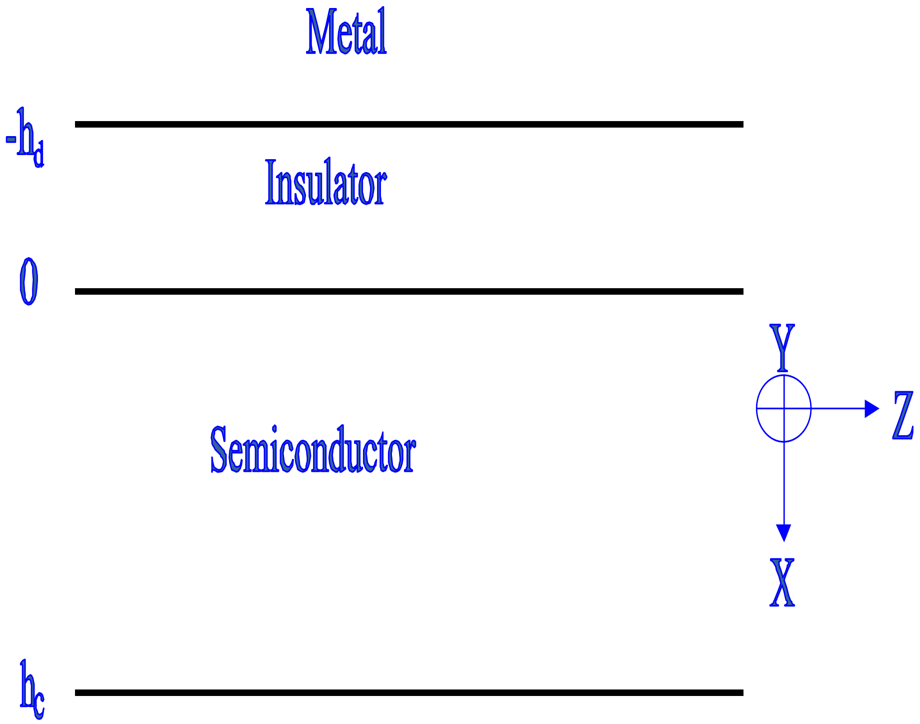

Figure 3.2: Configuration of a parallel-plate waveguide model

$$jm\omega n^{(m)}(x) = \frac{1}{q}\frac{\partial J_{nx}^{(m)}(x)}{\partial x} - \frac{m\gamma}{q}J_{nz}^{(m)}(x) - u^{(m)}(x) \tag{3.1b}$$

$$jm\omega\, p^{(m)}(x) = -\frac{1}{q}\frac{\partial J_{px}^{(m)}(x)}{\partial x} + \frac{m\gamma}{q}J_{pz}^{(m)}(x) - u^{(m)}(x) \tag{3.1c}$$

and

$$E_x^{(m)}(x) = -\frac{m\gamma}{m^2\left(k^2+\gamma^2\right)}\frac{\partial E_z^{(m)}(x)}{\partial x} + \frac{jm\omega\mu}{m^2\left(k^2+\gamma^2\right)}\left[J_{nx}^{(m)}(x) + J_{px}^{(m)}(x)\right] \tag{3.1d}$$

$$H_y^{(m)}(x) = \frac{1}{jm\omega\mu}\left[\frac{\partial E_z^{(m)}(x)}{\partial x} + m\gamma E_x^{(m)}(x)\right] \tag{3.1e}$$

where

$$\left(1 + jm\omega\tau_n\right)\mathbf{J}_n^{(m)(0)}(x) = q\mu_n\, n^{(0)}(x)\mathbf{E}^{(m)}(x) \tag{3.2a}$$

$$\left(1 + jm\omega\tau_p\right)\mathbf{J}_p^{(m)(0)}(x) = q\mu_p\, p^{(0)}(x)\mathbf{E}^{(m)}(x) \tag{3.2b}$$

$$\begin{aligned}\left(1 + jm\omega\tau_n\right)\mathbf{J}_n^{(m)}(x) = q\mu_n \sum_{s=0}^{m}\left[n^{(s)}(x)\mathbf{E}^{(m-s)}(x)\right] + qD_n\,\nabla n^{(m)}(x) \\ - \hat{\mathbf{z}}\, qD_n m\gamma\, n^{(m)}(x)\end{aligned} \tag{3.2c}$$

$$\begin{aligned}\left(1 + jm\omega\tau_p\right)\mathbf{J}_p^{(m)}(x) = q\mu_p \sum_{s=0}^{m}\left[p^{(s)}(x)\mathbf{E}^{(m-s)}(x)\right] - qD_p\,\nabla p^{(m)}(x) \\ + \hat{\mathbf{z}}\, qD_p m\gamma\, p^{(m)}(x)\end{aligned} \tag{3.2d}$$

$$\mathbf{J}_n^{(m)(r)}(x) = \mathbf{J}_n^{(m)}(x) - \mathbf{J}_n^{(m)(0)}(x), \quad \mathbf{J}_p^{(m)(r)}(x) = \mathbf{J}_p^{(m)}(x) - \mathbf{J}_p^{(m)(0)}(x) \tag{3.2e}$$

$$k_c^2 = k^2 - \frac{j\omega\mu\sigma^{(0)}(x)}{m}, \quad \sigma^{(0)}(x) = q\left[\frac{\mu_n n^{(0)}(x)}{1 + jm\omega\tau_n} + \frac{\mu_p p^{(0)}(x)}{1 + jm\omega\tau_p}\right] \tag{3.2f}$$

Equation (3.1d) is obtained by incorporating (2.12) into (2.8b), which is able to prevent spurious modes in the numerical solution.

## 3.2: BOUNDARY CONDITIONS

By accounting for the boundary condition $E_z^{(m)}(-h_d)=0$ at the metal surface, the field components in the dielectric layer can be obtained by solving equations (3.1a), (3.1d), and (3.1e) with $n^{(m)} = p^{(m)} = 0$ as follows:

$$E_z^{(m)}(x) = -\frac{A^{(m)}k_d}{\gamma}\sin[mk_d(x+h_d)] \tag{3.3a}$$

$$E_x^{(m)}(x) = A^{(m)}\cos[mk_d(x+h_d)] \tag{3.3b}$$

$$H_y^{(m)}(x) = \frac{j\omega\varepsilon_d A^{(m)}}{\gamma}\cos[mk_d(x+h_d)] \tag{3.3c}$$

where $\varepsilon_d$ and $\mu_d$ are, respectively, the permittivity and permeability of the dielectric layer, and $k_d = \sqrt{\omega^2\mu_d\varepsilon_d + \gamma^2}$. Note that $A^{(1)}$ is an arbitrary constant, depending on the excitation magnitude, while the $A^{(m)}\,(m>1)$ are coefficients to be determined.

Boundary conditions at the interface between the insulator and semiconductor are as follows:

$$E_z^{(m)}(0^+) = E_z^{(m)}(0^-) = -\frac{A^{(m)}k_d}{\gamma}\sin(mk_d h_d) \tag{3.4a}$$

$$H_y^{(m)}(0^+) = H_y^{(m)}(0^-) = \frac{j\omega\varepsilon_d A^{(m)}}{\gamma}\cos(mk_d h_d) \tag{3.4b}$$

$$J_{nx}^{(m)}(0) = J_{px}^{(m)}(0) = 0 \tag{3.4c}$$

The ground plane at $x = h_c$ is usually far away from the signal line, i.e., the value of $h_c$ is generally much larger than the Debye length. Hence, the ground plane may have little impact on the propagation characteristics. The boundary conditions on the ground plane are prescribed as

$$E_z^{(m)}(h_c) = 0 \tag{3.4d}$$

$$n^{(m)}(h_c) = p^{(m)}(h_c) = 0 \tag{3.4e}$$

For the fundamental mode, eliminating the arbitrary constant $A^{(1)}$ in (3.4a) and (3.4b) leads to

$$\frac{E_z^{(1)}(0^+)}{H_y^{(1)}(0^+)} = -\frac{k_d}{j\omega\varepsilon_d}\tan(k_d h_d) \tag{3.5}$$

Note that $k_d$ is a function of the propagation factor $\gamma$. Equation (3.5) provides a nonlinear algebraic equation for determining the propagation factor $\gamma$. Given an excitation magnitude $A^{(1)}$, equations (3.1a), (3.1b), (3.1c), (3.1d), (3.1e) and (3.5), along with boundary conditions given by equations (3.4a), (3.4c), (3.4d) and (3.4e), completely determine the field components, carrier concentrations, and propagation factor for the fundamental mode. Note that the boundary condition (3.4b) is automatically fulfilled, provided that (3.4a) and (3.5) are specified.

For higher order harmonics with $m > 1$, equations (3.4b) and (3.1e) are compatible only if one of the following conditions holds:

$$\frac{E_z^{(m)}(0^+)}{H_y^{(m)}(0^+)} = -\frac{mk_d}{jm\omega\varepsilon_d}\tan(mk_d h_d) \tag{3.6}$$

or

$$A^{(m)} = 0 \tag{3.7}$$

where the *m*-th harmonic components $E_z^{(m)}$ and $H_y^{(m)}$ are assumed to be the solution of equations (3.1a), (3.1b), (3.1c), (3.1d) and (3.1e) under the boundary conditions (3.4a), (3.4c), (3.4d) and (3.4e).

In general, the propagation factor $\gamma$, determined from (3.5), rarely meets the condition given by (3.6). Therefore, the condition (3.7) must be imposed as the condition for compatibility. This implies that higher order harmonics due to the semiconductor nonlinearity are confined within the semiconductor and do not penetrate into the insulator.

If the condition (3.6) happens to be satisfied, the solution would not be unique since any arbitrary $A^{(m)}$ could result in a solution, which is a phenomenal characteristic of shock waves or resonance. The reason for the resonance occurrence is because under the condition (3.6) the *m*-th harmonic is satisfying the identical set of equations as the fundamental mode at frequency $f^{(m)} = mf$. Physically, the local *m*-th harmonic contributions due to the semiconductor nonlinearity are able to propagate as fundamental mode waves along the waveguide and thus be summed in phase along their propagation paths to give rise to resonance.

Under the compatibility condition (3.7), equations (3.1a), (3.1b), (3.1c), (3.1d) and (3.1e) along with the boundary conditions (3.4a), (3.4c), (3.4d) and (3.4e) completely determine the *m*-th harmonic field components and carrier concentrations (where $m > 1$).

## 3.3: SOME OBSERVATIONS ON THE BASIC EQUATIONS

This section discusses some observations on the fundamental properties of the basic equations obtained in the preceding sections.

### 3.3.1: A NATURE OF BOUNDARY LAYER PROBLEMS

By careful examination on the set of equations established in the preceding sections, one can show that the problem under study exhibits a boundary layer nature. After substitution of expressions (3.2c) and (3.2d) for $J_{nx}^{(m)}$ and $J_{px}^{(m)}$, equations (3.1b) and (3.1c) contain the second-order derivatives $\partial^2 n^{(m)} / \partial x^2$ and $\partial^2 p^{(m)} / \partial x^2$ respectively. In equation (3.1b), the ratio between the coefficients of $\partial^2 n^{(m)} / \partial x^2$ and $n^{(m)}$ is roughly of the order of $L_{Dn}^2$, where $L_{Dn} = \sqrt{\varepsilon D_n / q n^{(0)} \mu_n}$ is the *n*-type Debye length. Similarly, in equation (3.1c), the ratio between the coefficients of $\partial^2 p^{(m)} / \partial x^2$ and $p^{(m)}$ is roughly of the order of $L_{Dp}^2$, where $L_{Dp} = \sqrt{\varepsilon D_p / q p^{(0)} \mu_p}$ is the *p*-type Debye length.

Note that the Debye length is generally much smaller than the dimension of the structure under consideration. Therefore, the highest derivative terms in (3.1b) or (3.1c) are negligible in comparison with the terms $n^{(m)}$ or $p^{(m)}$. Mathematically, either (3.1b) or (3.1c) results in a boundary layer problem [57, 58], which implies a solution with a fast decaying factor $e^{-x/L_{Dn}}$ or $e^{-x/L_{Dp}}$ within a very thin layer of the order of the Debye length. Physically, an accumulation-depletion layer of charged carriers appears in the semiconductor near the interface at $x = 0$.

### 3.3.2: LINEAR VERSUS NONLINEAR EQUATIONS

Since equations (3.1a), (3.1d), and (3.5) are nonlinear in $\gamma$, it is essentially a nonlinear system of equations for the fundamental mode. Nonlinear equation solvers are required for such a nonlinear system of equations.

Once the fundamental mode is determined, the propagation constant $\gamma$ is a known quantity. For high order harmonics, the equations turn out to be linear for all the unknowns and thus can be readily solved by linear equation solvers.

## 3.4: FINITE ELEMENT ANALYSIS

This section develops the weak formulation as well as the discretization for the problem under study. The finite element method (e.g., [59-62]) is utilized to accomplish the discretization task. Some special numerical considerations are also discussed.

### 3.4.1: AN ALTERNATIVE FORM OF EQUATIONS

The frequency domain formulae developed in preceding sections can be discretized using the standard finite element procedure (e.g., [59-62]). Before applying the finite element method, one can rewrite the formulae into a form more suitable for numerical analysis as follows:

$$\begin{aligned}\frac{\partial^2 E_z^{(m)}(x)}{\partial x^2} + m^2\left(k_c^2 + \gamma^2\right)E_z^{(m)}(x) - jm\omega\mu\left[J_{nz}^{(m)(r)}(x) + J_{pz}^{(m)(r)}(x)\right] \\ + \frac{qm\gamma}{\varepsilon}\left[p^{(m)}(x) - n^{(m)}(x)\right] = 0\end{aligned} \tag{3.8a}$$

$$m^2\left(k^2 + \gamma^2\right)E_x^{(m)}(x) + m\gamma\frac{\partial E_z^{(m)}(x)}{\partial x} - jm\omega\mu\left[J_{nx}^{(m)}(x) + J_{px}^{(m)}(x)\right] = 0 \tag{3.8b}$$

$$\begin{aligned}-\tilde{D}_n\frac{\partial^2 n^{(m)}(x)}{\partial x^2} - \tilde{D}_n m^2\gamma^2 n^{(m)}(x) + G_n^{(m)}(x) + jm\omega\, n^{(m)}(x) + u^{(m)}(x) \\ + \sum_{s=0}^{m} F_n^{(m,s)}(x) = 0\end{aligned} \tag{3.8c}$$

$$\begin{aligned}\tilde{D}_p\frac{\partial^2 p^{(m)}(x)}{\partial x^2} + \tilde{D}_p m^2\gamma^2 p^{(m)}(x) + G_p^{(m)}(x) - jm\omega\, p^{(m)}(x) - u^{(m)}(x) \\ + \sum_{s=0}^{m} F_p^{(m,s)}(x) = 0\end{aligned} \tag{3.8d}$$

where

$$H_y^{(m)}(x) = \frac{1}{jm\omega\mu}\left[\frac{\partial E_z^{(m)}(x)}{\partial x} + m\gamma E_x^{(m)}(x)\right] \tag{3.9a}$$

$$F_n^{(m,s)}(x) = \frac{\mu_n}{1+jm\omega\tau_n}\left\{-E_x^{(m-s)}(x)\frac{\partial n_s(x)}{\partial x} - n^{(s)}(x)\frac{q}{\varepsilon}c^{(m-s)}(x)\right\} \tag{3.9b}$$

$$F_p^{(m,s)}(x) = \frac{\mu_p}{1+jm\omega\tau_p}\left\{-E_x^{(m-s)}(x)\frac{\partial p_s(x)}{\partial x} - p^{(s)}(x)\frac{q}{\varepsilon}c^{(m-s)}(x)\right\} \tag{3.9c}$$

$$G_n^{(m)}(x) = \frac{\mu_n}{1+jm\omega\tau_n}\sum_{s=1}^{m} s\,\gamma\, n^{(s)}(x)\, E_z^{(m-s)}(x) \tag{3.9d}$$

$$G_p^{(m)}(x) = \frac{\mu_p}{1+jm\omega\tau_p}\sum_{s=1}^{m} s\,\gamma\, p^{(s)}(x)\, E_z^{(m-s)}(x) \tag{3.9e}$$

$$\tilde{D}_n = \frac{D_n}{1+jm\omega\tau_n} \tag{3.9f}$$

$$\tilde{D}_p = \frac{D_p}{1+jm\omega\tau_p} \tag{3.9g}$$

and the net carrier concentrations are given by

$$c^{(s)}(x) = \begin{cases} p^{(0)}(x) - n^{(0)}(x) + N(x) & \text{if } s = 0 \\ p^{(s)}(x) - n^{(s)}(x) & \text{otherwise} \end{cases} \tag{3.9h}$$

In the above formulae, there are four primary unknown functions $E_z^{(m)}$, $E_x^{(m)}$, $n^{(m)}$, and $p^{(m)}$ (besides the unknown propagation factor $\gamma$ when $m$ = 1). All these primary unknowns are tightly coupled and need to be solved simultaneously. Once the primary unknown functions are solved, the secondary unknown functions such as $H_y^{(m)}$ can be readily evaluated.

### 3.4.2: WEAK FORMULATION

Define a space $V = \{ v(x) \in C([0,h_c],\Re): v'(\cdot)$ is piecewise continuous and bounded on $[0,h_c]\}$ and denote the $L^2$ inner product

$$\langle u,v\rangle = \int_0^{h_c} u(x)v(x)dx \tag{3.10}$$

Then, the weak forms of (3.8a), (3.8b), (3.8c), and (3.8d) can be obtained as follows:

$$-\left\langle \frac{\partial E_z^{(m)}(x)}{\partial x}, \frac{\partial W_1^{(m)}(x)}{\partial x} \right\rangle + \left[ \frac{\partial E_z^{(m)}(x)}{\partial x} W_1^{(m)}(x) \right]_{x=0}^{x=h_c} + \left\langle Q_1^{(m)}(x), W_1^{(m)}(x) \right\rangle = 0 \tag{3.11a}$$

$$m^2\left(k^2+\gamma^2\right)\left\langle E_x^{(m)}(x), W_2^{(m)}(x)\right\rangle + \left\langle Q_2^{(m)}(x), W_2^{(m)}(x)\right\rangle = 0 \tag{3.11b}$$

$$\tilde{D}_n \left\langle \frac{\partial n^{(m)}(x)}{\partial x}, \frac{\partial W_3^{(m)}(x)}{\partial x} \right\rangle - \tilde{D}_n \left[ \frac{\partial n^{(m)}(x)}{\partial x} W_3^{(m)}(x) \right]_{x=0}^{x=h_c} + \left\langle Q_3^{(m)}(x), W_3^{(m)}(x) \right\rangle = 0 \tag{3.11c}$$

$$-\tilde{D}_p \left\langle \frac{\partial p^{(m)}(x)}{\partial x}, \frac{\partial W_4^{(m)}(x)}{\partial x} \right\rangle + \tilde{D}_p \left[ \frac{\partial p^{(m)}(x)}{\partial x} W_4^{(m)}(x) \right]_{x=0}^{x=h_c} + \left\langle Q_4^{(m)}(x), W_4^{(m)}(x) \right\rangle = 0 \tag{3.11d}$$

$\forall W_i^{(m)} \in V$ ($i$ = *1*, *2*, *3*, or *4*), where functions $W_i^{(m)}$ ($i$ = *1*, *2*, *3*, or *4*) are the testing functions, and

$$Q_1^{(m)}(x) = m^2\left(k_c^2 + \gamma^2\right)E_z^{(m)}(x) - jm\omega\mu\left[J_{nz}^{(m)(r)}(x) + J_{pz}^{(m)(r)}(x)\right] + \frac{qm\gamma}{\varepsilon}\left[p^{(m)}(x) - n^{(m)}(x)\right] \tag{3.12a}$$

$$Q_2^{(m)}(x) = m\gamma\frac{\partial E_z^{(m)}(x)}{\partial x} - jm\omega\mu\left[J_{nx}^{(m)}(x) + J_{px}^{(m)}(x)\right] \tag{3.12b}$$

$$Q_3^{(m)}(x) = -\tilde{D}_n m^2\gamma^2 n^{(m)}(x) + G_n^{(m)}(x) + jm\omega n^{(m)}(x) + u^{(m)}(x) + \sum_{s=0}^{m} F_n^{(m,s)}(x) \tag{3.12c}$$

$$Q_4^{(m)}(x) = \tilde{D}_p m^2\gamma^2 p^{(m)}(x) + G_p^{(m)}(x) - jm\omega\, p^{(m)}(x) - u^{(m)}(x) + \sum_{s=0}^{m} F_p^{(m,s)}(x) \tag{3.12d}$$

Equations (3.12a), (3.12b), (3.12c), and (3.12d) are, respectively, equivalent to the original differential equations (3.8a), (3.8b), (3.8c), and (3.8d) in a weak sense.

Note that all the terms involved with the unknown variables $E_z^{(m)}$, $E_x^{(m)}$, $n^{(m)}$, and $p^{(m)}$ are linear in $Q_i^{(m)}(x)$ ($i$ = *1*, *2*, *3*, or *4*). To express $Q_i^{(m)}(x)$ ($i$ = *1*, *2*, *3*, or *4*) in explicit linear combinations of the unknown variables $E_z^{(m)}$, $E_x^{(m)}$, $n^{(m)}$, and $p^{(m)}$, one can introduce

$$\begin{aligned} T_{ij}^{(m)}(x) &= \frac{\partial Q_i^{(m)}}{\partial U_j^{(m)}} && \text{for } i, j = 1,2,3,\text{or},4 \\ R_i^{(m)}(x) &= Q_i^{(m)}(x) - \sum_{j=1}^{4} T_{ij}^{(m)}(x)U_j^{(m)}(x) && \text{for } i = 1,2,3,\text{or},4 \end{aligned} \tag{3.13}$$

where $U_1^{(m)}$, $U_2^{(m)}$, $U_3^{(m)}$, and $U_4^{(m)}$ denote the unknown variables $E_z^{(m)}$, $E_x^{(m)}$, $n^{(m)}$, and $p^{(m)}$ respectively.

Since $Q_i^{(m)}(x)$ (*i = 1, 2, 3,* or *4*) linearly depend on the unknown variables $E_z^{(m)}$, $E_x^{(m)}$, $n^{(m)}$, and $p^{(m)}$, the newly introduced functions $T_{ij}^{(m)}(x)$ (*i, j = 1, 2, 3,* or *4*) and $R_i^{(m)}(x)$ (*i = 1, 2, 3,* or *4*) are independent of the unknown variables $E_z^{(m)}$, $E_x^{(m)}$, $n^{(m)}$, and $p^{(m)}$.

In terms of $T_{ij}^{(m)}(x)$ (*i, j = 1, 2, 3,* or *4*) and $R_i^{(m)}(x)$ (*i = 1, 2, 3,* or *4*), one can write

$$Q_i^{(m)}(x)=\sum_{j=1}^{4}T_{ij}^{(m)}(x)U_j^{(m)}(x)+R_i^{(m)}(x) \qquad i=1,2,3,\text{or},4 \tag{3.14}$$

and thus the weak forms (3.12a), (3.12b), (3.12c), and (3.12d) become

$$\begin{aligned}&-\left\langle \frac{\partial U_1^{(m)}(x)}{\partial x},\frac{\partial W_1^{(m)}(x)}{\partial x}\right\rangle+\left[\frac{\partial U_1^{(m)}(x)}{\partial x}W_1^{(m)}(x)\right]_{x=0}^{x=h_c}\\&+\sum_{j=1}^{4}\left\langle T_{1j}^{(m)}(x)U_j^{(m)}(x),W_1^{(m)}(x)\right\rangle+\left\langle R_1^{(m)}(x),W_1^{(m)}(x)\right\rangle=0\end{aligned} \tag{3.15a}$$

$$\begin{aligned}&m^2\left(k^2+\gamma^2\right)\left\langle U_2^{(m)}(x),W_2^{(m)}(x)\right\rangle\\&+\sum_{j=1}^{4}\left\langle T_{2j}^{(m)}(x)U_j^{(m)}(x),W_2^{(m)}(x)\right\rangle+\left\langle R_2^{(m)}(x),W_2^{(m)}(x)\right\rangle=0\end{aligned} \tag{3.15b}$$

$$\begin{aligned}&\tilde{D}_n\left\langle \frac{\partial U_3^{(m)}(x)}{\partial x},\frac{\partial W_3^{(m)}(x)}{\partial x}\right\rangle-\tilde{D}_n\left[\frac{\partial U_3^{(m)}(x)}{\partial x}W_3^{(m)}(x)\right]_{x=0}^{x=h_c}\\&+\sum_{j=1}^{4}\left\langle T_{3j}^{(m)}(x)U_j^{(m)}(x),W_3^{(m)}(x)\right\rangle+\left\langle R_3^{(m)}(x),W_3^{(m)}(x)\right\rangle=0\end{aligned} \tag{3.15c}$$

$$
\begin{gathered}
-\tilde{D}_p \left\langle \frac{\partial U_4^{(m)}(x)}{\partial x}, \frac{\partial W_4^{(m)}(x)}{\partial x} \right\rangle + \tilde{D}_p \left[ \frac{\partial U_4^{(m)}(x)}{\partial x} W_4^{(m)}(x) \right]_{x=0}^{x=h_c} \\
+ \sum_{j=1}^{4} \left\langle T_{4j}^{(m)}(x) U_j^{(m)}(x), W_4^{(m)}(x) \right\rangle + \left\langle R_4^{(m)}(x), W_4^{(m)}(x) \right\rangle = 0
\end{gathered}
\tag{3.15d}
$$

In general, a numerical method is completely specified by two sets of functions, i.e., the basis functions and the testing functions. The basis functions are used to expand the unknown functions. A very popular numerical procedure is Galerkin’s method, in which the set of testing functions is selected to be identical to the set of basis functions.

### 3.4.3: FINITE ELEMENT DISCRETIZATION

In a finite element analysis, the continuous solution domain under study is discretized into a series of elements. These elements are connected only at nodal points or on the element boundaries within the solution domain. In this way, the solution domain is discretized and represented as a patchwork of elements.

Once the element mesh for the solution domain has been determined, the unknown variables over each element are approximated by some continuous functions in terms of the nodal values of the respective unknown functions. These continuous functions defined over each element are called as interpolation functions or shape functions. The collection of interpolation functions over the entire solution domain provides a complete set of basis functions, which expand the unknown variables in a piecewise manner.

If the derivatives of the unknown functions in the weak formulation are up to the *k*-th order, the interpolation functions are required to meet the following requirements [59-63]:

- At interfaces or end-nodes between elements, the interpolation functions must have $C^{k-1}$ continuity, whereas within each element the interpolation functions must have $C^k$ continuity;

- The interpolation function referred to any arbitrarily given node assumes zero values in all elements that do not include the given node, whereas within elements containing the given node the interpolation function takes a unitary value at the given node and zero values at all other nodes.

The first requirement guarantees that the integrals in the weak formulation are bounded and well defined, whereas the second requirement implies that the unknown coefficients in the expansion of an unknown variable are, in fact, the values of the unknown variable at nodal points.

Since all the equations in the weak forms (3.15a), (3.15b), (3.15c), and (3.15d) have derivatives at most up to the first order, the standard polynomial interpolation (shape) functions with $C^0$ continuity are sufficient for the problem under study. As shown in finite element literature (e.g., [59-63]), the standard polynomial interpolation functions with $C^0$ continuity have $C^0$ continuity at element boundaries and at least $C^1$ continuity within elements.

Assume that there are a total of $M$ nodes in the discretized solution domain and denote them as $\{x_i\}_{i=1,2,\cdots,M}$. Let the interpolation function referred to node $x_i$ be $\psi_i(x)$. By the second requirement for interpolation functions, one must have

$$\psi_i(x_j) = \begin{cases} 1 & i = j \\ 0 & i \neq j \end{cases} \tag{3.16}$$

Any unknown function $U(x)$ can be expanded in a series of interpolation functions as follows:

$$U(x) = \sum_{i=1}^{M} U_i \, \psi_i(x) = \sum_{i=1}^{M} U(x_i)\psi_i(x) \tag{3.17}$$

where relation (3.16) has been exploited to obtain the second expansion in (3.17).

By applying expansion (3.17) to unknown functions $E_z^{(m)}$, $E_x^{(m)}$, $n^{(m)}$, and $p^{(m)}$ and using Galerkin's method, the weak forms (3.15a), (3.15b), (3.15c), and (3.15d) lead to a linear algebraic system:

$$\mathbf{K}^{(m)}\boldsymbol{\eta}^{(m)} = \mathbf{b}^{(m)} \tag{3.18}$$

where

$$\mathbf{K}^{(m)} = \begin{bmatrix} \mathbf{K}_{11}^{(m)} & \mathbf{K}_{12}^{(m)} & \mathbf{K}_{13}^{(m)} & \mathbf{K}_{14}^{(m)} \\ \mathbf{K}_{21}^{(m)} & \mathbf{K}_{22}^{(m)} & \mathbf{K}_{23}^{(m)} & \mathbf{K}_{24}^{(m)} \\ \mathbf{K}_{31}^{(m)} & \mathbf{K}_{32}^{(m)} & \mathbf{K}_{33}^{(m)} & \mathbf{K}_{34}^{(m)} \\ \mathbf{K}_{41}^{(m)} & \mathbf{K}_{42}^{(m)} & \mathbf{K}_{43}^{(m)} & \mathbf{K}_{44}^{(m)} \end{bmatrix} \tag{3.19a}$$

$$\boldsymbol{\eta}^{(m)} = \begin{bmatrix} \boldsymbol{\eta}_1^{(m)} \\ \boldsymbol{\eta}_2^{(m)} \\ \boldsymbol{\eta}_3^{(m)} \\ \boldsymbol{\eta}_4^{(m)} \end{bmatrix} \qquad \mathbf{b}^{(m)} = \begin{bmatrix} \mathbf{b}_1^{(m)} \\ \mathbf{b}_2^{(m)} \\ \mathbf{b}_3^{(m)} \\ \mathbf{b}_4^{(m)} \end{bmatrix} \tag{3.19b}$$

with $M \times M$ complex matrices $\mathbf{K}_{kl}^{(m)}$ ($k$, $l$ = $1, 2, 3$, or $4$) and complex vectors $\boldsymbol{\eta}_k^{(m)}$ and $\mathbf{b}_k^{(m)}$ ($k$ = $1, 2, 3$, or $4$) of size $M$, whose entries are given by

$$\begin{cases} \left(\boldsymbol{\eta}_1^{(m)}\right)_i = E_z^{(m)}(x_i) & \left(\boldsymbol{\eta}_2^{(m)}\right)_i = E_x^{(m)}(x_i) \\ \left(\boldsymbol{\eta}_3^{(m)}\right)_i = n^{(m)}(x_i) & \left(\boldsymbol{\eta}_4^{(m)}\right)_i = p^{(m)}(x_i) \end{cases} \tag{3.20}$$

$$\begin{aligned} \left(\mathbf{K}_{11}^{(m)}\right)_{ij} &= -\left\langle \frac{\partial \psi_j(x)}{\partial x}, \frac{\partial \psi_i(x)}{\partial x} \right\rangle + \left[ \frac{\partial \psi_j(x)}{\partial x} \psi_i(x) \right]_{x=0}^{x=h_c} \\ &\quad + \left\langle T_{11}^{(m)}(x)\psi_j(x), \psi_i(x) \right\rangle \end{aligned} \tag{3.21a}$$

$$\left(\mathbf{K}_{22}^{(m)}\right)_{ij} = m^2\left(k^2+\gamma^2\right)\left\langle \psi_j(x), \psi_i(x)\right\rangle + \left\langle T_{22}^{(m)}(x)\psi_j(x), \psi_i(x)\right\rangle \tag{3.21b}$$

$$\left(\mathbf{K}_{33}^{(m)}\right)_{ij} = \tilde{D}_n\left\langle \frac{\partial\psi_j(x)}{\partial x}, \frac{\partial\psi_i(x)}{\partial x}\right\rangle - \tilde{D}_n\left[\frac{\partial\psi_j(x)}{\partial x}\psi_i(x)\right]_{x=0}^{x=h_c} + \left\langle T_{33}^{(m)}(x)\psi_j(x), \psi_i(x)\right\rangle \tag{3.21c}$$

$$\left(\mathbf{K}_{44}^{(m)}\right)_{ij} = -\tilde{D}_p\left\langle \frac{\partial\psi_j(x)}{\partial x}, \frac{\partial\psi_i(x)}{\partial x}\right\rangle + \tilde{D}_p\left[\frac{\partial\psi_j(x)}{\partial x}\psi_i(x)\right]_{x=0}^{x=h_c} + \left\langle T_{44}^{(m)}(x)\psi_j(x), \psi_i(x)\right\rangle \tag{3.21d}$$

$$\left(\mathbf{K}_{kl}^{(m)}\right)_{ij} = \left\langle T_{kl}^{(m)}(x)\psi_j(x), \psi_i(x)\right\rangle \qquad \text{if } k \neq l \tag{3.21e}$$

$$\left(\mathbf{b}_{k}^{(m)}\right)_{i} = -\left\langle R_{k}^{(m)}(x), \psi_i(x)\right\rangle \tag{3.22}$$

Note that the boundary terms in (3.21a), (3.21b), (3.21c), and (3.21d) vanish for all interior nodes due to the localization property implied by (3.16). A boundary condition of the first kind can be imposed by replacing the row equation corresponding to the specified boundary node with the boundary condition itself in (3.18). On the other hand, boundary conditions of the second or third kind can be utilized to zero the boundary terms or specify the boundary derivatives of the unknown variables in terms of their boundary values in (3.21a), (3.21b), (3.21c), and (3.21d).

### 3.4.4: SOME SPECIAL CONSIDERATIONS

As pointed out in Subsection 3.3.1, an accumulation-depletion layer of charged carriers appears in the semiconductor near the interface at $x = 0$. In order for modeling the fast decaying behavior of carrier concentrations in the accumulation-depletion layer, an adaptive meshing scheme must be employed to allocate finer elements at locations closer to the interface $x = 0$ in the finite element discretization.

Theoretically, the $x$ component of electrical field should automatically fulfill the boundary condition:

$$E_x^{(m)}\left(0^+\right) = \frac{\varepsilon_d}{\varepsilon} E_x^{(m)}\left(0^-\right) = \frac{\varepsilon_d}{\varepsilon} A^{(m)} \cos\left(m k_d h_d\right) \qquad (3.23)$$

However, the weak solution may not satisfy (3.23) due to the weak sense of the numerical solution and the error introduced by numerical evaluation of the derivative term in (3.1d). The consequences can be severe because the solution in the accumulation-depletion layer is quite sensitive. In order to remove the degradation of accuracy near the interface at $x = 0$ and enhance the overall solution convergence, a boundary term imposing (3.23) at $x = 0$ needs to be added into the weak form (3.11b). By so doing, the numerical solution is actually required to satisfy (3.23) at $x = 0$ while meet (3.1d) everywhere else.

## 3.5: SOLUTION OF NONLINEAR SYSTEM AND NEWTON’S METHOD

For the fundamental mode, the propagation factor $\gamma$ needs to be determined along with electromagnetic fields and carrier concentrations. Thus, one more equation is required besides the matrix equation (3.18). Equation (3.5) is the additional desirable equation. By simultaneously solving (3.5) and (3.18), one can obtain $\gamma$, $E_z^{(1)}$, $E_x^{(1)}$, $n^{(1)}$, and $p^{(1)}$. Note that both equations (3.5) and (3.18) are nonlinear in the propagation factor $\gamma$. Hence, the set of equations for the fundamental mode is essentially a nonlinear system of equations. Newton’s method [64-66] can be used to solve such a nonlinear system of equations.

In summary, one needs to solve the set of nonlinear equations as follows:

$$\mathbf{\Gamma}(\boldsymbol{\eta}) \equiv \begin{bmatrix} \mathbf{K}^{(1)}\boldsymbol{\eta}^{(1)} - \mathbf{b}^{(1)} \\ j\omega\varepsilon_d E_z^{(1)}(0^+) + k_d \tan(k_d h_d) H_y^{(1)}(0^+) \end{bmatrix} = 0 \tag{3.24}$$

where $\mathbf{\Gamma}(\cdot)$ denotes the *(4M+1)*-dimensional vector of functions, and

$$\boldsymbol{\eta} = \begin{bmatrix} \boldsymbol{\eta}^{(1)} \\ \gamma \end{bmatrix} \tag{3.25}$$

Note that $E_z^{(1)}(0^+)$ is a component of vector $\boldsymbol{\eta}^{(1)}$, whereas $H_y^{(1)}(0^+)$ is a function of the propagation factor $\gamma$ and the components of vector $\boldsymbol{\eta}^{(1)}$ as implied by (3.1e).

Using Taylor's series expansion, one can obtain

$$\mathbf{\Gamma}(\boldsymbol{\eta} + \Delta\boldsymbol{\eta}) = \mathbf{\Gamma}(\boldsymbol{\eta}) + \mathbf{D} \cdot \Delta\boldsymbol{\eta} + O\left([\Delta\boldsymbol{\eta}]^2\right) \tag{3.26}$$

where $\Delta\boldsymbol{\eta}$ is a small deviation from $\boldsymbol{\eta}$ and the $(4M+1)\times(4M+1)$ matrix $\mathbf{D}$ is the Jacobian matrix, whose entries are given by

$$D_{ij} = \frac{\partial \Gamma_i}{\partial \eta_j} \tag{3.27}$$

It is obvious to see that

$$\mathbf{D}(1:4M, 1:4M) = \mathbf{K}^{(1)} \tag{3.28}$$

Neglecting terms of order $[\Delta\boldsymbol{\eta}]^2$ and higher and setting $\mathbf{\Gamma}(\boldsymbol{\eta} + \Delta\boldsymbol{\eta}) = 0$, one obtains a set of linear equations for the correction vector $\Delta\boldsymbol{\eta}$ that moves $\mathbf{\Gamma}(\cdot)$ closer to zero, namely

$$\mathbf{D} \cdot \Delta\boldsymbol{\eta} = -\mathbf{\Gamma}(\boldsymbol{\eta}) \tag{3.29}$$

A new solution is then obtained by including the correction vector:

$$\boldsymbol{\eta}_{new} = \boldsymbol{\eta} + \Delta\boldsymbol{\eta} \tag{3.30}$$

The above iteration can be repeated until the solution converges. Then, a solution to the set of nonlinear equations is obtained. The above iterative procedure is a brief account of Newton's method.

Newton's method is generally sensitive to the initial guess. In order to get a convergent solution, the initial guess is sometimes required to be sufficient close to the real solution. Some variants of Newton's method have been developed to alleviate this problem [66]. Nevertheless, one can always use the solutions of some simplified yet closely related problems as the initial guess to speed up the convergence of Newton's iterations.

Unlike the iterative algorithm in [42], which solved each of the equations for $n^{(1)}$, $p^{(1)}$, $E_z^{(1)}$, and $\gamma$ sequentially and separately at each iteration, all the equations are simultaneously solved using multi-dimensional Newton's method in this approach, which reduces the number of iterations considerably.

For high order harmonics, the propagation factor $\gamma$ has been determined ahead when the equations for the fundamental mode were first solved. Hence, the matrix $\mathbf{K}^{(m)}$ ($m > 1$) is a known quantity. One can directly solve the matrix equation (3.18) for high order harmonic electromagnetic fields and carrier concentrations using linear matrix solvers.

## 3.6: SOLUTION OF LINEAR SYSTEM AND SPARSE MATRIX TECHNIQUES

For the fundamental mode, one needs to solve the matrix equation (3.29) for the corrections of the propagation factor, electromagnetic fields, and carrier concentrations during each of Newton's iterations. On the other hand, the matrix equation (3.18) must be solved to determine electromagnetic fields and carrier concentrations for each of high order harmonics. The efficient solution of a linear algebraic system plays an essential role for achieving fast device level simulation.

In practice, it is very common that orders of magnitudes of the unknown variables such as electromagnetic fields and carrier concentrations are far apart, which may range from $10^{-15}$ to $10^{18}$. The large disparity of the magnitudes among unknown variables could result in computer word length overflow and underflow during matrix operations. To circumvent such a potential numerical breakdown, the scale equilibration or matrix balancing among unknown variables is undertaken.

As expected for the finite element analysis of partial differential equations, both $\mathbf{K}^{(m)}$ and $\mathbf{D}$ are sparse matrices. To gain fast computational speed and save memory, sparse matrix techniques [67-70] are utilized for solving linear algebraic equations.

To minimize the memory requirement, indexed storage via one-dimensional arrays is used. The precise pattern of the matrix sparsity is recorded, and only nonzero entries are stored. Both direct and iterative methods can be employed. In a direct method, the number of fill-ins is first to be minimized by re-ordering schemes and then the factorization is performed. For large sparse linear systems, iterative methods such as preconditioned conjugate gradient (CG) method or generalized minimum residual (GMRES) method may outperform direct methods and thus be preferred in many practical situations.

## 3.7: SUMMARY

In this chapter, the device level frequency domain (DLFD) simulation has been developed for investigating the wave propagation characteristics along MIS interconnects. This device level simulation is based on the general frequency domain formulae. For simplicity, an MIS interconnect was modeled as a parallel-plate waveguide structure for the device level simulation. The boundary conditions were carefully studied and properly devised.

The finite element method was utilized for discretization of the basic equations. The weak formulation was developed for each harmonic. By virtue of Galerkin’s method and finite element discretization, a set of algebraic equations was obtained for each harmonic. For the fundamental mode, a set of nonlinear equations was derived. Multi-dimensional Newton’s method has been found to be suitable and efficient for tackling the set of nonlinear equations. For a high order harmonic, only a set of linear algebraic equations needs to be solved. Sparse matrix techniques have been used for improving computational speed and saving memory space.

The nonlinearity in the motion equations of charged carriers was preserved and included in the formulae. Thus, this approach is suitable for both small-signal and large-signal analyses. The boundary layer nature of the problem under study has been manifested theoretically and treated in a numerically consistent manner through adaptive finite element discretization.

This device level simulation can provide quantitative predictions to propagation and attenuation constants as well as detailed electromagnetic field and carrier concentration distributions of the fundamental mode and high order harmonics. This proposed device level simulation scheme allows for large-signal analysis to be performed and is capable of studying detailed field-carrier interaction mechanisms, semiconductor substrate loss and nonlinearity, as well as slow-wave, external bias, and screening effects of charged carriers. It has been shown that higher order harmonics due to the semiconductor nonlinearity are confined within the semiconductor and do not penetrate into the insulator in MIS waveguide structures.

# CHAPTER 4: EXTRACTION OF EQUIVALENT CIRCUIT MODEL

To construct equivalent circuit models for the interconnects, a contour integral based approach has been widely employed (e.g., [6, 17, 43]). Integrals of electromagnetic fields over the appropriate contours are used as a convenient definition for voltage and current. These definitions of voltage and current are valid, however, only for TEM waves.

For TM waves, the contour integral definitions of voltage and current, which is a consequence of the TEM assumptions, are no longer applicable. The presence of a longitude electrical field implies that the transverse field components do not satisfy the equations of a static analysis, and thus the contour integral definitions of voltage and current are no longer valid. Instead, an energy-based method should be employed to build the equivalent circuit model.

In this chapter, the energy-based approach [44] is employed to construct an equivalent circuit model from the device level simulation results. The energy-based approach abandons the approach based on intuitively chosen contour integrals. Rather, it builds the equivalent circuit model based on the power equivalence between the circuit model and the actual MIS waveguide.

## 4.1: ENERGY BASED APPROACH

A general form of the transmission line model consists of a series impedance $Z$ per unit length and a shunt admittance $Y$ per unit length, as shown in Figure 4.1.

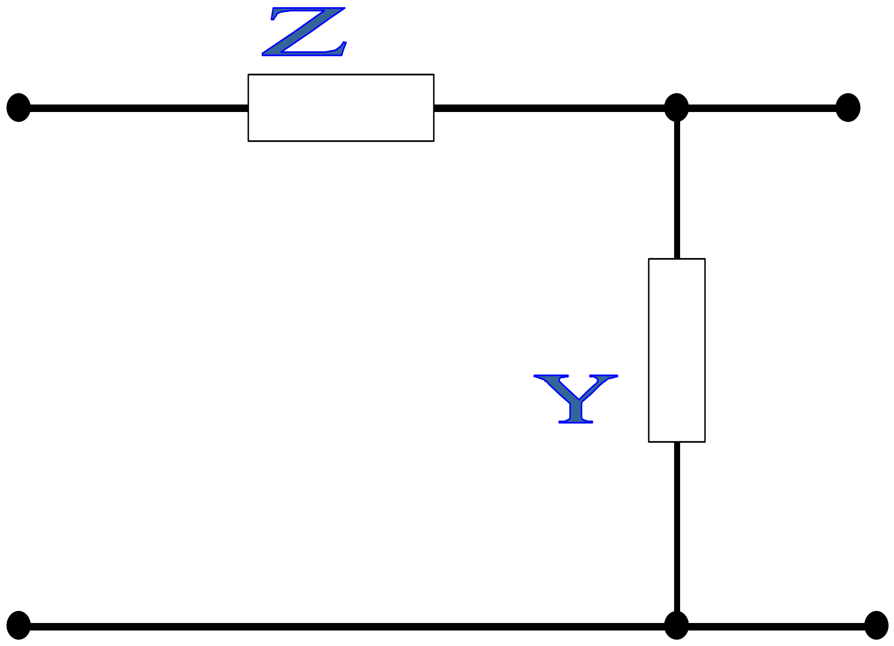

Figure 4.1: General form of the transmission line model

To build an equivalent transmission line model, the following requirements are prescribed [44]:

- The propagation constant $\gamma_{eq}$ for the equivalent transmission line should be identical to the propagation constant $\gamma$ of the electromagnetic wave propagating along the original MIS interconnect:

$$\gamma_{eq} = \gamma = \alpha + j\beta \tag{4.1}$$

where $\alpha$ is the attenuation constant and $\beta$ is the phase constant.

- The complex time-averaged power $P_{eq}(z)$ traveling down the equivalent circuit is required to be equal to the complex time-averaged power $P(z)$ traveling down the original MIS interconnect:

$$P_{eq}(z) = P(z) \tag{4.2}$$

The propagation constant $\gamma_{eq}$ and characteristic impedance $Z_0$ of the equivalent transmission line model can be expressed in terms of the series impedance $Z$ and shunt admittance $Y$ per unit length as follows [47]:

$$\gamma_{eq} = \sqrt{ZY} \tag{4.3a}$$

$$Z_0 = \sqrt{\frac{Z}{Y}} = \frac{Z}{\gamma_{eq}} = \frac{\gamma_{eq}}{Y} \tag{4.3b}$$

In the case of a single propagating mode, the voltage $V(z)$ and current $I(z)$ of the equivalent transmission line are simply related by the characteristic impedance through

$$Z_0 = \frac{V(z)}{I(z)} \tag{4.4}$$

Moreover, the complex time-averaged power $P_{eq}(z)$ can be expressed as

$$P_{eq}(z) = \frac{1}{2} V(z) I^*(z) = \frac{1}{2} |I(z)|^2 Z_0 \tag{4.5}$$

where the superscript "*" denotes a complex conjugate quantity. Equation (4.5) can be rewritten as

$$Z_0 = \frac{2P_{eq}(z)}{|I(z)|^2} \tag{4.6}$$

Combining (4.1), (4.2), (4.3b), and (4.6) leads to

$$Z = \gamma_{eq} Z_0 = \gamma \frac{2P(z)}{|I(z)|^2} \tag{4.7a}$$

$$\frac{1}{Y} = \frac{1}{\gamma_{eq}} Z_0 = \frac{1}{\gamma} \frac{2P(z)}{|I(z)|^2} \tag{4.7b}$$

The complex time-averaged power traveling down the original MIS interconnect can be obtained by

$$P(z) = \frac{1}{2T} \int_0^T \left\{ \iint_{(x,y)\in S} \left[ \mathbf{E} \times \mathbf{H}^* \right] \cdot \hat{\mathbf{z}} \; dxdy \right\} dt \tag{4.8}$$

where $T = 2\pi/\omega$ and $S = S_0 + S_s$ is the cross section of the MIS interconnect, as shown in Figure 4.2.

The current flowing through the equivalent transmission line can be defined as the physical current flowing through the signal line of the MIS interconnect, that is,

$$I(z) = \iint_{(x,y)\in S_i} \mathbf{J} \cdot \hat{\mathbf{z}} \, dxdy \tag{4.9}$$

where $S_i$ denotes the cross-section of the signal line, as shown in Figure 4.2.

Write $P(z)$ into two terms:

$$P(z) = P_0(z) + P_s(z) \tag{4.10}$$

where

$$P_0(z) = \frac{1}{2T} \int_0^T \left\{ \iint_{(x,y)\in S_0} \left[ \mathbf{E} \times \mathbf{H}^* \right] \cdot \hat{\mathbf{z}} \; dxdy \right\} dt \tag{4.11a}$$

$$P_s(z) = \frac{1}{2T} \int_0^T \left\{ \iint_{(x,y)\in S_s} \left[ \mathbf{E} \times \mathbf{H}^* \right] \cdot \hat{\mathbf{z}} \; dxdy \right\} dt \tag{4.11b}$$

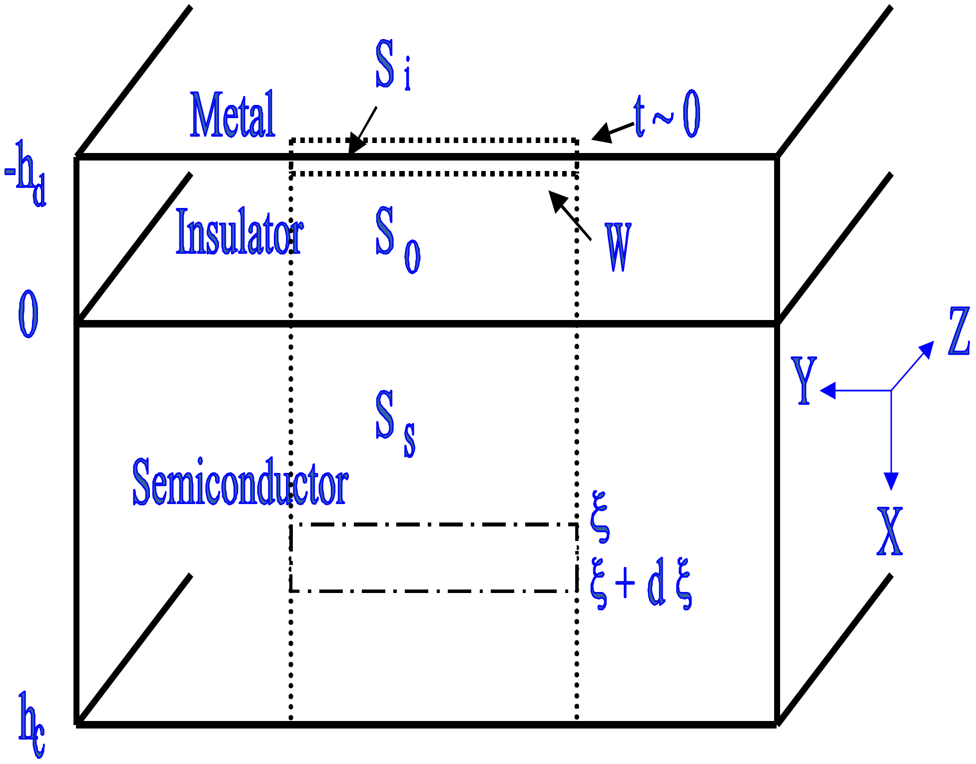

Figure 4.2: Pictorial illustration of $S_i$, $S_0$, and $S_s$ in calculation of equivalent circuit elements

Substituting (4.10) into (4.7a) and (4.7b), one can write

$$Z = (R_0 + j\omega L_0) + (R_s + j\omega L_s) \tag{4.12a}$$

$$\frac{1}{Y} = \frac{1}{G_0 + j\omega C_0} + \frac{1}{G_s + j\omega C_s} \tag{4.12b}$$

such that

$$R_0 + j\omega L_0 = \gamma \frac{2P_0(z)}{|I(z)|^2} \tag{4.13a}$$

$$\frac{1}{G_0 + j\omega C_0} = \frac{1}{\gamma}\,\frac{2P_0(z)}{|I(z)|^2} \tag{4.13b}$$

$$R_s + j\omega L_s = \gamma\,\frac{2P_s(z)}{|I(z)|^2} \tag{4.13c}$$

$$\frac{1}{G_s + j\omega C_s} = \frac{1}{\gamma}\,\frac{2P_s(z)}{|I(z)|^2} \tag{4.13d}$$

Equations (4.13a), (4.13b), (4.13c), and (4.13d) provide the basic formulae for calculating the circuit elements of equivalent circuit model.

## 4.2: CIRCUIT ELEMENTS DUE TO EM FIELDS IN INSULATOR LAYER

Denote

$$E_0(z,t) = E_0(z)\cdot e^{j\omega t} = E_x^{(1)}\Big|_{x=-h_d} = A^{(1)}\cdot e^{-\gamma z}\cdot e^{j\omega t} \tag{4.14}$$

Using (3.3a), (3.3b), (3.3c), and (3.7), the field components in the insulator layer are given by:

$$E_z(x,z,t) = E_z^{(1)}(x,z,t) = -\frac{k_d E_0(z,t)}{\gamma}\sin[k_d(x+h_d)] \tag{4.15a}$$

$$E_x(x,z,t) = E_x^{(1)}(x,z,t) = E_0(z,t)\cos[k_d(x+h_d)] \tag{4.15b}$$

$$H_y(x,z,t) = H_y^{(1)}(x,z,t) = \frac{j\omega\varepsilon_d E_0(z,t)}{\gamma}\cos[k_d(x+h_d)] \tag{4.15c}$$

$$E_y(x,z,t) = H_x(x,z,t) = H_z(x,z,t) = 0 \tag{4.15d}$$

Therefore, one obtains

$$I(z,t)=\iint_{(x,y)\in S_i}\mathbf{J}\cdot\hat{\mathbf{z}}\,dxdy=\int_0^w J_{sz}\Big|_{x=-h_d}dy=\int_0^w(\hat{\mathbf{x}}\times\mathbf{H})\Big|_{x=-h_d}dy \tag{4.16a}$$
$$=\int_0^w H_y\Big|_{x=-h_d}dy=wH_y\Big|_{x=-h_d}=\frac{j\omega\varepsilon_d w}{\gamma}E_0(z,t)$$

namely,

$$I(z)=\frac{j\omega\varepsilon_d w}{\gamma}E_0(z) \tag{4.16b}$$

Moreover, one has

$$P_0(z)=\frac{1}{2T}\int_0^T\left\{\iint_{(x,y)\in S_0}\left[\mathbf{E}\times\mathbf{H}^*\right]\cdot\hat{\mathbf{z}}\;dxdy\right\}dt=\frac{1}{2T}\int_0^T\left\{\iint_{(x,y)\in S_0}E_xH_y^*\;dxdy\right\}dt$$
$$=\frac{1}{2T}\int_0^T\left\{\iint_{(x,y)\in S_0}\left|E_0(z,t)\cos[k_d(x+h_d)]\right|^2\left(\frac{j\omega\varepsilon_d}{\gamma}\right)^*dxdy\right\}dt \tag{4.17}$$
$$=\frac{-j\omega\varepsilon_d w}{2\gamma^*}\left|E_0(z)\right|^2\int_{-h_d}^0\left|\cos[k_d(x+h_d)]\right|^2dx=\frac{-j\gamma K_d}{2\omega\varepsilon_d w}\left|I(z)\right|^2$$

where the positive real constant $K_d$ is given by

$$K_d=\int_{-h_d}^0\left|\cos[k_d(x+h_d)]\right|^2dx=\int_{-h_d}^0\left|\frac{e^{jk_d(x+h_d)}+e^{-jk_d(x+h_d)}}{2}\right|^2dx$$
$$=\frac{1}{2}\int_{-h_d}^0\{\cos[2\operatorname{Re}(k_d)(x+h_d)]+\cosh[2\operatorname{Im}(k_d)(x+h_d)]\}dx \tag{4.18}$$
$$=\frac{1}{2}\left\{\frac{\sin[2\operatorname{Re}(k_d)h_d]}{2\operatorname{Re}(k_d)}+\frac{\sinh[2\operatorname{Im}(k_d)h_d]}{2\operatorname{Im}(k_d)}\right\}$$

Note that $K_d\approx h_d$ as $|k_dh_d|<<1$. Hence, $K_d$ can be viewed as an equivalent thickness of the insulator layer.

Equation (4.17) leads to

$$\frac{2P_0(z)}{|I(z)|^2} = \frac{K_d}{j\omega\varepsilon_d w}\gamma \tag{4.19}$$

Substitution of (4.19) into (4.13a) and (4.13b) results in the expansions:

$$R_0 + j\omega L_0 = \frac{K_d}{j\omega\varepsilon_d w}\left(\alpha^2 - \beta^2 + j2\alpha\beta\right) \tag{4.20a}$$

$$\frac{1}{G_0 + j\omega C_0} = \frac{K_d}{j\omega\varepsilon_d w} \tag{4.20b}$$

That is,

$$R_0 = \frac{2\alpha\beta K_d}{\omega\varepsilon_d w}, \qquad L_0 = \frac{K_d}{\varepsilon_d w}\frac{\left(\beta^2 - \alpha^2\right)}{\omega^2} \tag{4.21a}$$

$$C_0 = \frac{\varepsilon_d w}{K_d}, \qquad G_0 = 0 \tag{4.21b}$$

Note that $R_0$ is nonzero even if the insulator medium is lossless. Equation (4.21a) shows that $R_0 \to 0$ as $\alpha \to 0$. Hence, the existence of nonzero $R_0$ is due to the influence of the semiconductor loss upon electromagnetic fields in the insulator layer.

## 4.3: CIRCUIT ELEMENTS DUE TO EM FIELDS IN SEMICONDUCTOR LAYER

The field components in the semiconductor layer take the following form:

$$E_x(x,z,t) = \sum_{m=1}^{\infty} E_x^{(m)}(x)\cdot e^{-m\gamma z}\cdot e^{jm\omega t} \tag{4.22a}$$

$$E_z(x,z,t) = \sum_{m=1}^{\infty} E_z^{(m)}(x)\cdot e^{-m\gamma z}\cdot e^{jm\omega t} \tag{4.22b}$$

$$H_y(x,z,t) = \sum_{m=1}^{\infty} H_y^{(m)}(x) \cdot e^{-m\gamma z} \cdot e^{jm\omega t} \tag{4.22c}$$

$$E_y(x,z,t) = H_x(x,z,t) = H_z(x,z,t) = 0 \tag{4.22d}$$

Equations (4.22a), (4.22b), (4.22c), and (4.22d) lead to

$$\begin{aligned} P_s(z) &= \frac{1}{2T}\int_0^T \left\{ \iint_{(x,y)\in S_s} \left[\mathbf{E}\times\mathbf{H}^*\right]\cdot\hat{\mathbf{z}}\ dxdy \right\} dt = \frac{1}{2T}\int_0^T \left\{ \iint_{(x,y)\in S_s} E_x H_y^*\ dxdy \right\} dt \\ &= \sum_{m=1}^{\infty} \frac{P_s^{(m)}}{\left[A^{(1)}\right]^{2m}} \left( \frac{|\gamma|}{\omega\varepsilon_d w} \right)^{2m} |I(z)|^{2m} \end{aligned} \tag{4.23}$$

where (4.16b) has been used, and

$$P_s^{(m)} = \frac{1}{2} \iint_{(x,y)\in S_s} E_x^{(m)}(x)\left[H_y^{(m)}(x)\right]^* dxdy = \frac{w}{2}\int_0^{h_c} E_x^{(m)}(x)\left[H_y^{(m)}(x)\right]^* dx \tag{4.24}$$

Equation (4.23) yields

$$\frac{2P_s(z)}{|I(z)|^2} = 2\sum_{m=1}^{\infty} \frac{P_s^{(m)}}{\left[A^{(1)}\right]^{2m}} \left( \frac{|\gamma|}{\omega\varepsilon_d w} \right)^{2m} |I(z)|^{2(m-1)} \tag{4.25}$$

Using (4.25), (4.13c) and (4.13d) give

$$R_s + j\omega L_s = 2\gamma \sum_{m=1}^{\infty} \frac{P_s^{(m)}}{\left[A^{(1)}\right]^{2m}} \left( \frac{|\gamma|}{\omega\varepsilon_d w} \right)^{2m} |I(z)|^{2(m-1)} \tag{4.26a}$$

$$\frac{1}{G_s + j\omega C_s} = \frac{2}{\gamma} \sum_{m=1}^{\infty} \frac{P_s^{(m)}}{\left[A^{(1)}\right]^{2m}} \left( \frac{|\gamma|}{\omega\varepsilon_d w} \right)^{2m} |I(z)|^{2(m-1)} \tag{4.26b}$$

That is,

$$Z_s = R_s + j\omega L_s = Z_s^{(1)} + \sum_{m=2}^{\infty} Z_s^{(m)} \left| I(z) \right|^{2(m-1)} \tag{4.27a}$$

$$\frac{1}{Y_s} = \frac{1}{G_s + j\omega C_s} = \frac{1}{Y_s^{(1)}} + \sum_{m=2}^{\infty} \frac{1}{Y_s^{(m)}} \left| I(z) \right|^{2(m-1)} \tag{4.27b}$$

where

$$Z_s^{(m)} = R_s^{(m)} + j\omega L_s^{(m)} = 2\gamma \left( \frac{|\gamma|}{\omega \varepsilon_d w} \right)^{2m} \frac{P_s^{(m)}}{\left[A^{(1)}\right]^{2m}} \tag{4.28a}$$

$$Y_s^{(m)} = G_s^{(m)} + j\omega C_s^{(m)} = 1 \Bigg/ \left[ \frac{2}{\gamma} \left( \frac{|\gamma|}{\omega \varepsilon_d w} \right)^{2m} \frac{P_s^{(m)}}{\left[A^{(1)}\right]^{2m}} \right] \tag{4.28b}$$

The device level simulation in the preceding chapter shows that the *m*-th harmonic field components are proportional to $\left[A^{(1)}\right]^m$ in magnitude. The quantity $P_s^{(m)}$ is thus proportional to $\left[A^{(1)}\right]^{2m}$ based on using (4.24). Therefore, the coefficients $R_s^{(m)}$, $L_s^{(m)}$, $G_s^{(m)}$ and $C_s^{(m)}$ given by (4.28a) and (4.28b) are independent of the excitation strength. These coefficients are functions of the geometry and material parameters only.

## 4.4: EQUIVALENT CIRCUIT MODEL

In summary, the equivalent circuit model for MIS interconnects consists of an equivalent transmission line, as shown by Figure 4.3. The line parameters of the equivalent circuit model are given by (4.21a), (4.21b), (4.27a), (4.27b), (4.28a), and (4.28b).

In Figure 4.3, circuit elements $R_0$, $L_0$, and $C_0$ are, respectively, the resistance, inductance, and capacitance per unit length due to electromagnetic field in the insulator layer, whereas circuit elements $R_s$, $L_s$, $C_s$, and $G_s$ denote, respectively, the resistance, inductance, capacitance, and conductance per unit length due to electromagnetic field in the semiconductor substrate. Circuit element $R_c$ denotes the resistance per unit length over the signal line, which is not studied here since the signal line has been treated as an ideal conductor.

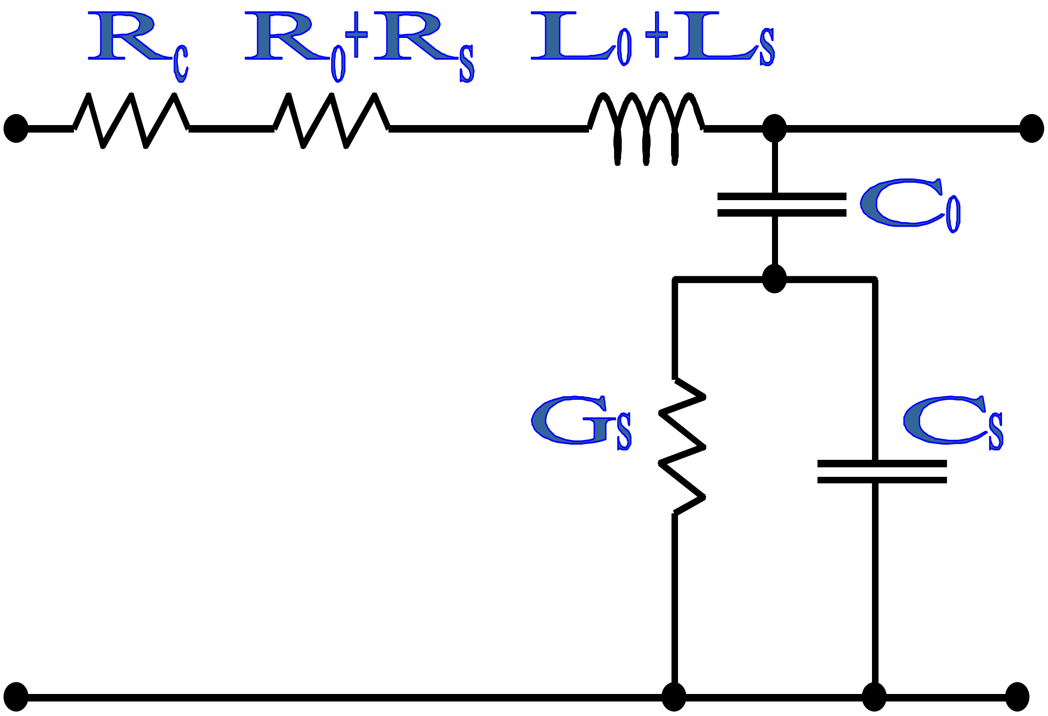

Figure 4.3: Equivalent circuit model for MIS interconnects

Equations (4.27a) and (4.27b) state that all the impedance elements due to the semiconductor effects are connected in series, as do the shunt admittance elements, as shown by Figure 4.4 and Figure 4.5. The first terms in (4.27a) and (4.27b) are, respectively, the contributions to the series impedance and shunt admittance from the fundamental mode. The remaining terms are due to high order harmonics and exhibit nonlinear characteristics as manifested by their dependence on the magnitude of signal current in (4.27a) and (4.27b).

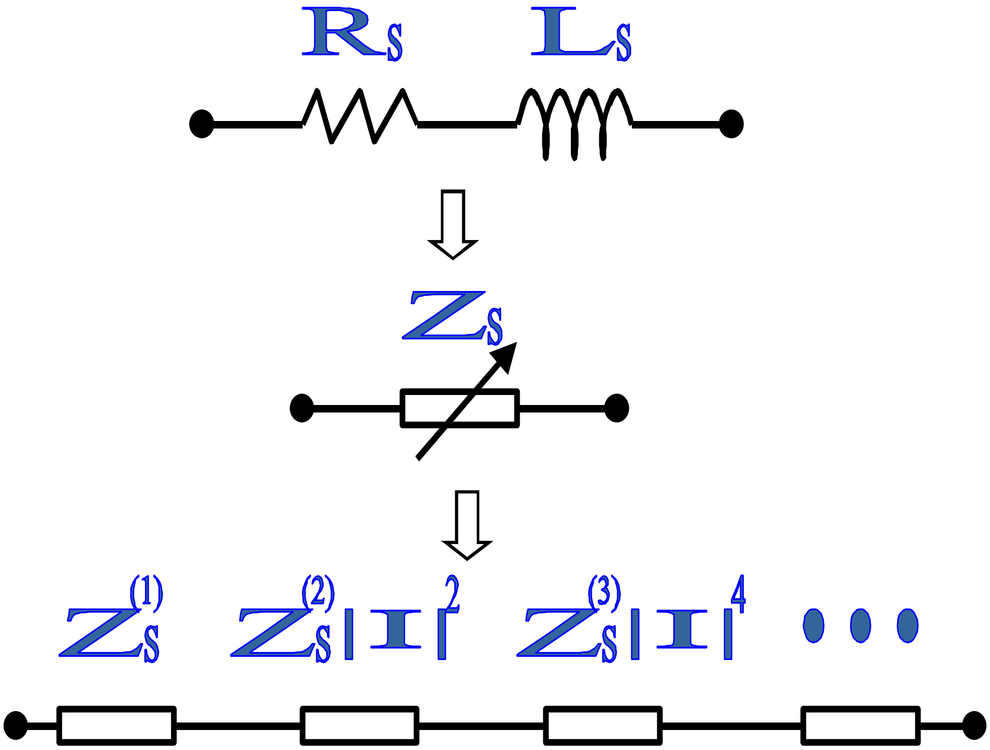

Figure 4.4: Impedance $Z_s$ consists of a linear inductance element and many nonlinear impedance elements connected in series

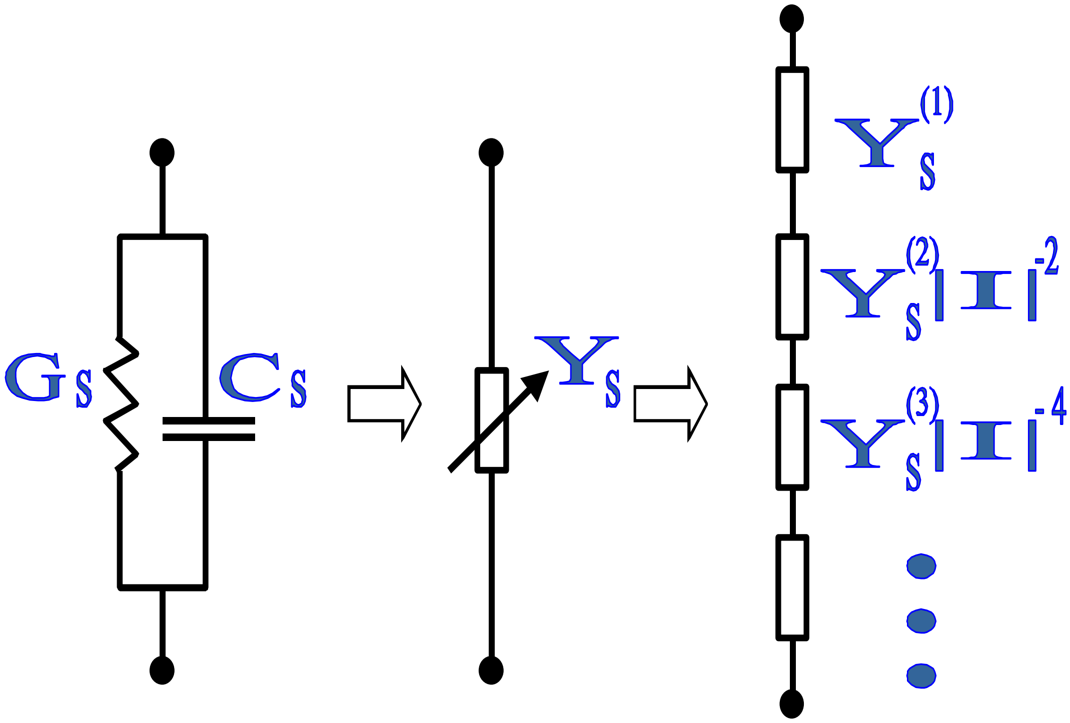

Figure 4.5: Admittance $Y_s$ consists of a linear admittance element and many nonlinear admittance elements connected in series

For use in the small signal analysis mode, the nonlinear terms in (4.27a) and (4.27b) are small and can be generally neglected. The equivalent circuit model then reduces to a linear transmission line, which have been studied extensively using approaches such as fast Fourier transform (FFT) [71-74], numerical inversion of Laplace transform (NILT) [75-77], asymptotic waveform evaluation (AWE) [78-81], and recursive convolution [82, 83]. Most previous modeling of MIS interconnects has been carried out using only the electromagnetic analysis, with semiconductor effects simply accounted for by virtue of the conductivity, permittivity, and permeability of semiconductor material. That is, the basic formula relies on Maxwell’s equations and thus only the linear equivalent circuit elements can be extracted.

Since the equivalent circuit model is generally a nonlinear transmission line, this behavior necessities large signal analysis. Circuit simulation of nonlinear transmission lines has been addressed by numbers of previous research work (e.g., see [84-86]). The nonlinear circuit model obtained from this device level approach can be directly used in nonlinear circuit simulations.

## 4.5: SUMMARY

Based on the device level frequency domain (DLFD) simulation, a rigorous modeling scheme for metal-insulator-semiconductor (MIS) interconnects has been introduced. The energy-based approach was used for construction of the equivalent circuit model from the device level simulation results. The equivalent circuit model consists of a transmission line, which mimics the energy transport characteristics of the actual MIS interconnect.

In the device level simulation, the motion equations of charged carriers and Maxwell’s equations were solved simultaneously. The device level simulation provides knowledge on field-carrier interactions, semiconductor substrate loss and nonlinearity, as well as slow-wave effect, external bias effect, and screening effect of charged carriers. The equivalent circuit model retains information about the semiconductor substrate effects obtained from the device level simulation, and thus provides a generalized nonlinear and electronic tunable circuit model suitable for both small-signal and large-signal analyses.

# CHAPTER 5: COMPUTER SOFTWARE REALIZATION

In this chapter, the computer software realization is described for device level frequency domain (DLFD) simulation as well as extraction of equivalent circuit models.

## 5.1: SOFTWARE REALIZATION OF DEVICE LEVEL SIMULATION

The device level frequency domain (DLFD) simulation of wave propagation along MIS interconnects is conducted within the PROPHET framework. The PROPHET simulator is a tool to solve systems of partial differential equations [87]. This simulator has been utilized industrially to perform semiconductor process simulation for several years. Electromagnetic analysis is, however, not available in the PROPHET framework. In order to perform the device level simulation of wave propagation along MIS interconnects, electromagnetic analysis capability must be added into the PROPHET simulator.

### 5.1.1: FLOWCHART OF DEVICE LEVEL SIMULATION

Figure 5.1 illustrates the flowchart of the device level simulation for wave propagation along MIS interconnects. The software tool takes, as inputs, the material properties, geometrical parameters, operating frequency, excitation strength, external bias, number of harmonics to be solved, mesh specification, and equation descriptions. The input information is usually presented through either a script file or a database library.

The input parser analyzes the inputs and stores the information into the internal database for future use. Then, the tool performs mesh generation according to the mesh specification given at the inputs. The tool is then ready to solve the equation systems on the meshed domain.

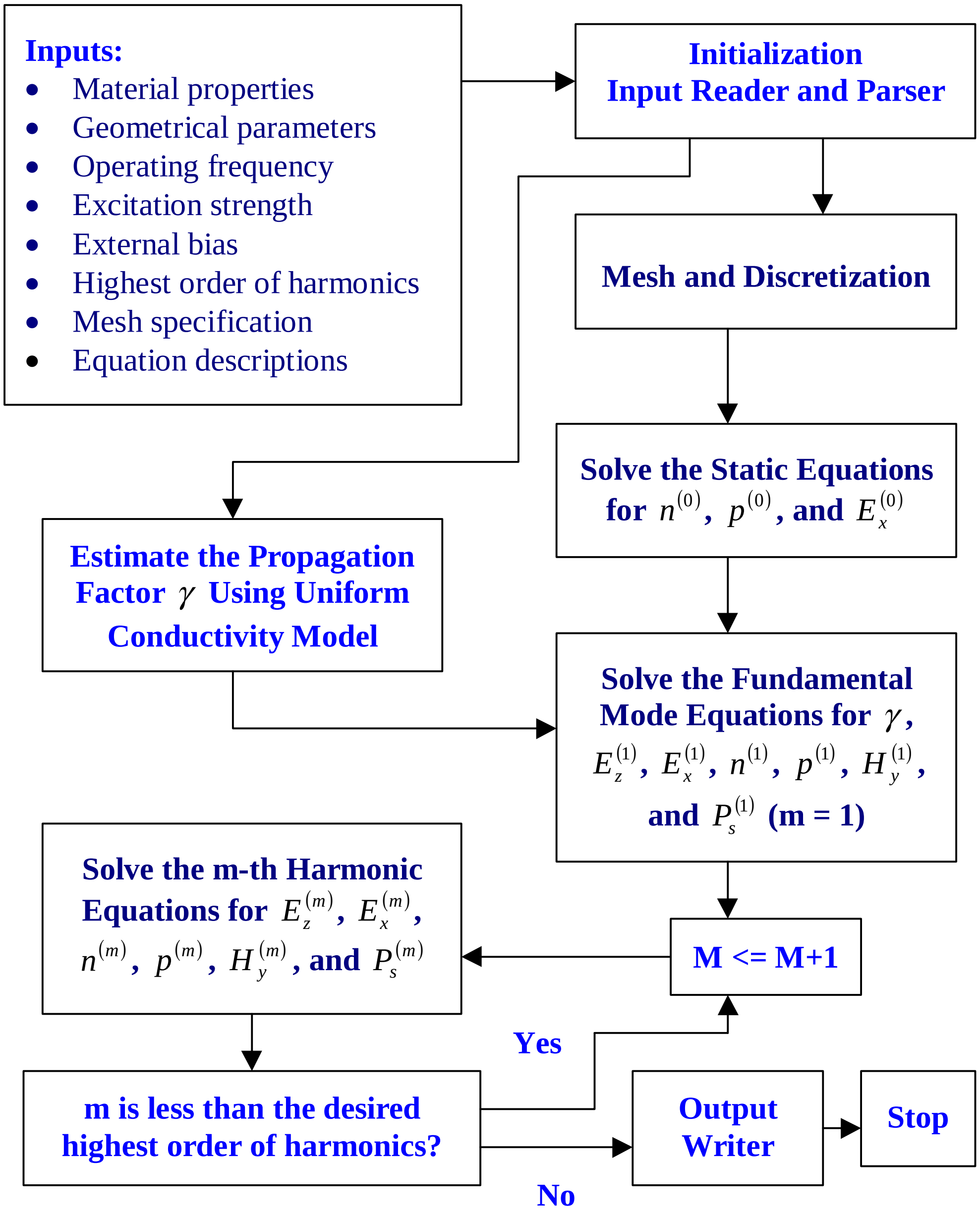

Figure 5.1: Flowchart of device level simulation

The first set of equations to be solved is the set of static equations. The static quantities $n^{(0)}$, $p^{(0)}$, and $E_x^{(0)}$ are obtained from the static (Poisson's) equations. Once the static quantities are obtained, the program is ready to solve the set of equations for the fundamental mode. Note that the fundamental mode is governed by a set of nonlinear equations described in Chapter 3 and thus Newton's iterations are involved in the solution process. In order to improve the efficiency of Newton's iterations, an estimated value of the propagation factor $\gamma$ is obtained by solving a pure electromagnetic problem based on the uniform conductivity model [Appendix A, 28].

The estimated value is then used as the initial guess of the actual propagation factor $\gamma$ for solving the fundamental mode equations. To maximize the convergence rate of Newton's iterations, it is a common practice to first solve a simplified yet closely related problem, and then use the solution from the simplified problem as the initial guess to the original problem.

Once the fundamental mode equations are solved, high order harmonic equations are linear and thus can be easily solved using linear matrix solvers. The output quantities from the device level simulation include the propagation factor $\gamma$, electromagnetic fields $E_z^{(m)}$, $E_x^{(m)}$, and $H_y^{(m)}$, carrier concentrations $n^{(m)}$, $p^{(m)}$, and power flows $P_s^{(m)}$ (where $m = 1, 2, \cdots$) besides the static quantities $n^{(0)}$, $p^{(0)}$, and $E_x^{(0)}$.

### 5.1.2: ELECTROMAGNETIC ANALYSIS CAPABILITY

In order to perform device level simulation for wave propagation along MIS interconnects, electromagnetic analysis capability must be added into the PROPHET program. This task can be accomplished by introducing new physical operators to the software framework.

In the PROPHET framework, a variable defined over the meshed solution domain is called a field [87]. The physical operators take fields or their derivatives as inputs and then form fluxes by combining these fields or derivatives together in various ways. Table 5.1 lists the newly created physical operators for electromagnetic analysis in PROPHET framework. All these physical operators are implemented in the C language, which is the primary language for the computer code in the PROPHET simulator. All the code for these physical operators are tightly and seamlessly integrated with the rest of PROPHET.

| | |
|---|---|
| **Associated with divergence operators** | |
| em_dix_x | The $x$ component of diffusion currents |
| em_dix_y | The $y$ component of diffusion currents |
| em_dix_xy | Two-dimensional vector of diffusion currents |
| **Associated with the derivative nodal operator** | |
| em_carrier_field | Terms $F_n^{(m,s)}$ or $F_p^{(m,s)}$ |
| em_carrier_field0 | Terms $G_n^{(m)}$ or $G_p^{(m)}$ |
| em_field_Ex_1d | The $x$ component of electric field |
| em_field_Hy_prop | The $y$ component of magnetic field |
| em_source_x | Term $-jm\omega\mu\left[J_{nx}^{(m)}+J_{px}^{(m)}\right]-\frac{q}{\varepsilon}\frac{\partial}{\partial x}\left[p^{(m)}-n^{(m)}\right]$ |
| em_source_y | Term $-jm\omega\mu\left[J_{ny}^{(m)}+J_{py}^{(m)}\right]-\frac{q}{\varepsilon}\frac{\partial}{\partial y}\left[p^{(m)}-n^{(m)}\right]$ |
| **Associated with nodal operators** | |
| em_carrier_prop | Terms $-\tilde{D}_n m^2\gamma^2 n^{(m)} + jm\omega n^{(m)} + u^{(m)}$ or $\tilde{D}_p m^2\gamma^2 p^{(m)} - jm\omega p^{(m)} - u^{(m)}$ |

| | |
|---|---|
| em_conductivity | Calculate the semiconductor conductivity from carrier concentrations |
| em_dix_prop | The *z* component of diffusion currents |
| em_drift | The drift currents due to the ac electric fields |
| em_drift0 | The drift currents due to the dc electric field |
| em_drift_dix_prop | The total currents due to the ac electric fields |
| em_power | Normalized complex time-average power |
| em_prop | Terms $m^2\left(k_c^2+\gamma^2\right)E_x^{(m)}$, $m^2\left(k_c^2+\gamma^2\right)E_y^{(m)}$, or $m^2\left(k_c^2+\gamma^2\right)E_z^{(m)}$ |
| em_source_prop | Term $-jm\omega\mu\left[J_{nz}^{(m)(r)}+J_{pz}^{(m)(r)}\right]+\frac{qm\gamma}{\varepsilon}\left[p^{(m)}-n^{(m)}\right]$ |
| **Associated with interface operators** | |
| em_boundary_Ex_1d | Boundary condition for the *x* component of electric field |
| em_cal_eigen_1d | Scalar nonlinear equation for the propagation factor at the boundary |
| em_drift0_bd | Boundary condition for the dc drift currents |
| em_robin_1d | Third kind boundary condition for electric field |
| em_third_kind | Third kind boundary condition for currents |
| **Associated with the dirichlet operators** | |
| em_device_dirichlet | Boundary conditions for $n^{(0)}$, $p^{(0)}$, and $\phi$. |

| | |
|---|---|
| em_dirichelet_1d | Set boundary conditions for electromagnetic fields and estimate the propagation factor based on the uniform conductivity model |

Table 5.1: New physical operators for electromagnetic analysis

A sample PROPHET script file is included in Appendix B to illustrate how the physical operators in Table 5.1 can be used for electromagnetic analysis and device level simulation within PROPHET.

Electromagnetic analysis equations contain derivative terms. This translates into the fact that many physical operators listed in Table 5.1 involve a functional form $f(\mathbf{r}, v, \nabla v)$, where $v$ is an unknown function. The discretization of the form $f(\mathbf{r}, v, \nabla v)$ was not immediately available in the PROPHET framework. A new geometrical operator, called the "derivative nodal operator", has been implemented for performing the discretization of $f(\mathbf{r}, v, \nabla v)$.

Moreover, in order to handling the scalar unknowns such as the propagation factor, the PROPHET framework has been also enhanced to support scalar variables that are defined by a unique value over the entire meshed solution domain. The scalar variable feature also enables numerical integration and provides integral equation capability in the PROPHET framework. Note that the PROPHET framework was originally designed to treat partial differential equations.

Both the derivative nodal operator and scalar variable concept will be discussed in the next subsection.

### 5.1.3: MISCELLANEOUS ENHANCEMENTS

In this subsection, newly developed features in the PROPHET simulator are discussed. These new features include the derivative nodal operator and scalar variable support.

### 5.1.3.1: The Derivative Nodal Operator

The only derivative terms previously supported by the PROPHET framework involved divergence terms. The divergence terms are differential forms and thus their weak form can be evaluated from lower dimensional integrals by virtue of Stokes' theorem [88]. In order to handle the derivative terms other than divergence operators, the derivative nodal operator, i.e., *dnodal*, has been implemented in the PROPHET framework to perform the discretization of the form $f(\mathbf{r}, v, \nabla v)$.

Analytically, if an unknown function to partial differential equations is determined, its derivative is then well defined and can be completely determined from the function itself by differentiation. However, it is not necessary that the quantity is to be valid numerically. Consider an unknown function $U(\mathbf{r})$ expanded in a series of basis functions as follows:

$$U(\mathbf{r}) = \sum_{i=1}^{M} U_i \, \psi_i(\mathbf{r}) \tag{5.1}$$

where $\{\psi_i(\mathbf{r})\}_{i=1,\cdots,M}$ is the set of basis functions over the solution domain. It is common that the basis functions are only of $C^0$ continuity and $\{\nabla \psi_i(\mathbf{r})\}_{i=1,\cdots,M}$ may not be well defined over some regions of measure zero such as element boundaries. Therefore, it would be *invalid* to specify the derivatives as

$$\nabla U(\mathbf{r}) = \sum_{i=1}^{M} U_i \, \nabla\psi_i(\mathbf{r}) \tag{5.2}$$

since $\{\nabla \psi_i(\mathbf{r})\}_{i=1,\cdots,M}$ may not exist everywhere in the solution domain.

However, the functional integrals

$$\mathbf{F}_i[W] = \int_{\text{Solution Domain}} W(\mathbf{r}) \nabla \psi_i(\mathbf{r}) d\sigma \qquad i = 1, \cdots, M \tag{5.3}$$

are well defined for any function $W(\mathbf{r})$ of $C^0$ continuity. Hence, one can define a new unknown vector function $\mathbf{G}(\mathbf{r})$ of the form:

$$\mathbf{G}(\mathbf{r}) = \sum_{i=1}^{M} \mathbf{G}_i \, \psi_i(\mathbf{r}) \tag{5.4}$$

such that

$$\int_{\text{Solution Domain}} W(\mathbf{r})\mathbf{G}(\mathbf{r})d\sigma = \sum_{i=1}^{M} U_i \, \mathbf{F}_i[W] \tag{5.5}$$

Then, the unknown function $\mathbf{G}(\mathbf{r})$ is equivalent to the derivatives $\nabla U(\mathbf{r})$ in a weak sense. The unknown function $\mathbf{G}(\mathbf{r})$ can be defined as the numerical gradient of $U(\mathbf{r})$. Substitution of (5.3) and (5.4) in (5.5), one obtains

$$\sum_{i=1}^{M} \mathbf{G}_i \int_{\text{Solution Domain}} W(\mathbf{r})\psi_i(\mathbf{r})d\sigma = \sum_{i=1}^{M} U_i \int_{\text{Solution Domain}} W(\mathbf{r})\nabla \psi_i(\mathbf{r})d\sigma \tag{5.6}$$

By selecting $W(\mathbf{r}) = \psi_j(\mathbf{r}) \; (j = 1,\cdots,M)$ in (5.6), one obtains $M$ vectorial linear equations, which can be utilized to determine unknown coefficients $\mathbf{G}_i$.

Based on the basic ideas stated as above, the discretization of the form $f(\mathbf{r}, v, \nabla v)$ can be implemented in the same manner as the numerical gradient. The *dnodal* operator is a finite element realization for the discretization of the form $f(\mathbf{r}, v, \nabla v)$ in the PROPHET framework.

### 5.1.3.2: Scalar Variable Support

An unknown variable is generally represented as a field after discretization in the PROPHET framework. The most common fields are nodal fields, which are completely specified by their nodal values over the meshed solution domain. The number of degrees of freedom of a nodal field is equal to the total number of nodes over the meshed solution domain.

However, some unknown variables such as the propagation factor are not spatial dependent. Hence, a nodal field is not a suitable discrete representation for such a spatial invariant variable. A new type of field, called scalar field, can be introduced to represent these spatial invariant unknown variables. A scalar field takes a unique value over the entire meshed solution domain. The number of degrees of freedom of a scalar field is equal to one. The scalar fields were not originally supported in the PROPHET framework. In order to solve for the propagation factor, the PROPHET framework has been enhanced to support scalar fields.

The scalar field feature also enables the evaluation of integral equations within the PROPHET framework. In an integral equation, the variables in the integrand are generally spatial dependent, whereas the integral value is spatial invariant. Therefore, the variables in the integrand can be represented as nodal fields, while the integral itself should be defined as a scalar field.

## 5.2: SOFTWARE REALIZATION OF CIRCUIT MODEL EXTRACTION

The extraction of an equivalent circuit model for MIS interconnects is implemented using the C++ language. This circuit model extractor is a standalone program, which includes two capabilities. The primary capability is to extract the equivalent circuit elements from the device level simulation results using the energy-based approach. Another capability is to compute the equivalent circuit elements based on the uniform conductivity model [Appendix A, 28]. In the latter, only linear circuit elements can be computed. The basic C++ data structures of the extraction program are included in Appendix C.

When the extraction program is employed to extract the equivalent circuit elements from the device level simulation results, the required inputs to the program include the material properties, geometrical parameters, operating frequency, propagation factor, total number of harmonics, and normalized power flow resulting from each harmonic. The output information includes the characterization impedance, attenuation and phase constants, and equivalent linear and nonlinear circuit elements per unit length.

For the circuit extraction using the uniform conductivity model, the inputs to the program must contain the information about the material properties, geometrical parameters, and operating frequency. The propagation factor and electromagnetic fields are computed by solving a pure electromagnetic problem inside the program. The output data includes the characteristic impedance, attenuation and phase constants, and equivalent linear circuit elements per unit length.

## 5.3: SUMMARY

This chapter has briefly discussed the computer software implementation of device level frequency domain (DLFD) simulation and circuit extraction. The device level simulation of wave propagation along MIS interconnects has been realized within the PROPHET framework. In order to perform the device level simulation for wave propagation, electromagnetic analysis capabilities were added into the PROPHET framework. More than two-dozen new physical operators were developed in the PROPHET framework for the device level simulation. A flowchart of the device level simulation was illustrated.

In order to treat the derivative terms in a general manner, a derivative nodal operator was implemented in the PROPHET framework by using the finite element discretization. In addition, the scalar field was introduced into the PROPHET framework to enable inclusion of spatial invariant variables such as the propagation factor and integrals over the solution domain.

The extraction of an equivalent circuit model for MIS interconnects has been implemented as a standalone program. This circuit extraction program includes two capabilities: the circuit extraction from the device level simulation results and the circuit extraction based on the uniform conductivity model.

# CHAPTER 6: EXAMPLES AND DISCUSSIONS

In this chapter, numerical results are presented to validate the computer software implementations and demonstrate capabilities of the device level frequency domain (DLFD) simulation scheme as well as the circuit model extraction. The numerical results are compared with both measurements and previously published data. The device level approach provides many new insights to propagation characteristics of MIS interconnects, including field-carrier interactions, semiconductor substrate loss and nonlinearity, external bias effect, slow-wave effect, and screening effect of charged carriers. Discussions on the device level simulation results as well as the equivalent nonlinear circuit models are included.

## 6.1: DEVICE LEVEL SIMULATION OF WAVE PROPAGATION

In this section, numerical results are presented for device level simulation of wave propagation along MIS interconnects. By comparison with previously published data, the computer software realizations of device level simulation are validated. Numerical results also demonstrate capabilities of the device level simulation scheme and give new insight into field-carrier interactions, semiconductor substrate loss and nonlinearity, external bias effect, slow-wave effect, and screening effect of charged carriers.

For all the numerical examples in this section, the following geometrical parameters and material properties were assumed: $\varepsilon = 11.9\varepsilon_0$, $\varepsilon_d = 3.9\varepsilon_0$, $\mu = \mu_d = \mu_0$, $\mu_n = 1500$ $\mathrm{cm}^2/(\mathrm{v}\cdot\mathrm{s})$, $\mu_p = 450\ \mathrm{cm}^2/(\mathrm{v}\cdot\mathrm{s})$, $D_n = \mu_n \kappa T / q$, $D_p = \mu_p \kappa T / q$, $T = 300$ K,

$\tau_n = 2.2156\times10^{-13}\,\text{s}$, $\tau_p = 5.2706\times10^{-14}\,\text{s}$, $h_d = 0.05\,\mu\text{m}$, and $h_c = 100\mu\text{m}$, where $\varepsilon_0$ and $\mu_0$ are, respectively, the permittivity and permeability in vacuum, and $\kappa$ is the Boltzmann constant. The semiconductor was assumed to be *n*-type silicon with donor impurity concentration $N_d = 10^{17}\,\text{cm}^{-3}$. The metal work function was chosen in such a way that a flat-band condition would be attained in the absence of external bias. Under the assumption of small disturbance from equilibrium, the net recombination rates can be approximately expressed as $u^{(m)} = p^{(m)} / t_p$ by virtue of the Shockley-Read-Hall recombination model. The hole lifetime $t_p$ was taken to be $2.5\times10^{-3}\,\text{s}$ in the calculation.

In order to tackle the boundary layer nature, the mesh grid takes a much smaller size at a location closer to the interface at $x = 0$. In specific, the mesh size starts as small as $10^{-5}\,\mu\text{m}$ at $x = 0$, and gradually increases to $5\,\mu\text{m}$ at $x = 100\mu\text{m}$. By so doing, the mesh grid is fine enough to capture the boundary layer behavior in the accumulation-depletion layer, whereas keeps the entire problem manageable by easily accessible computing resources such as personal computers. The utilization of sparse matrix techniques results in an algorithm of complexity $O(N^2)$, where $N$ denotes the total number of unknowns.

The characteristics of the wave propagation along the MIS interconnect structure are investigated using the device level simulation scheme. The field components and carrier concentrations for the fundamental mode, the second order harmonic, and the third order harmonic are computed at a fundamental frequency $f = 5\,\text{GHz}$, when an excitation with $A^{(1)} = 10^3\,\text{v/cm}$ was applied. The cases with three different external bias conditions, i.e., negative bias –0.1v, no bias, and positive bias +0.1v, were examined.

### 6.1.1: FUNDAMENTAL MODE AND PROPAGATION CHARACTERISTICS

Figure 6.1 through Figure 6.4 illustrate the magnitude distributions of field components and carrier concentrations for the fundamental mode at a fundamental frequency

$f = 5\,\text{GHz}$, when an excitation with $A^{(1)} = 10^3\ \text{v/cm}$ was applied. The plots are shown for three different external bias conditions: negative bias –0.1v, no bias, and positive bias +0.1v.

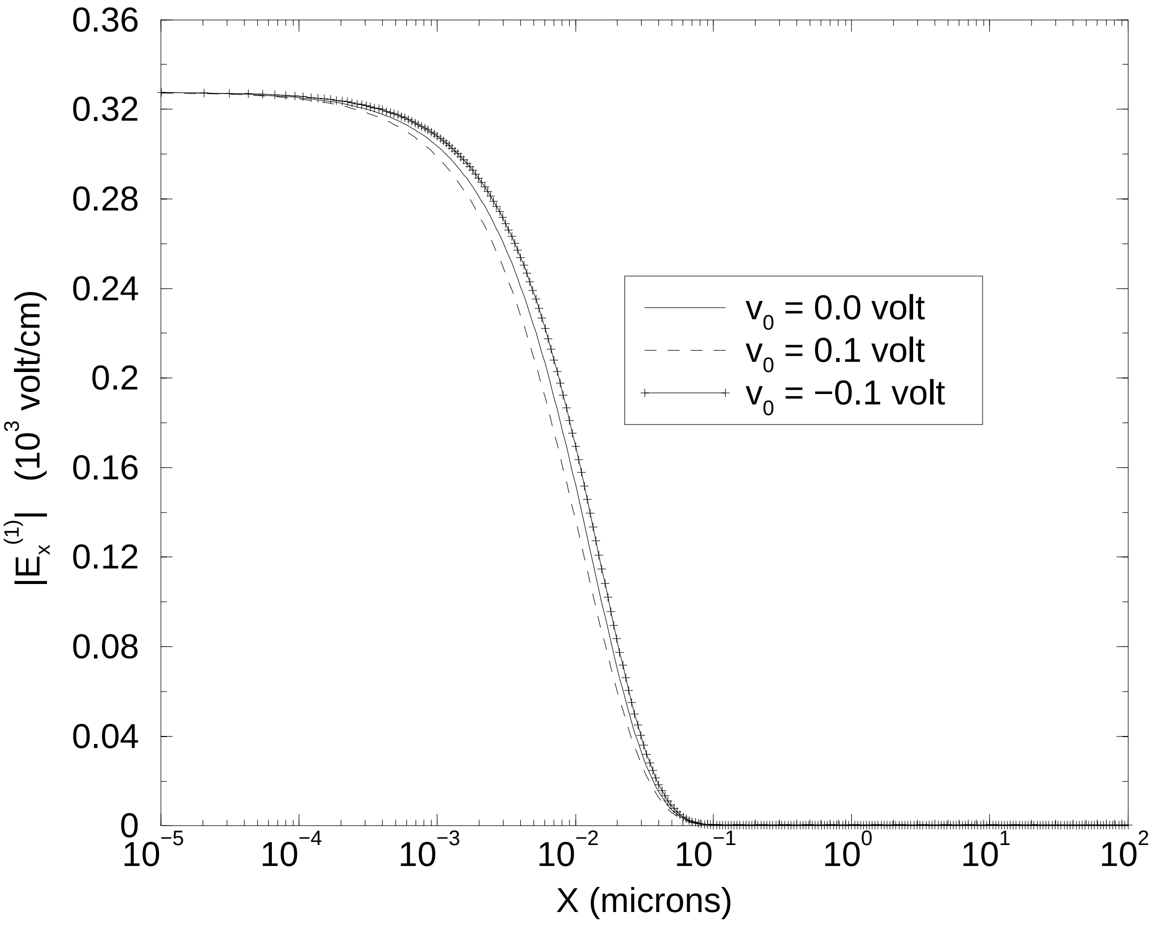

Figure 6.1: Magnitude of electric field component $E_x^{(1)}$ of the fundamental mode in the semiconductor.

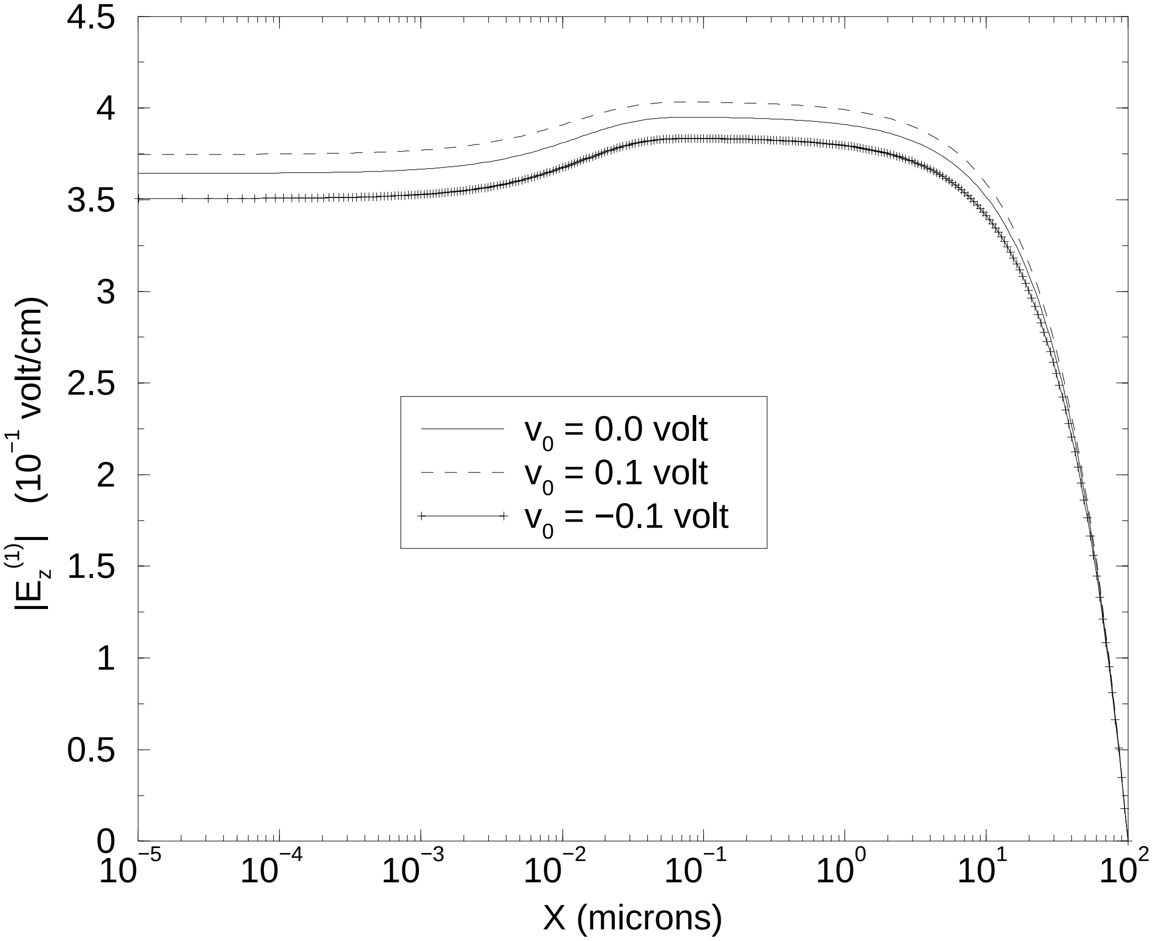

Figure 6.2: Magnitude of electric field component $E_z^{(1)}$ of the fundamental mode in the semiconductor.

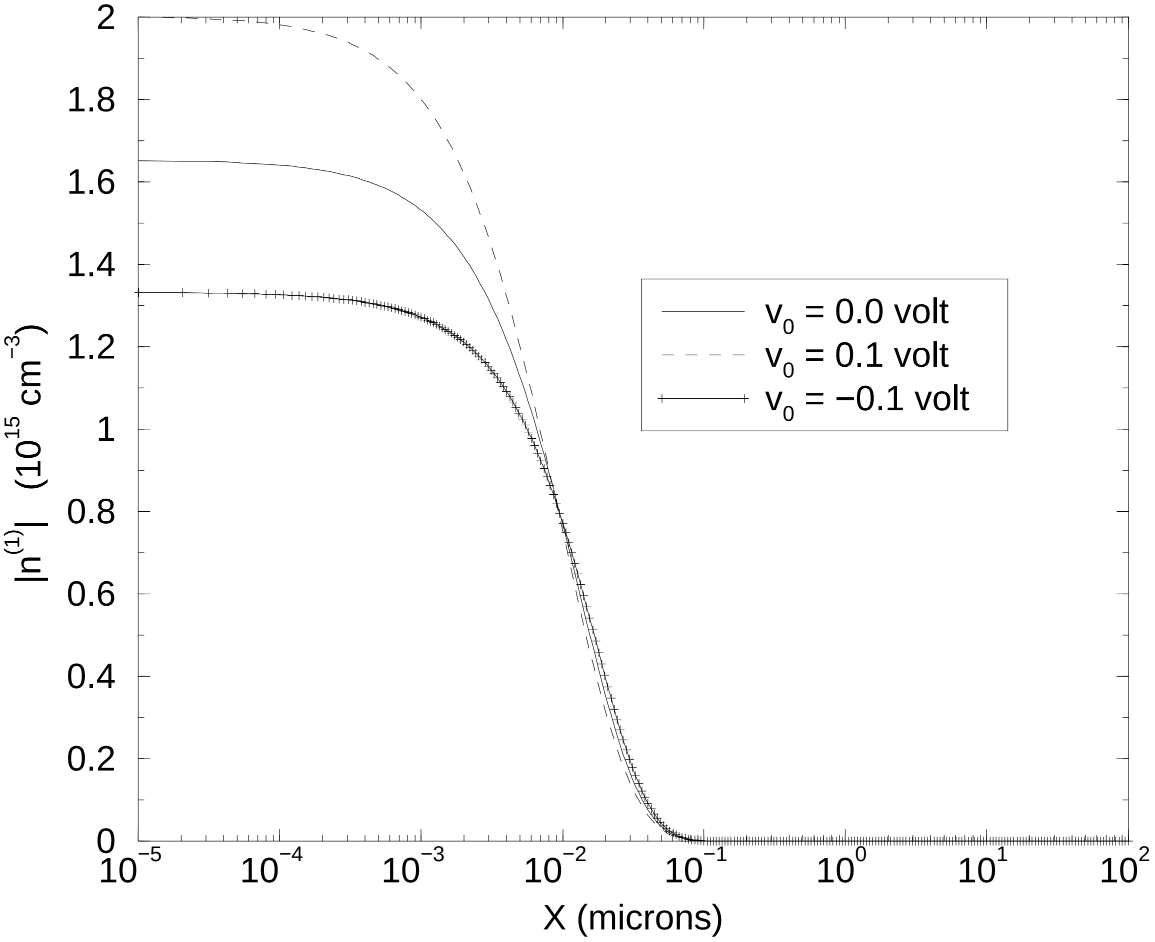

Figure 6.3: Magnitude of electron concentration $n^{(1)}$ of the fundamental mode in the semiconductor.

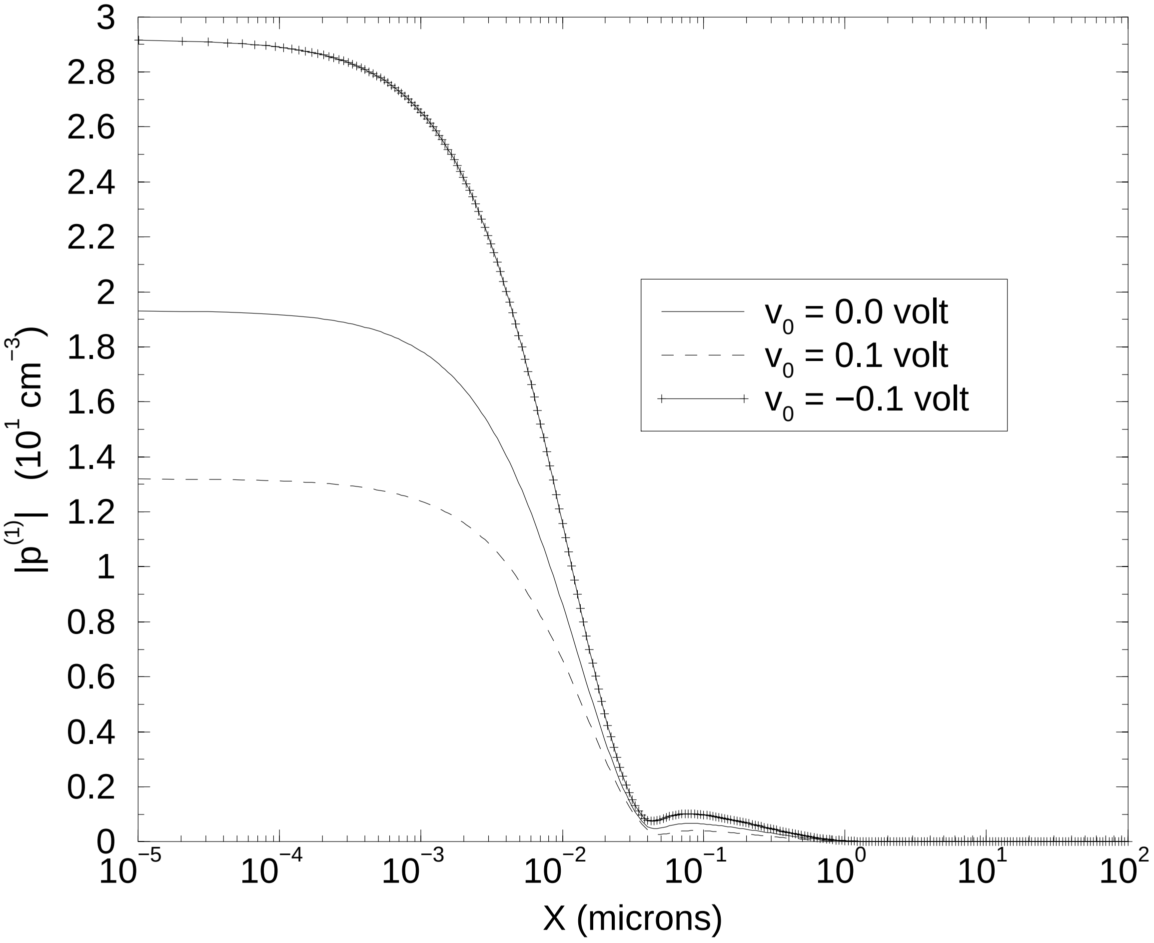

Figure 6.4: Magnitude of hole concentration $p^{(1)}$ of the fundamental mode in the semiconductor.

For the three external bias conditions: negative bias –0.1v, no bias, and positive bias +0.1v, the propagation factor $\gamma$ was obtained as $0.0024549 + j0.0065734$, $0.0026608 + j0.0067883$ and $0.002938 + j0.0068985$ respectively. The real part of propagation factor gives the attenuation constant $\alpha$, whereas its imaginary part corresponds to the phase constant $\beta$. The above values of propagation factor result in the normalized phase constant $\beta/k_0$ = 62.7279, 64.7787, and 65.8303 and the attenuation constant 21.323, 23.114, and 25.5191 dB/mm respectively, where $k_0$ denotes the wave number in vacuum. The large ratio between the phase constant and the vacuum wave number indicates that the MIS waveguide structure exhibits a slow-wave phenomenon. Moreover, the attenuation constant provides a direct account for the semiconductor substrate loss.

Some phenomena reported in the small signal analysis of [42] can be observed in the solution of the fundamental mode, as shown in Figure 6.1 through Figure 6.4. In most previous work on studying MIS structures (e.g., see [6, 26-40]), semiconductor substrates were described by a uniform conductivity model in which semiconductor substrates are treated as uniform lossy materials and the electrical property of a semiconductor is characterized by its conductivity and dielectric constant. Using such a uniform conductivity model [28, Appendix A], the propagation factor can be readily obtained as a complex value $0.0027554 + j0.00686443$, which provides a close approximation to the actual result attained using the device level simulation. Nevertheless, the device level simulation is able to offer detailed information regarding field-carrier interaction mechanisms as well as external bias effect, whereas the uniform conductivity model fails to do so.

The device level simulation shows a strong coupling effect between the transverse component $E_x^{(1)}$ of electrical field and charged carriers, which leads to a completely different solution in the accumulation-depletion layer from that predicted by the uniform conductivity model. As indicated in the plots, the screening effect of charged carriers near the accumulation-depletion layer prevents the electrical field from penetrating the semiconductor to beyond a few Debye lengths.

### 6.1.2: HIGH ORDER HARMONICS

This device level simulation is capable of investigating the nonlinearity effect and predicting harmonics quantitatively. Figure 6.5 through Figure 6.12 illustrate the magnitude distributions of field components and carrier concentrations for the second and third harmonics at a fundamental frequency $f = 5\,\text{GHz}$, when an excitation with $A^{(1)} = 10^3\ \text{v/cm}$ was applied. The plots are again shown for three different external bias conditions: negative bias –0.1v, no bias, and positive bias +0.1v.

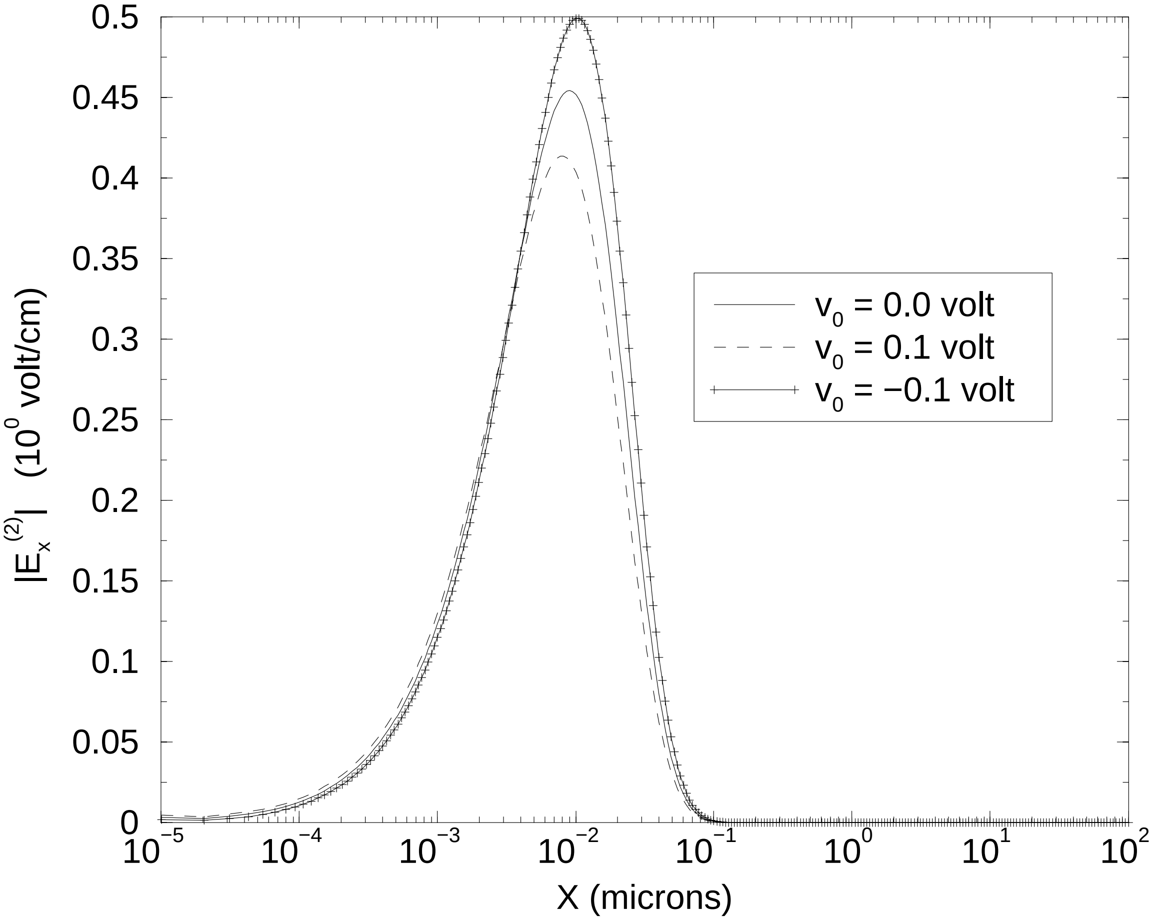

Figure 6.5: Magnitude of electric field component $E_x^{(2)}$ of the second harmonic in the semiconductor.

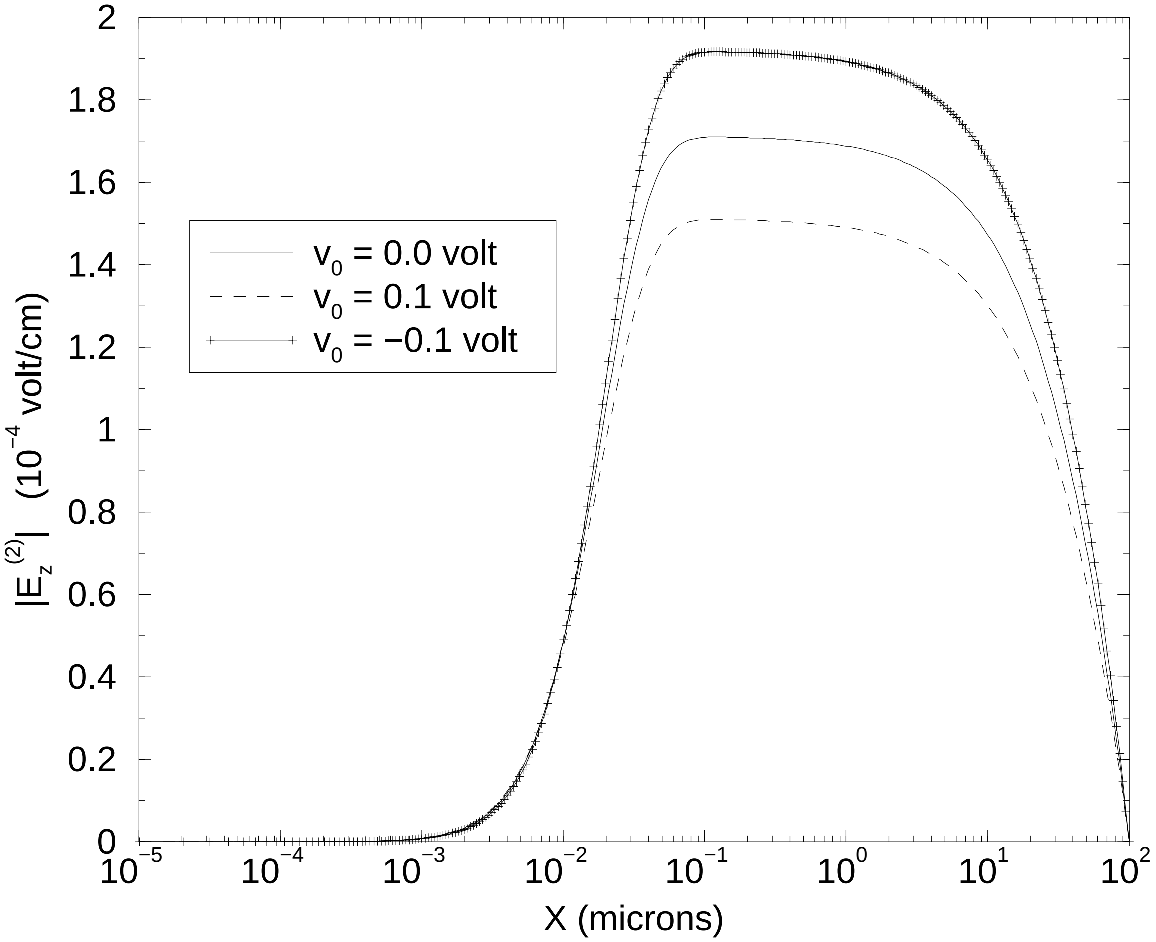

Figure 6.6: Magnitude of electric field component $E_z^{(2)}$ of the second harmonic in the semiconductor.

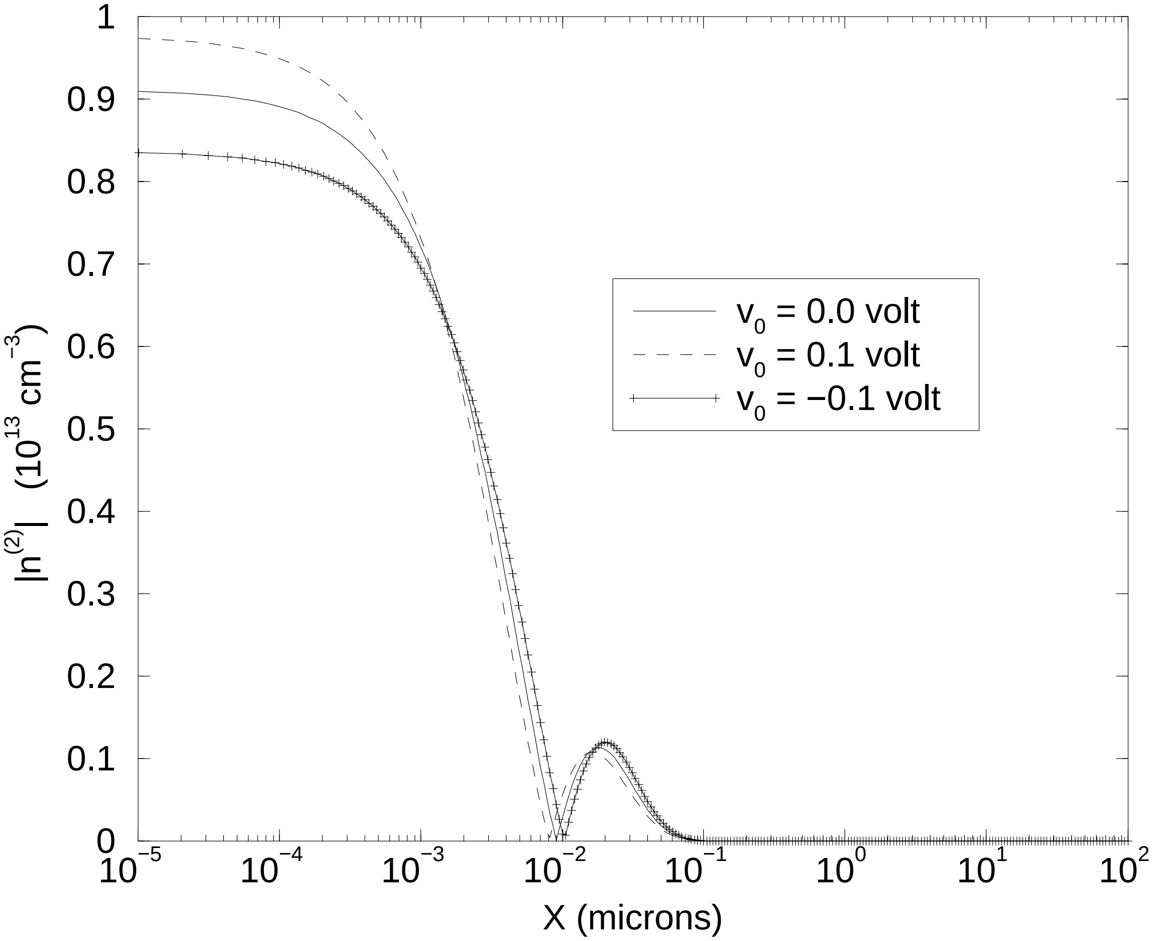

Figure 6.7: Magnitude of electron concentration $n^{(2)}$ of the second harmonic in the semiconductor.

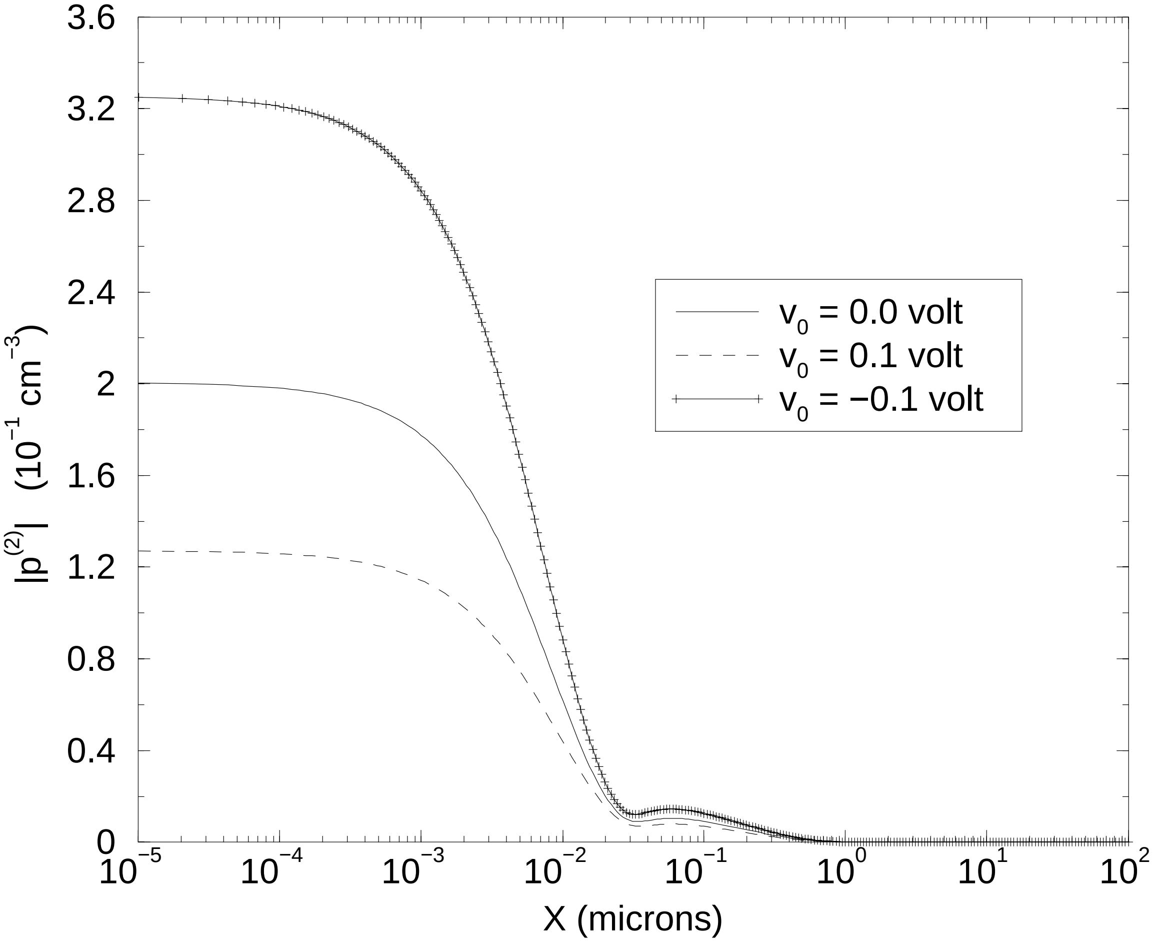

Figure 6.8: Magnitude of hole concentration $p^{(2)}$ of the second harmonic in the semiconductor.

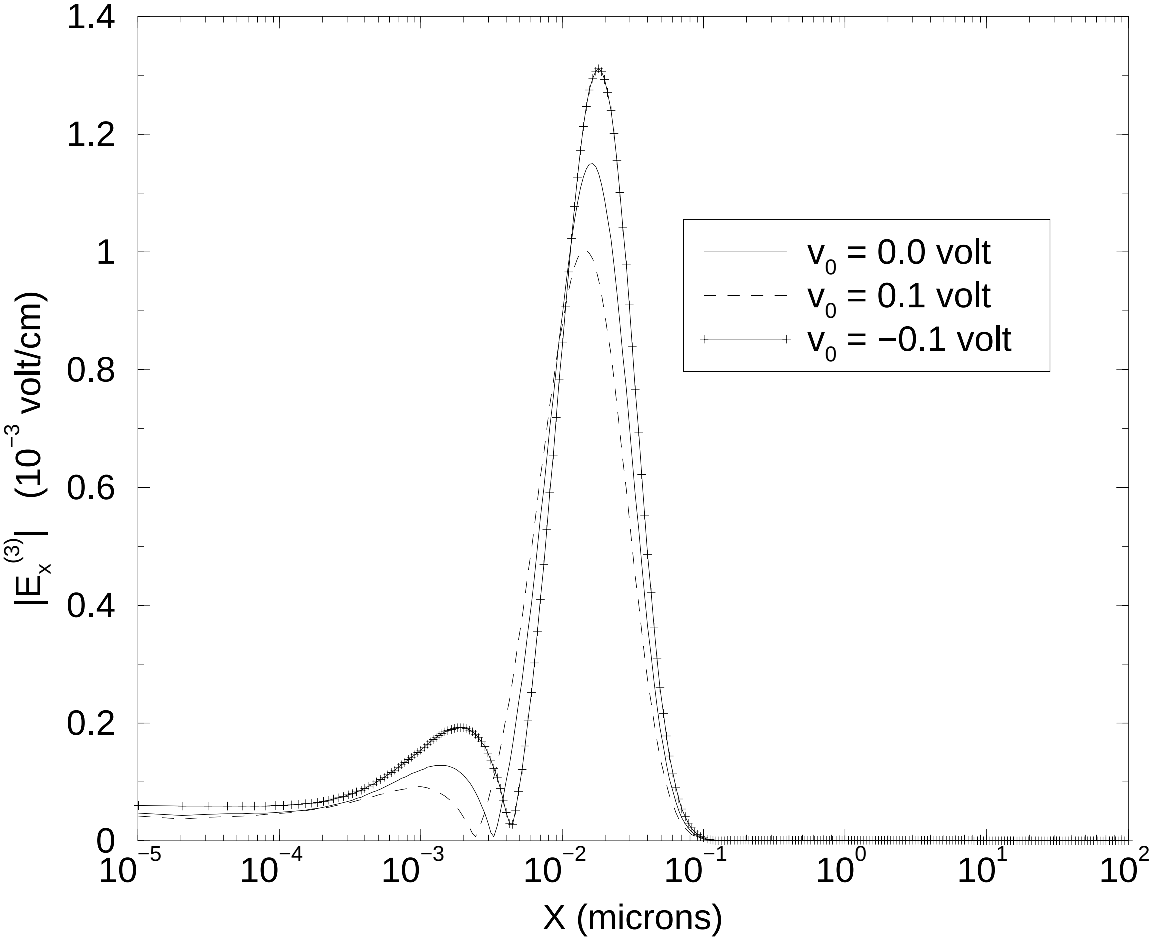

Figure 6.9: Magnitude of electric field component $E_x^{(3)}$ of the third harmonic in the semiconductor.

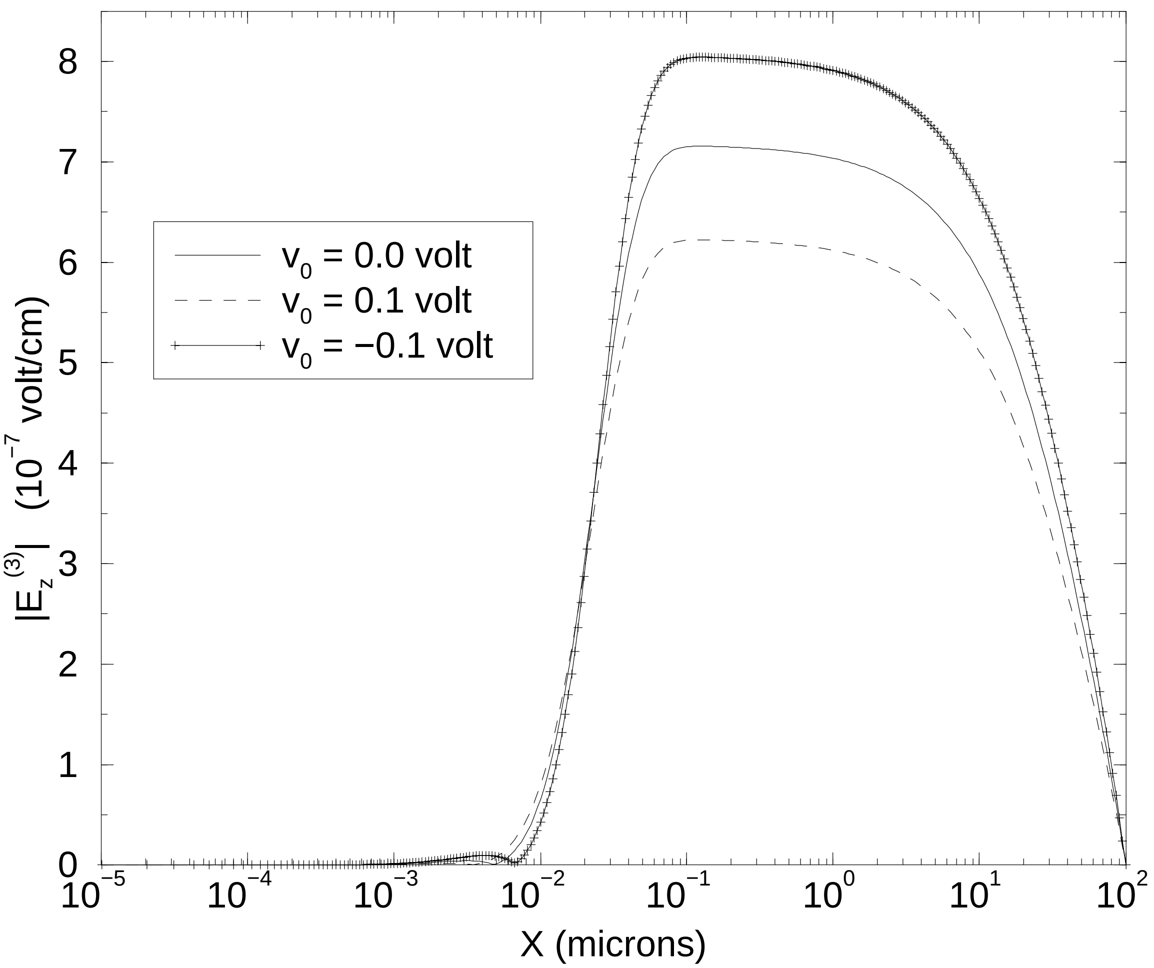

Figure 6.10: Magnitude of electric field component $E_z^{(3)}$ of the third harmonic in the semiconductor.

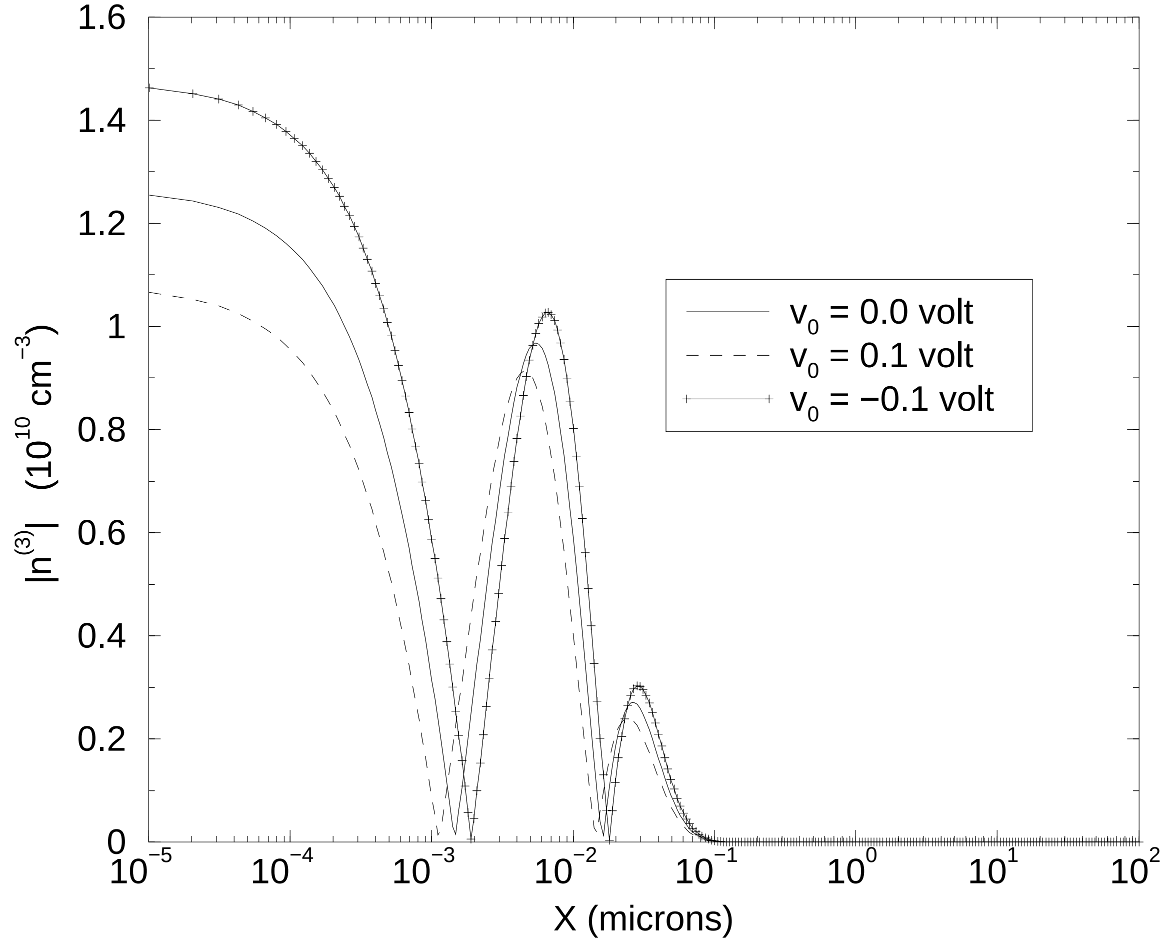

Figure 6.11: Magnitude of electron concentration $n^{(3)}$ of the third harmonic in the semiconductor.

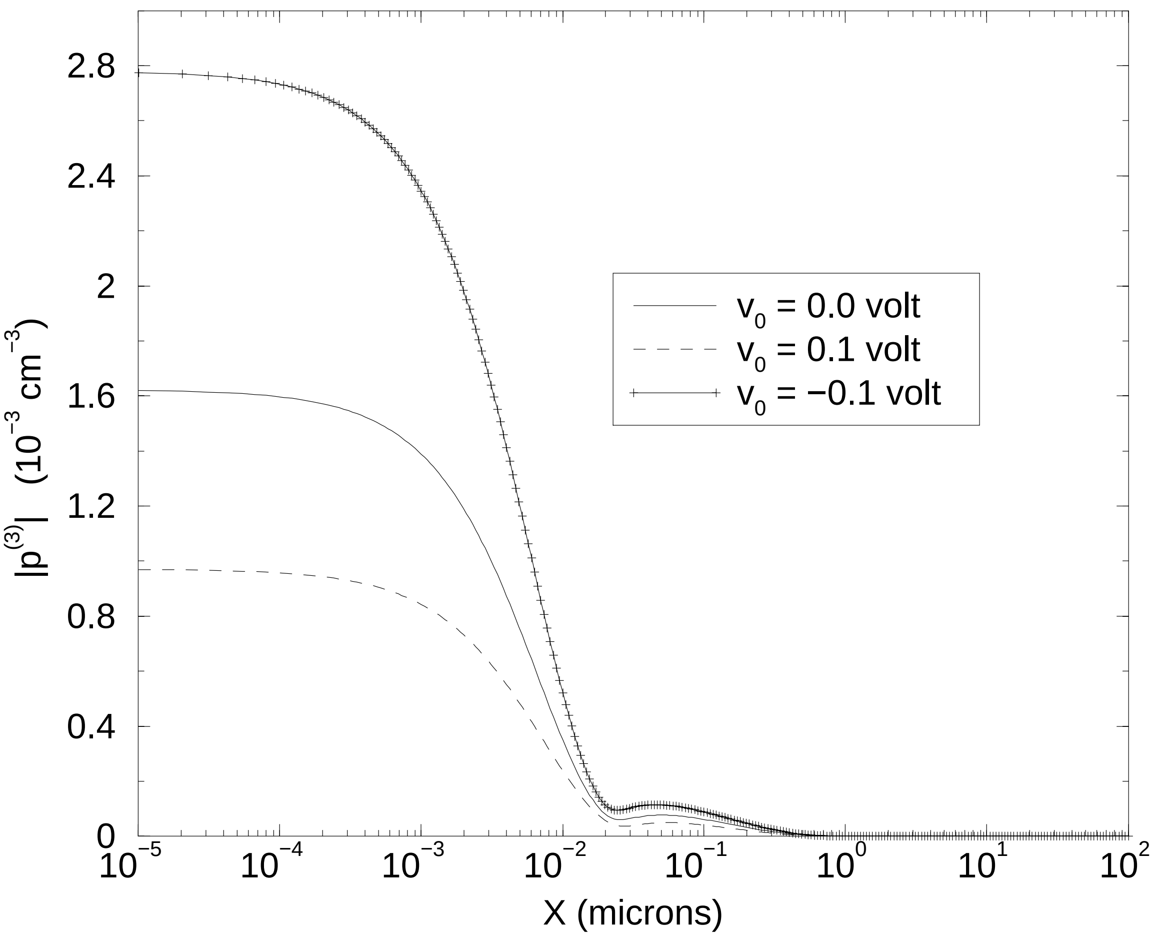

Figure 6.12: Magnitude of hole concentration $p^{(3)}$ of the third harmonic in the semiconductor.

It is of interest to note that some sidelobes appear in the amplitude plots of majority carrier concentrations for high order harmonics. The second harmonic is generated by field-carrier interactions among the fundamental mode, whereas the third harmonic is due to field-carrier interactions between the fundamental mode and the second harmonic. Therefore, intuitively, the second harmonic is expected to act in more complex way than the fundamental mode. Moreover, the third harmonic might exhibit even wilder behavior than the second harmonic. The intuition agrees well with the simulation results, as shown by Figure 6.5 through Figure 6.12, where more sidelobes are observed for a higher order harmonic. Moreover, the location where the electric field $E_x^{(2)}$ reaches its maximum coincides with the zero-crossing point of the majority carrier concentration $n^{(2)}$. A similar phenomenon to the third harmonic can be also observed between the electric field $E_x^{(3)}$ and the majority carrier concentration $n^{(3)}$. The zero-crossing points correspond to the regions where the majority carrier concentrations undertake rapid changes, which could induce strong electric fields locally.

The simulations were also performed for several other excitations with $A^{(1)}$ ranging from $10^{-2}\,\mathrm{v/cm}$ to $10^{5}\,\mathrm{v/cm}$. For each of these excitations, plots identical to Figure 6.1 through Figure 6.12 can be obtained except that appropriate scaling factors need to be used. In Figure 6.1 through Figure 6.12, the scaling factors are shown in the brackets along with the units at the vertical axis labels, that is, the scaling factors are $10^{3}$, $10^{-1}$, $10^{15}$, $10$, $10^{0}$, $10^{-4}$, $10^{13}$, $10^{-1}$, $10^{-3}$, $10^{-7}$, $10^{10}$, and $10^{-3}$ for unknowns $E_x^{(1)}$, $E_z^{(1)}$, $n^{(1)}$, $p^{(1)}$, $E_x^{(2)}$, $E_z^{(2)}$, $n^{(2)}$, $p^{(2)}$,$E_x^{(3)}$, $E_z^{(3)}$, $n^{(3)}$, and $p^{(3)}$ respectively.

### 6.1.3: DEPENDENCE ON EXCITATION STRENGTH

The dependence of electromagnetic fields and carrier concentrations on the excitation strength was investigated by performing the device level simulation for numbers of excitations with $A^{(1)}$ ranging from $10^{-2}\,\mathrm{v/cm}$ to $10^{5}\,\mathrm{v/cm}$. For each of these excitations, plots identical to Figure 6.1 through Figure 6.12 can be obtained except that appropriate scaling factors need to be used. These scaling factors are an excellent measure for the order of magnitude of unknowns. Figure 6.13 through Figure 6.16 depict the scaling factors versus the excitation magnitude $A^{(1)}$ for all the interested unknown variables.

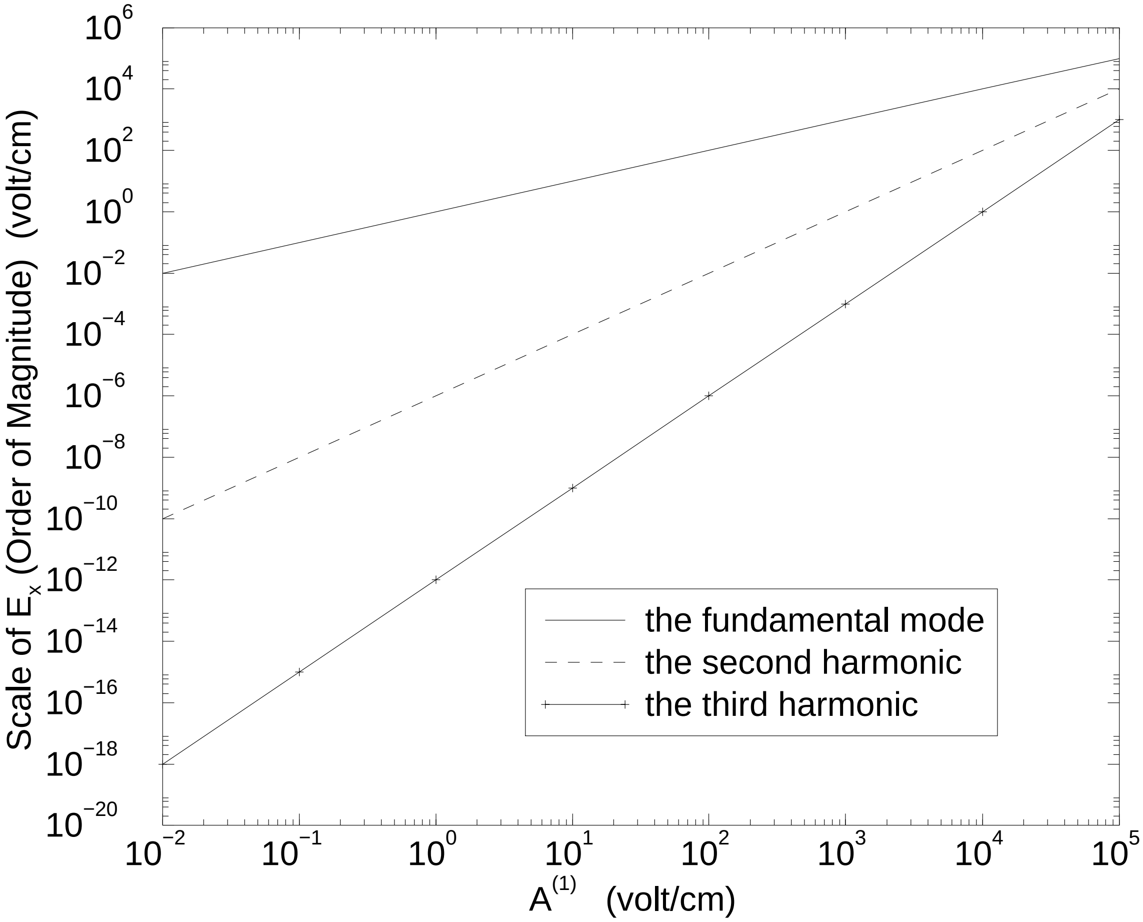

Figure 6.13: Scaling factors (orders of magnitudes) of the x components of electric field for the fundamental mode, second harmonic and third harmonic.

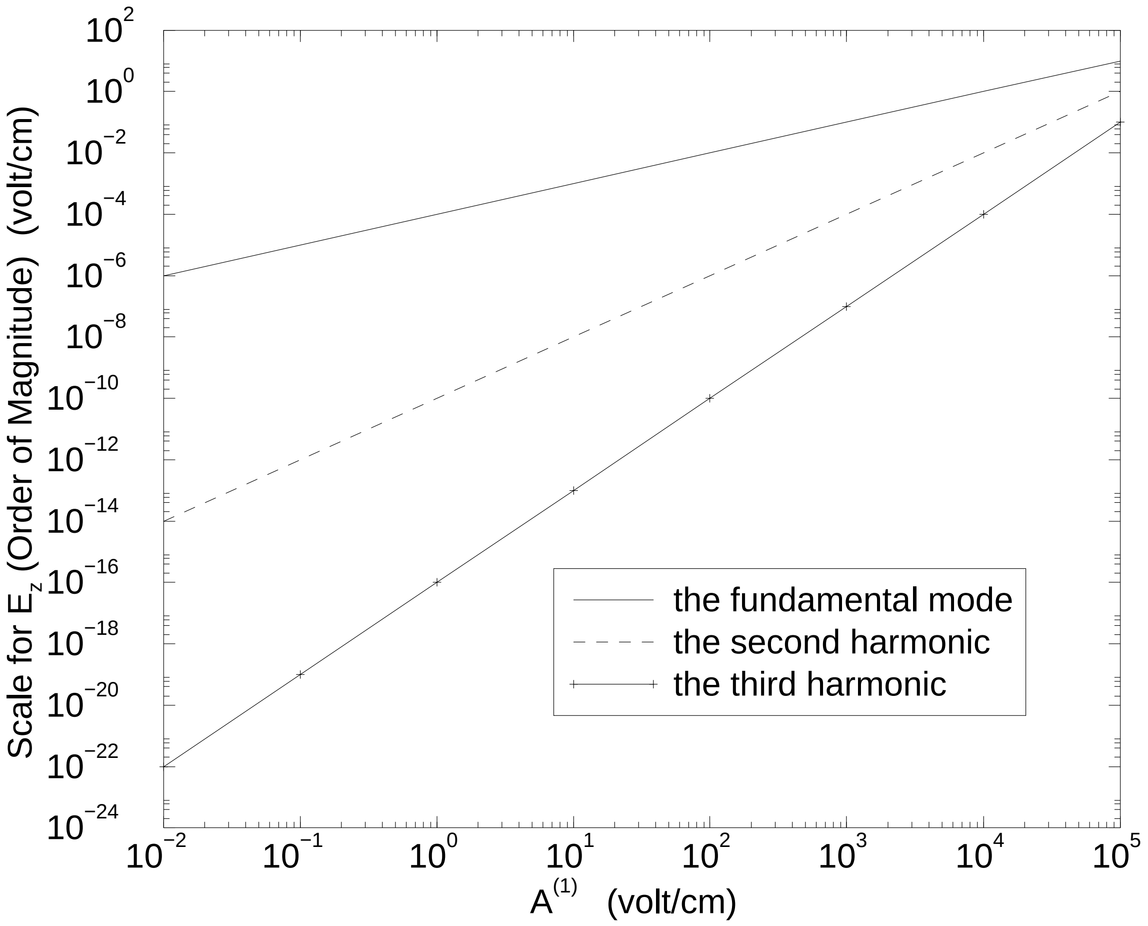

Figure 6.14: Scaling factors (orders of magnitudes) of the *z* components of electric field for the fundamental mode, second harmonic and third harmonic.

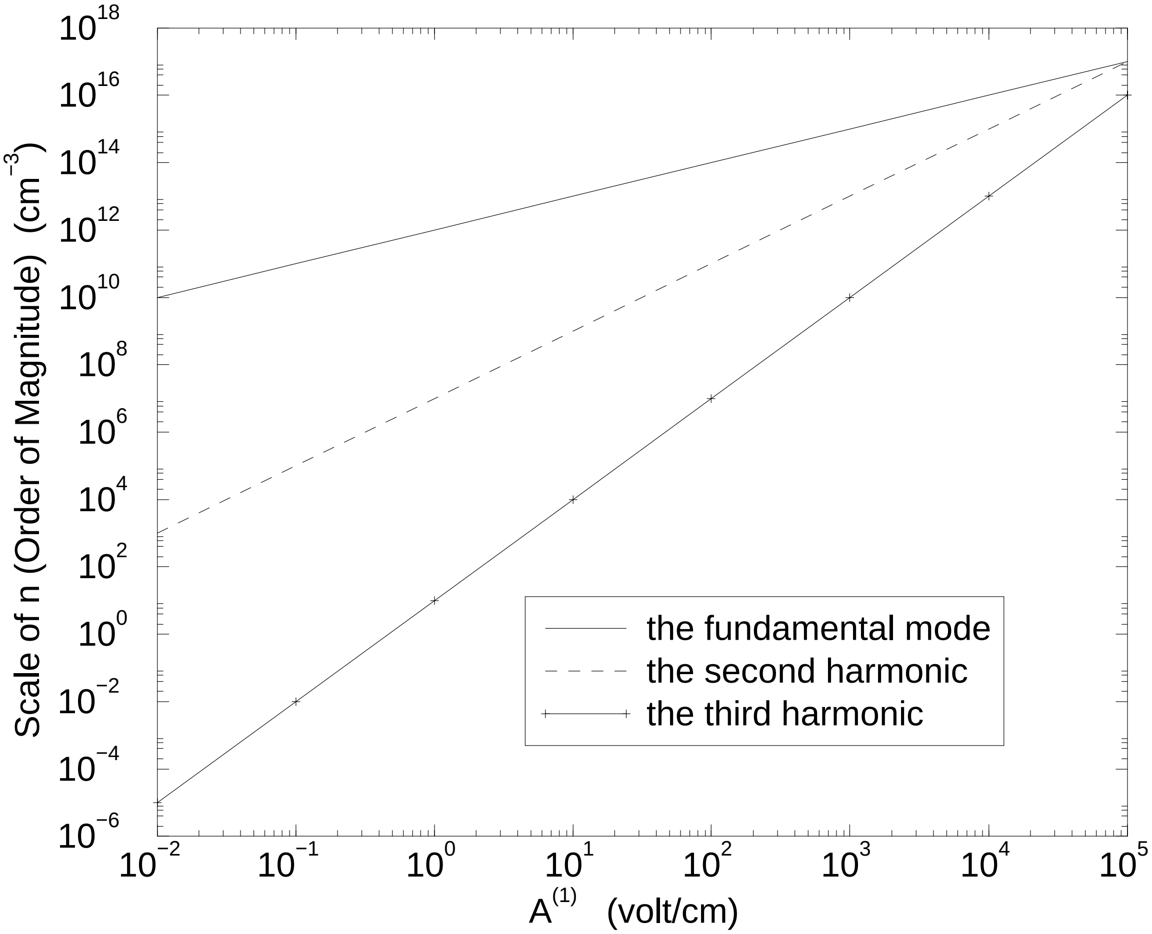

Figure 6.15: Scaling factors (orders of magnitudes) of the electron concentrations for the fundamental mode, second harmonic and third harmonic.

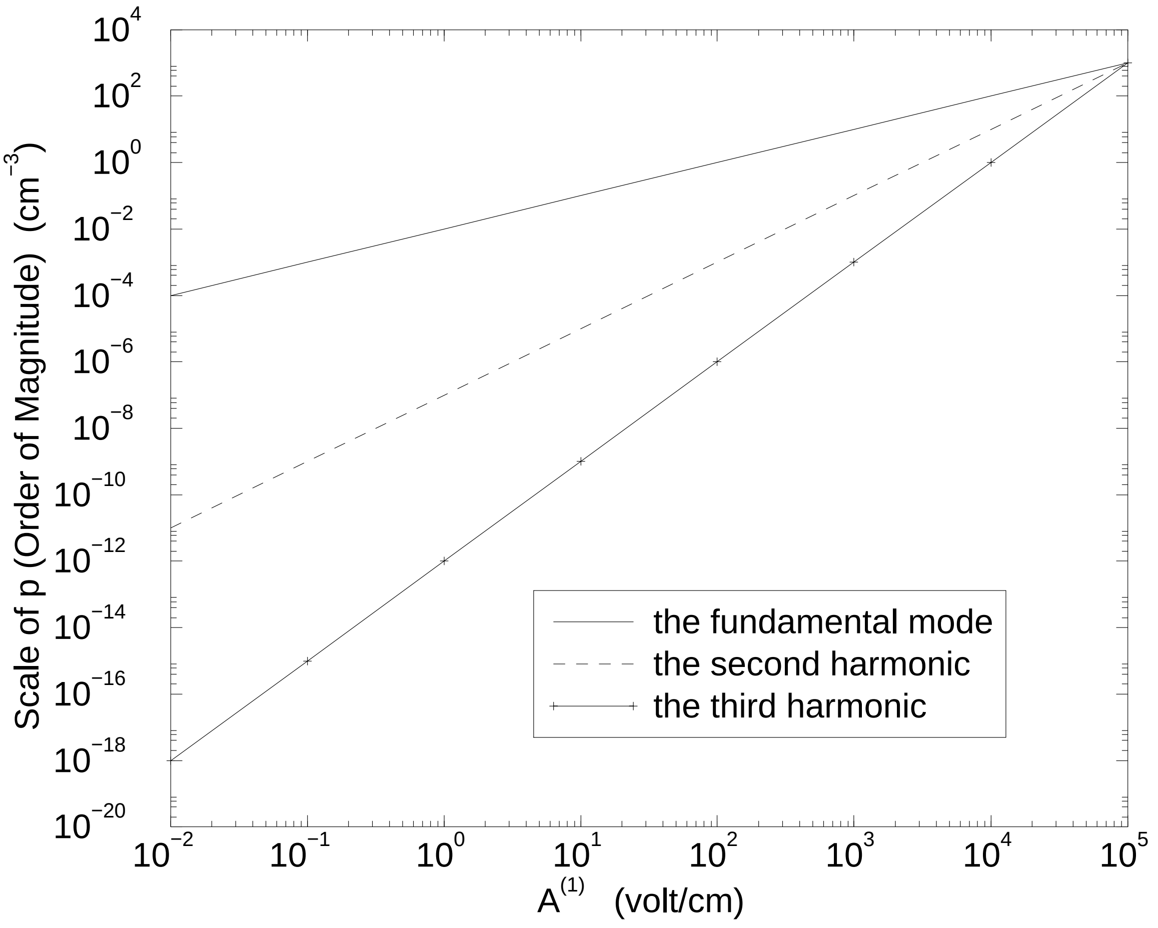

Figure 6.16: Scaling factors (orders of magnitudes) of the hole concentrations for the fundamental mode, second harmonic and third harmonic.

It can be both theoretically proven and numerically observed that the fundamental mode is linearly proportional to the excitation magnitude $A^{(1)}$. Using the fact, the fundamental mode for the excitation with $A^{(1)} = 10^{-2}\ \mathrm{v/cm}$ can readily obtained by scaling Figure 6.1 through Figure 6.4 with a factor $10^{-5}$, which gives results in a close agreement with those from the small signal analysis, i.e., Figure 6 through Figure 9 of [42]. Some slight discrepancies exhibited by the minority carrier concentration $p^{(1)}$ might be caused by a different recombination formula used in the calculation from that in [42]. Two distinct net recombination rates were employed in [42] for electrons and holes respectively, which might lead to a violation of the basic charge conservation principle. In this work, a single net recombination rate formula is applied to account for contributions from both electrons and holes, which eliminates this violation. The propagation factor $\gamma$ is usually a function of geometrical and material parameters and external bias but independent of the excitation strength. Hence, the propagation factors are the same for all the excitations.

Moreover, Figure 6.13 through Figure 6.16 reveal that the second and third harmonics are, respectively, proportional to $\left[A^{(1)}\right]^2$ and $\left[A^{(1)}\right]^3$. In general, it can be expected that the *m*-th harmonic is proportional to $\left[A^{(1)}\right]^m$. When the excitation becomes larger, the magnitudes of high order harmonics get closer and more comparable to the magnitude of the fundamental mode, and thus the nonlinearity becomes more severe. As shown in Figure 6.13 through Figure 6.16, the ratio between the magnitudes of a high order harmonic and the fundamental mode is becoming unity when $A^{(1)}$ is approaching $10^6\ \text{v/cm}$ and, equivalently, the maximum magnitude of $E_x^{(1)}$ is roughly approaching $3.27\times10^5\ \text{v/cm}$. Note that the breakdown field strength for silicon is about $3\times10^5\ \text{v/cm}$. Therefore, a nearly unitary ratio between the magnitudes of the high order harmonics and the fundamental mode is a clear indication of semiconductor breakdown. Mathematically, it implies that the solution can no longer be expressed by a series of harmonics because the series (2.7b) divergences and thus is invalid.

For an excitation with $A^{(1)}=10^3\ \text{v/cm}$, the high order harmonics are very small fractions of the fundamental mode in magnitude, which are about or below 0.1% of the fundamental model. In this case, the MIS waveguide structure can be approximated as a linear circuit element. However, for an excitation with $A^{(1)}=10^5\ \text{v/cm}$, the second harmonic is now about one tenth of the fundamental mode in magnitude, which can no longer be neglected. In the later case, the MIS waveguide structure should be treated as a nonlinear circuit element. Given that the insulator thickness is $0.05\,\mu\text{m}$, the equivalent ac voltage to $A^{(1)} = 10^5 \text{ v/cm}$ is approximately 0.5v. Roughly speaking, most of the voltage drop is applied across the insulator layer and thus the magnitude of electric field is linearly proportional to the insulator thickness for a given voltage. A thicker insulator layer is able to reduce the electric field in the semiconductor substrate and thus suffers less severe nonlinearity. For instance, if the insulator thickness is increased to be $0.5\,\mu\text{m}$ the second harmonic is then only about one percent of the fundamental mode in magnitude although the ac voltage is still 0.5v.

## 6.2: CIRCUIT MODEL EXTARCTION

In this section, circuit parameter extraction results are presented for the equivalent circuit model of MIS interconnects. By comparison with measurements and results from other approaches, the device level frequency domain (DLFD) scheme for MIS interconnects is validated. Numerical results also demonstrate capabilities of the device level circuit modeling scheme and illustrate some interesting properties of the equivalent circuit model of MIS interconnects.

### 6.2.1: MODELING RESULTS VERSUS MEASUREMENTS

Consider an MIS interconnect structure consisting of a strip conductor, thin silicon-dioxide layer, the silicon substrate, and the ground plane. The geometrical parameters are as follows: $w = 650\,\mu\text{m}$, $h_d = 1\,\mu\text{m}$, and $h_c = 250\,\mu\text{m}$. The silicon is assumed to be *n*-type with a donor impurity concentration $N_d = 5\times10^{15}\,\text{cm}^{-3}$, which corresponds to a resistivity of $0.9\,\Omega\cdot\text{cm}$. The equivalent circuit model has been created for zero bias conditions using the scheme described in the preceding chapters. Once the circuit elements are computed, the characteristic impedance and propagation constant for this equivalent circuit can be readily obtained using standard transmission line theory [47]. Figure 6.17 through Figure 6.20 plot the characteristic impedance and propagation constant versus frequency, in comparison with the measured data from [6]. Generally good agreement is observed in comparing the computed results with measurements.

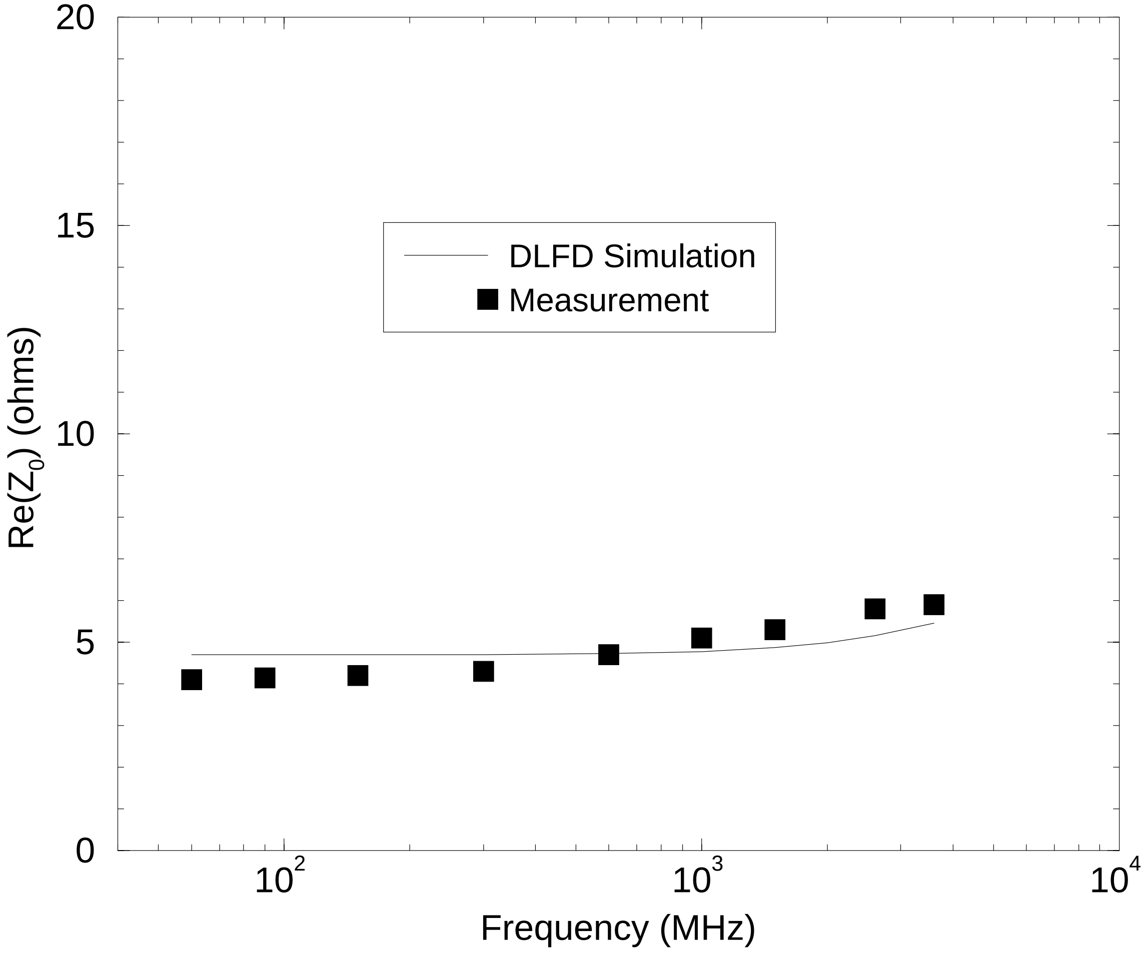

Figure 6.17: Comparison between theoretical prediction and measured data of real part of characteristic impedance.

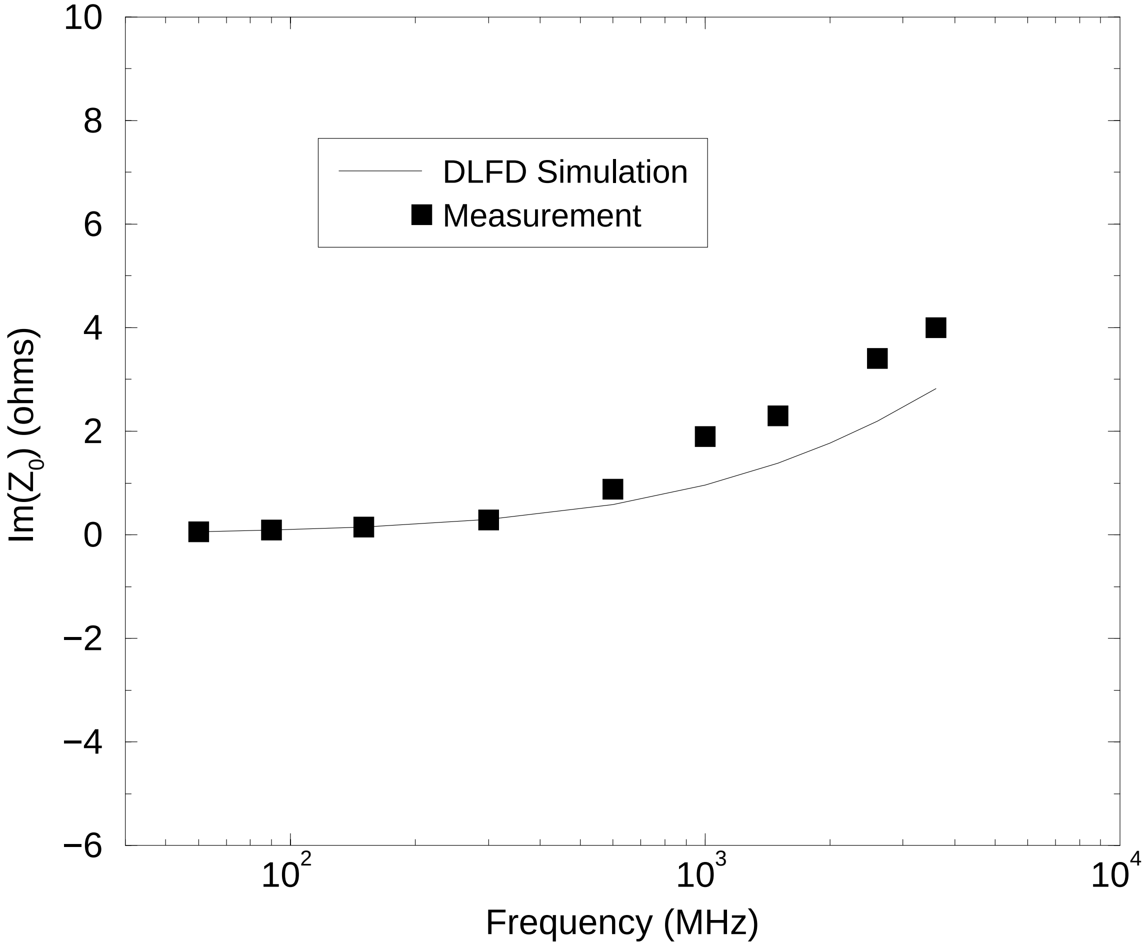

Figure 6.18: Comparison between theoretical prediction and measured data of imaginary part of characteristic impedance.

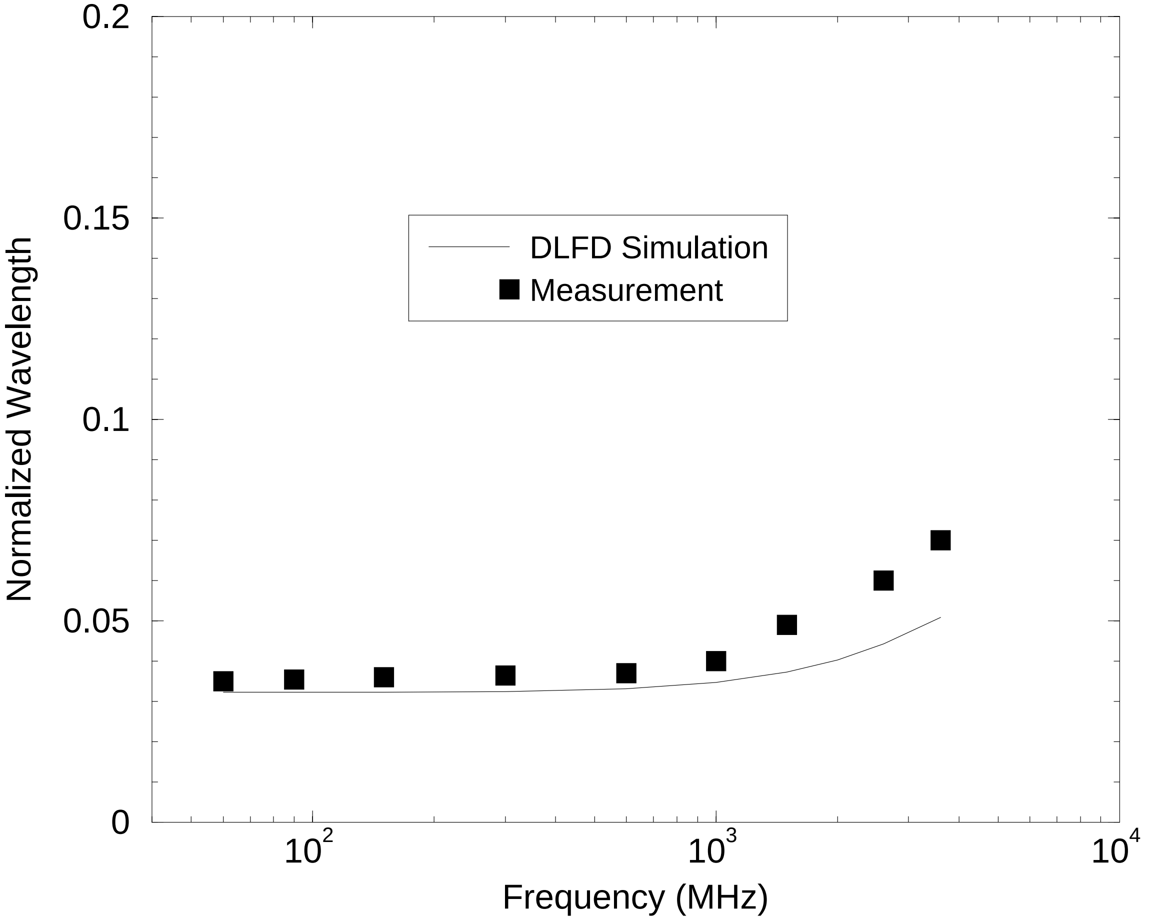

Figure 6.19: Comparison between theoretical prediction and measured data of phase constant.

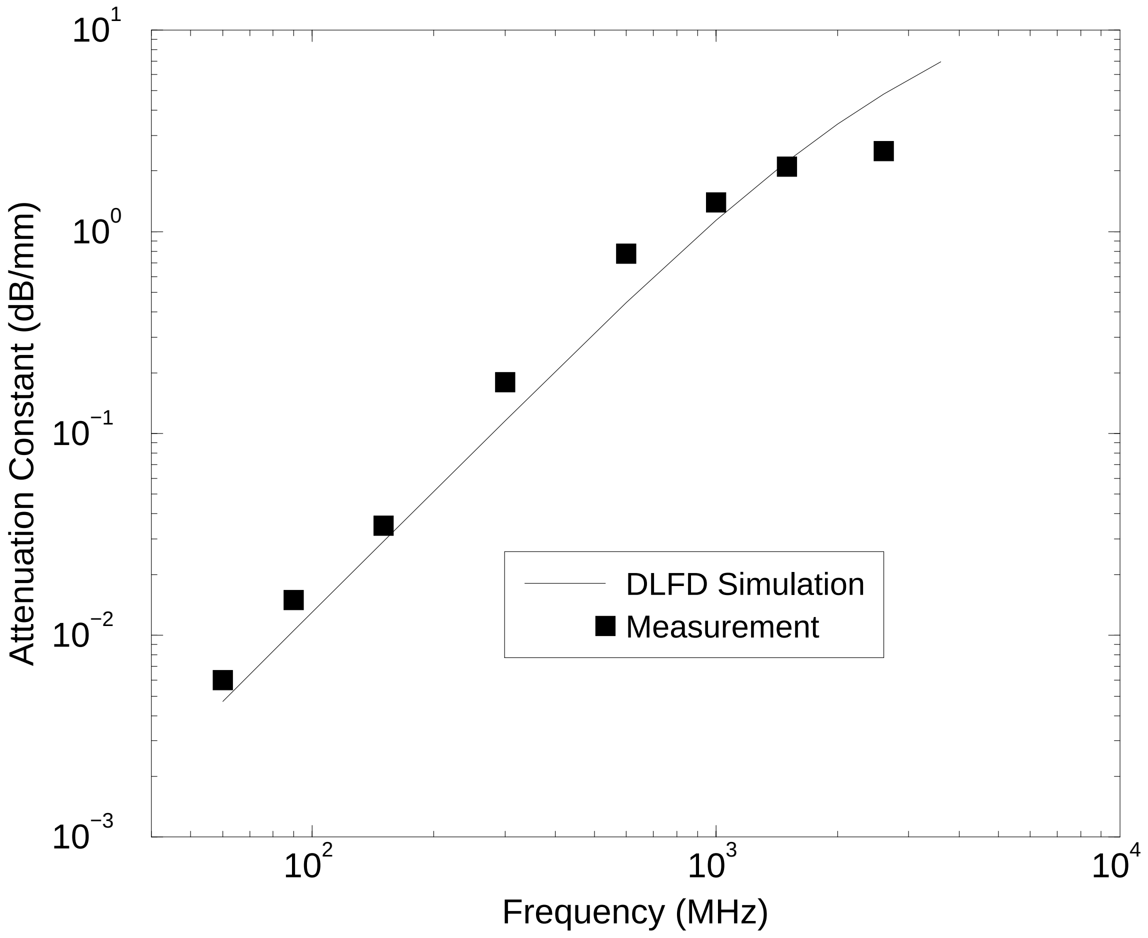

Figure 6.20: Comparison between theoretical prediction and measured data of attenuation constant.

### 6.2.2: EXTERNAL BIAS EFFECTS

Previous analyses of MIS interconnects have employed pure electromagnetic problems where the semiconductor substrate was treated as lossy medium. Hence neither external bias effects nor the inherent semiconductor nonlinearity are considered. In this work, the semiconductor substrate is described as solid state plasma, and the external bias effects on characteristics of MIS interconnects are directly included. In addition, the effects due to the semiconductor nonlinearity can be studied.

The external bias effects provide a theoretical foundation for designing electronic controllable devices. Figure 6.21 through Figure 6.24 show the characteristic impedance and propagation constant versus frequency for three external bias conditions: $V_0 = -0.2\,\text{volt}$, $V_0 = 0.0\,\text{volt}$, and $V_0 = 0.2\,\text{volt}$.

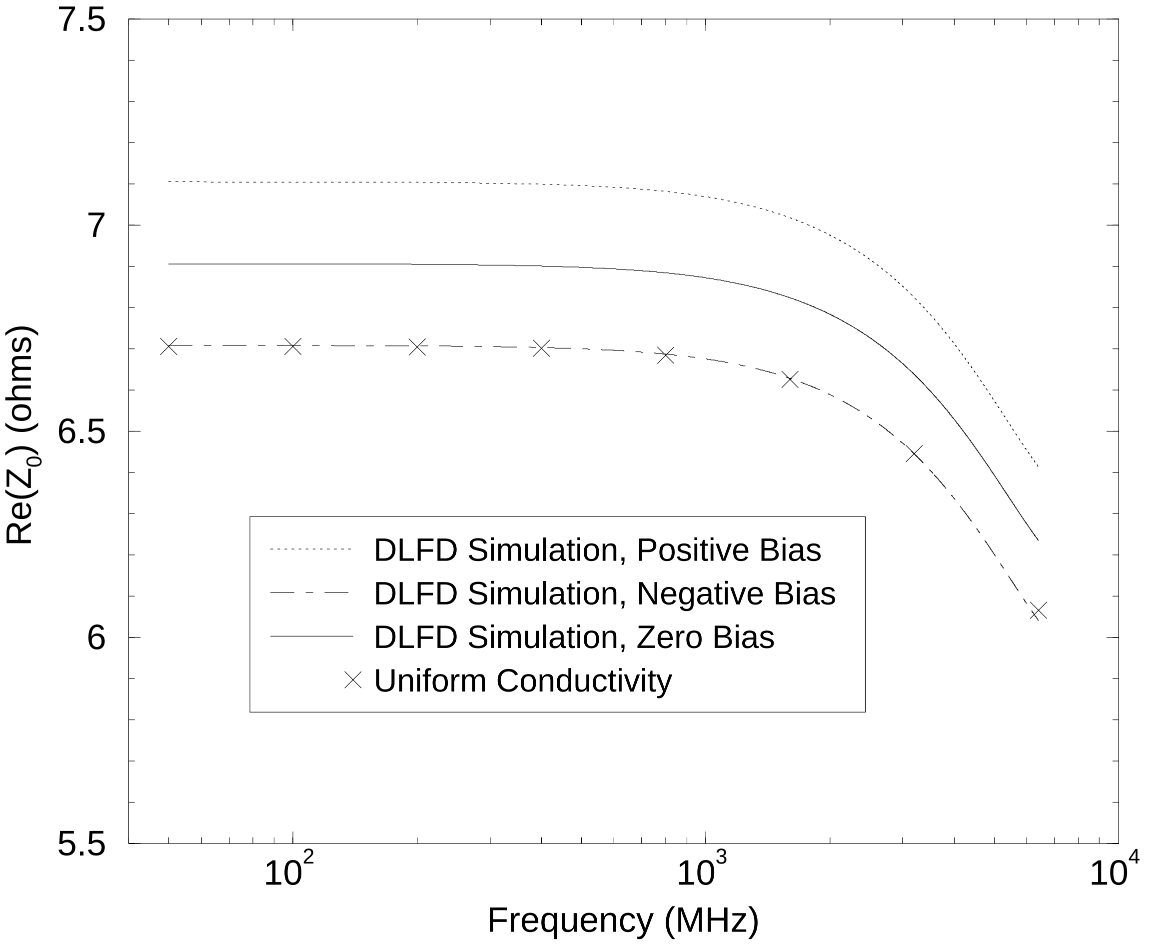

Figure 6.21: Real part of characteristic impedance versus frequency and external bias.

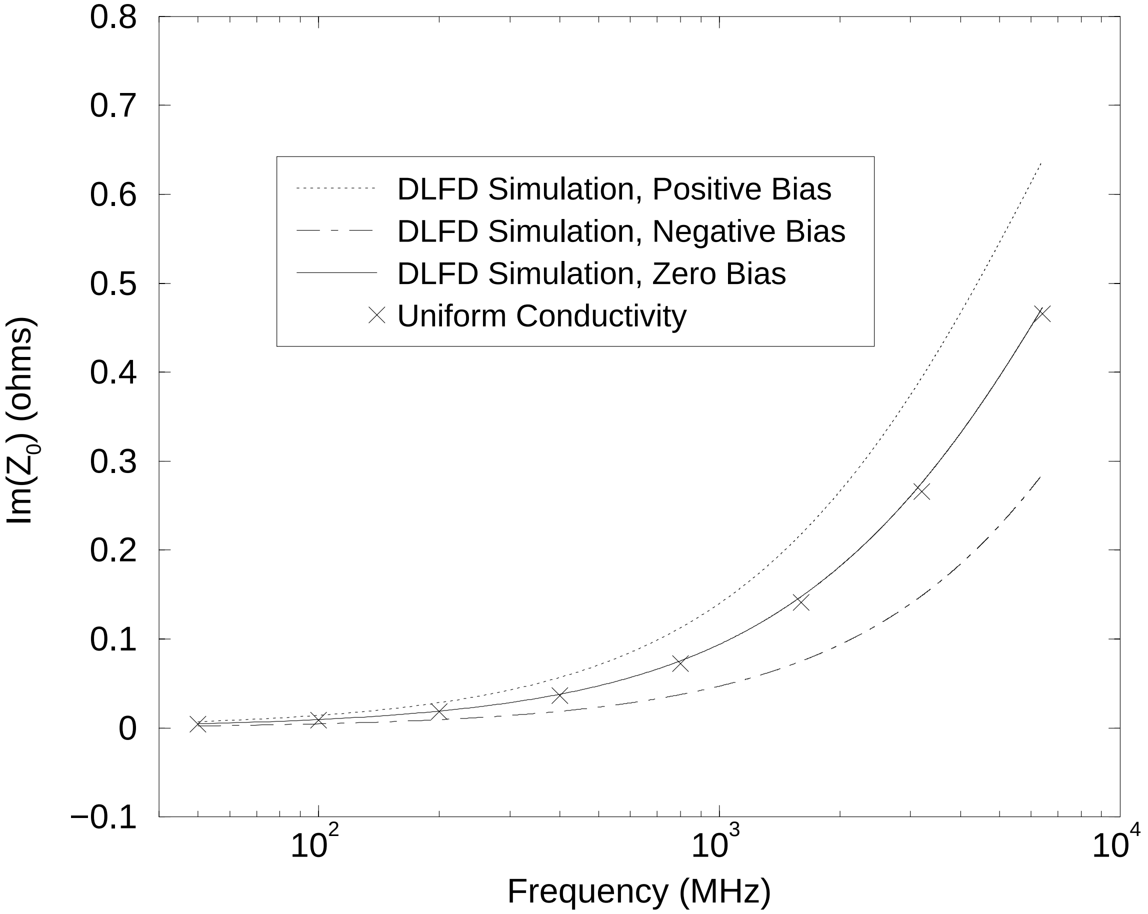

Figure 6.22: Imaginary part of characteristic impedance versus frequency and external bias.

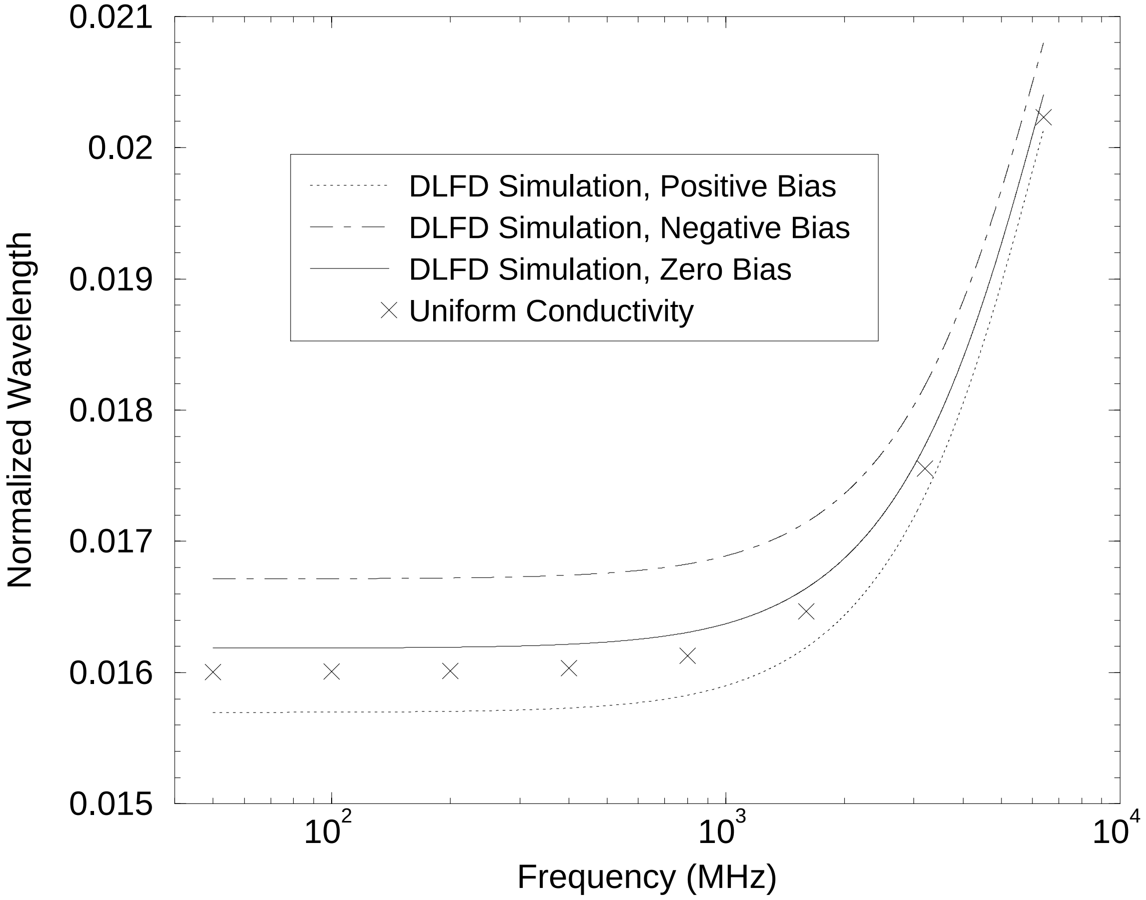

Figure 6.23: Phase constant versus frequency and external bias.

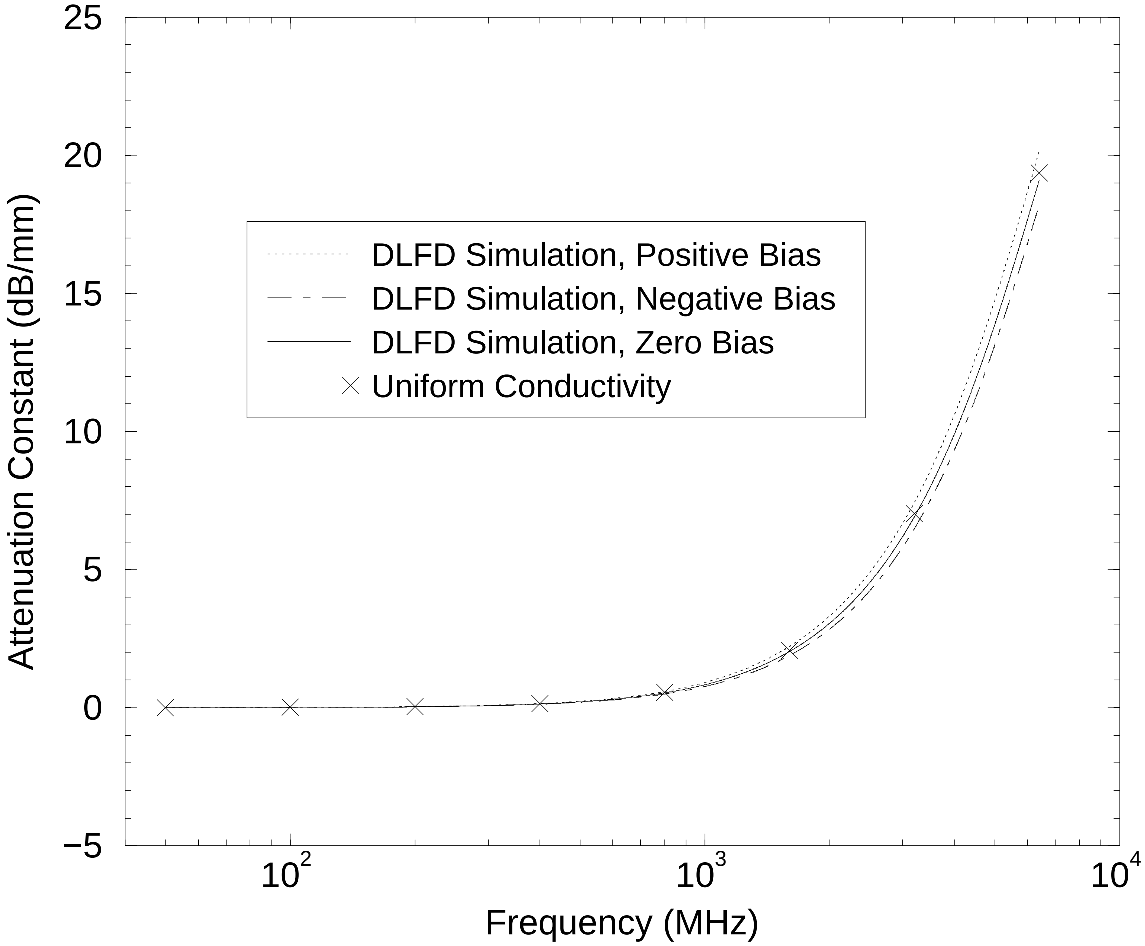

Figure 6.24: Attenuation constant versus frequency and external bias.

Calculated results using the uniform conductivity model [28, Appendix A] are also shown in Figure 6.21 through Figure 6.24. The geometrical parameters used in the calculations are as follows: $w = 90\,\mu\text{m}$, $h_d = 0.1\,\mu\text{m}$, and $h_c = 100\,\mu\text{m}$. The semiconductor substrate is assumed to be *n*-type silicon, now with donor impurity concentration $N_d = 10^{17}\,\text{cm}^{-3}$; the insulator is a thin silicon-dioxide layer. It can be observed that the uniform conductivity model generally gives results close to the solutions obtained by this device level scheme for the zero bias. Nevertheless, this scheme is able to provide a quantitative measure to the external bias effects on characteristics of MIS interconnects.

### 6.2.3: NONLINEARITY VERSUS IMPURITY CONCENTRATIONS

One of the salient merits of this device level modeling scheme is that the semiconductor nonlinearity can be studied, since the nonlinear behavior has been preserved in the motion equations of charged carriers.

Figure 6.25 through Figure 6.30 illustrate the extracted linear and nonlinear equivalent circuit elements for various impurity concentrations. In the calculations, all the parameters are the same as those used in subsection 6.2.1, except for the donor impurity concentration that varies over a range from $N_d = 5\times10^{15}\,\mathrm{cm}^{-3}$ to $N_d = 5\times10^{18}\,\mathrm{cm}^{-3}$. The operating frequency is assumed to be 1 GHz, and no external bias is applied to this MIS structure. The results obtained using the uniform conductivity model are also shown in the plots for linear circuit elements.

As shown by Figure 6.25 through Figure 6.30, for linear circuit elements, the uniform conductivity model gives results close to the numerical solutions from this device level scheme, although apparent differences for $C_s^{(1)}$ and $G_s^{(1)}$ are observed between the two sets of solutions when the semiconductor substrate is heavily doped.

Note that larger $\left|L_s^{(m)}\right|$ and $\left|R_s^{(m)}\right|$ or smaller $\left|C_s^{(m)}\right|$ and $\left|G_s^{(m)}\right|$ imply more significant contributions from the *m*-th harmonic ($m > 1$). Figure 6.25 through Figure 6.30 illustrate a case where the nonlinearity becomes less severe when the doping level in the semiconductor substrate increases. More heavily doped semiconductor substrates exhibit greater screening effect, which dramatically reduces the electromagnetic field penetration deep into the semiconductor, thus less wave energy participates in field-carrier interactions.

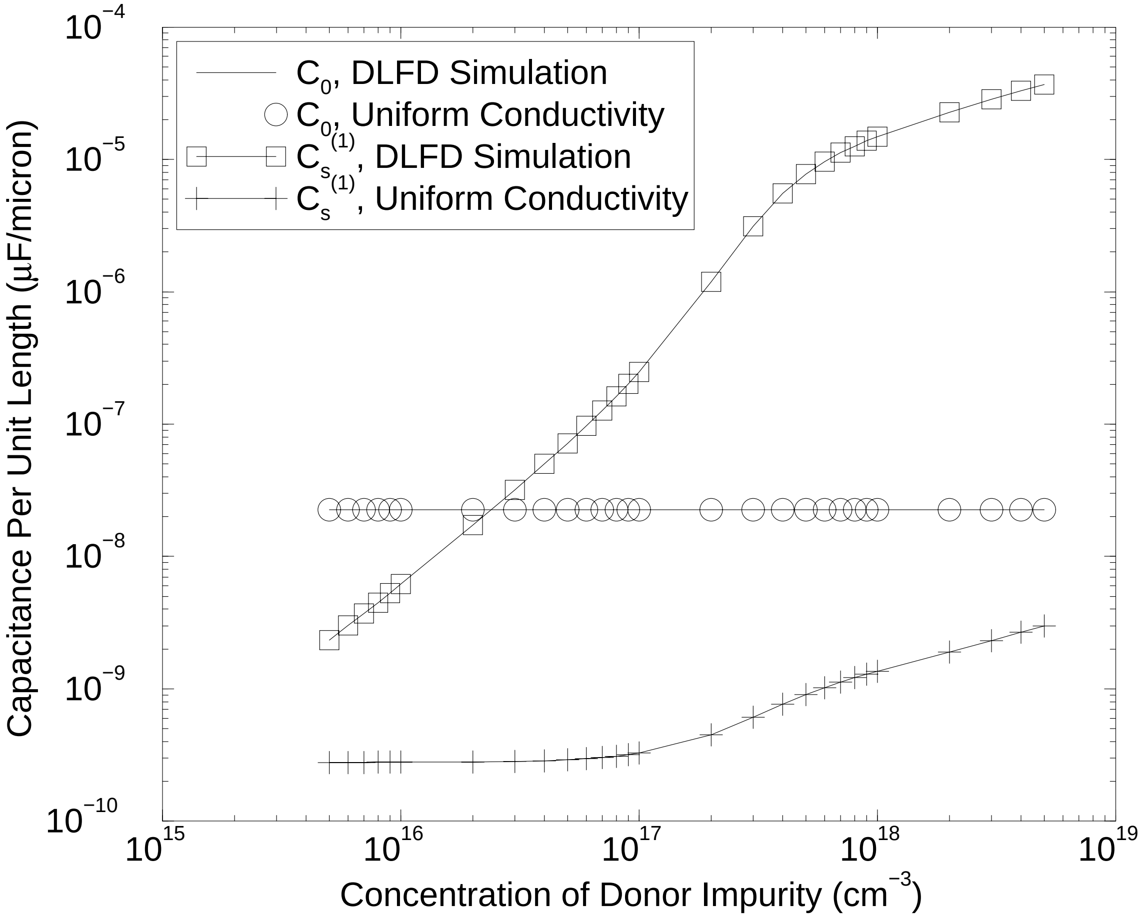

Figure 6.25: Equivalent circuit elements $C_0$ and $C_s^{(1)}$ versus doping rate.

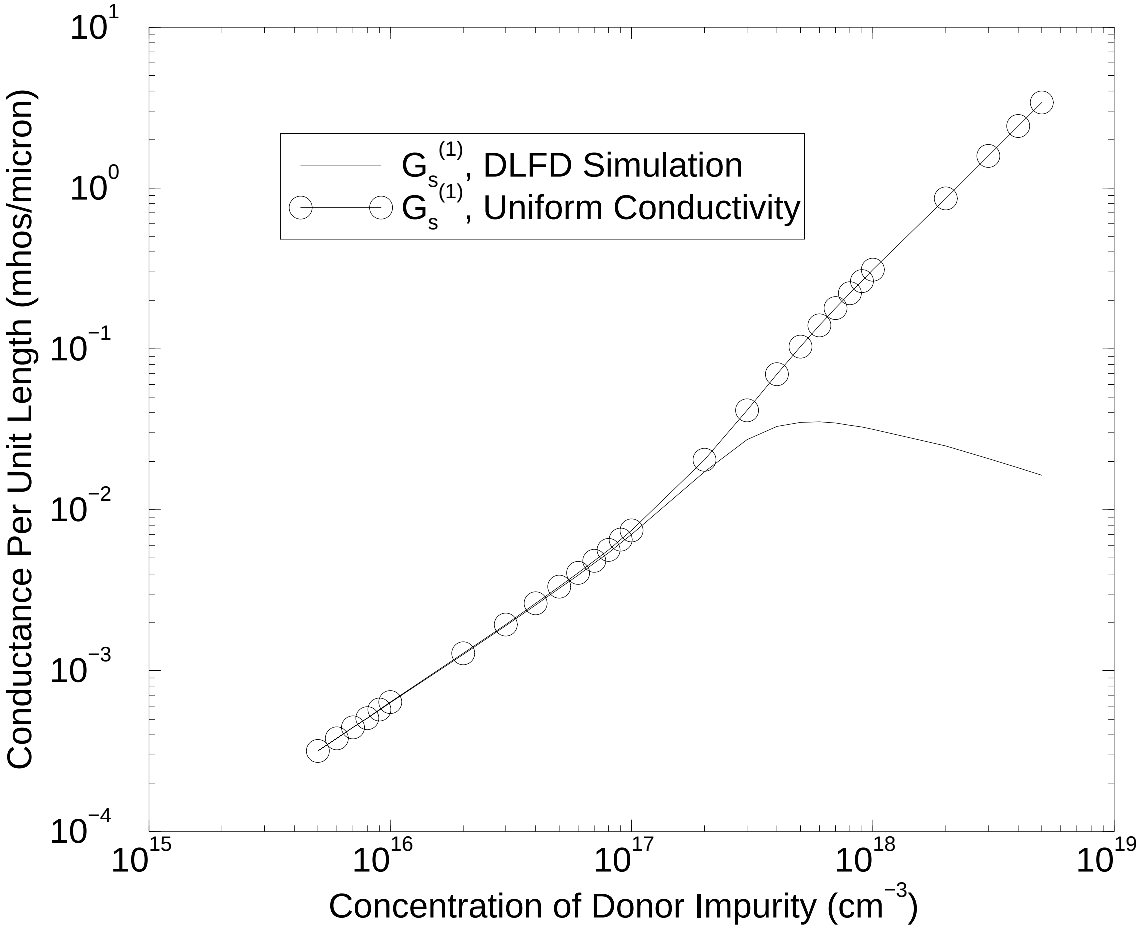

Figure 6.26: Equivalent circuit element $G_s^{(1)}$ versus doping rate.

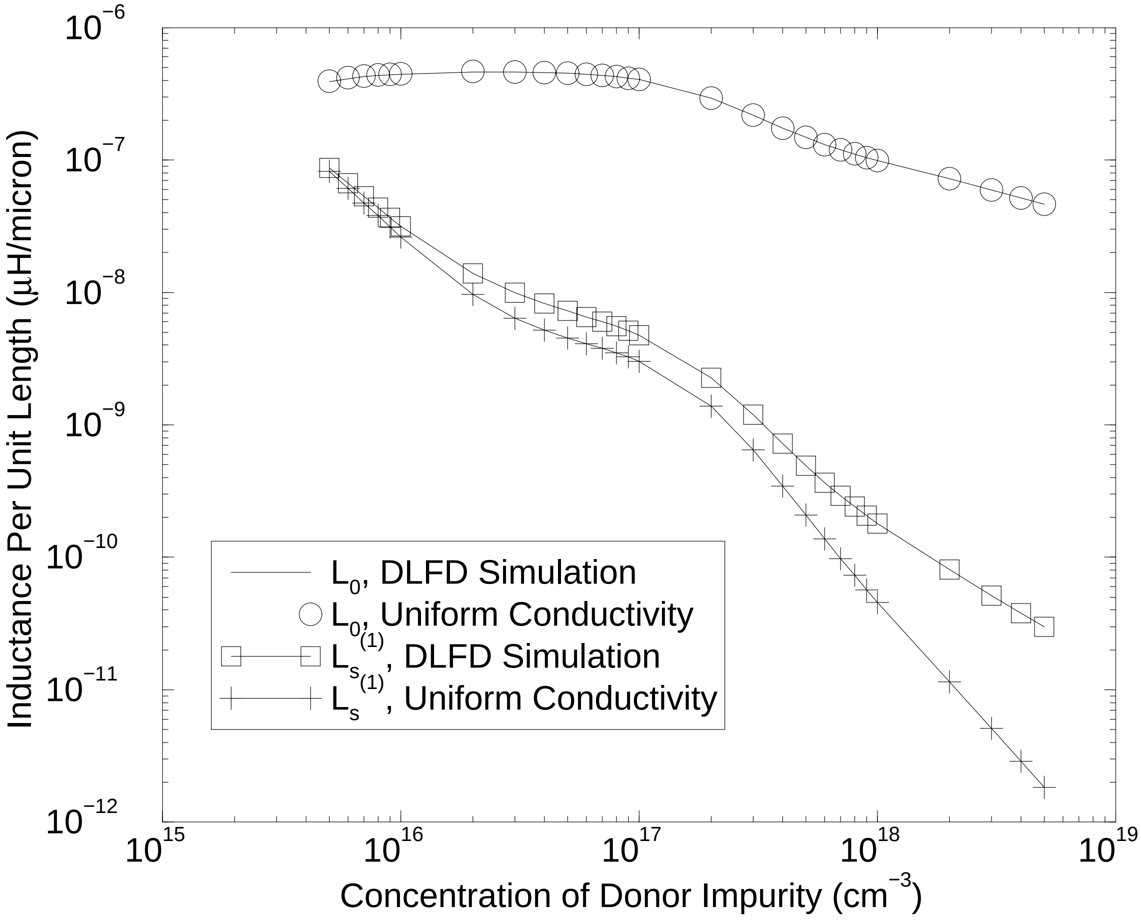

Figure 6.27: Equivalent circuit elements $L_0$ and $L_s^{(1)}$ versus doping rate.

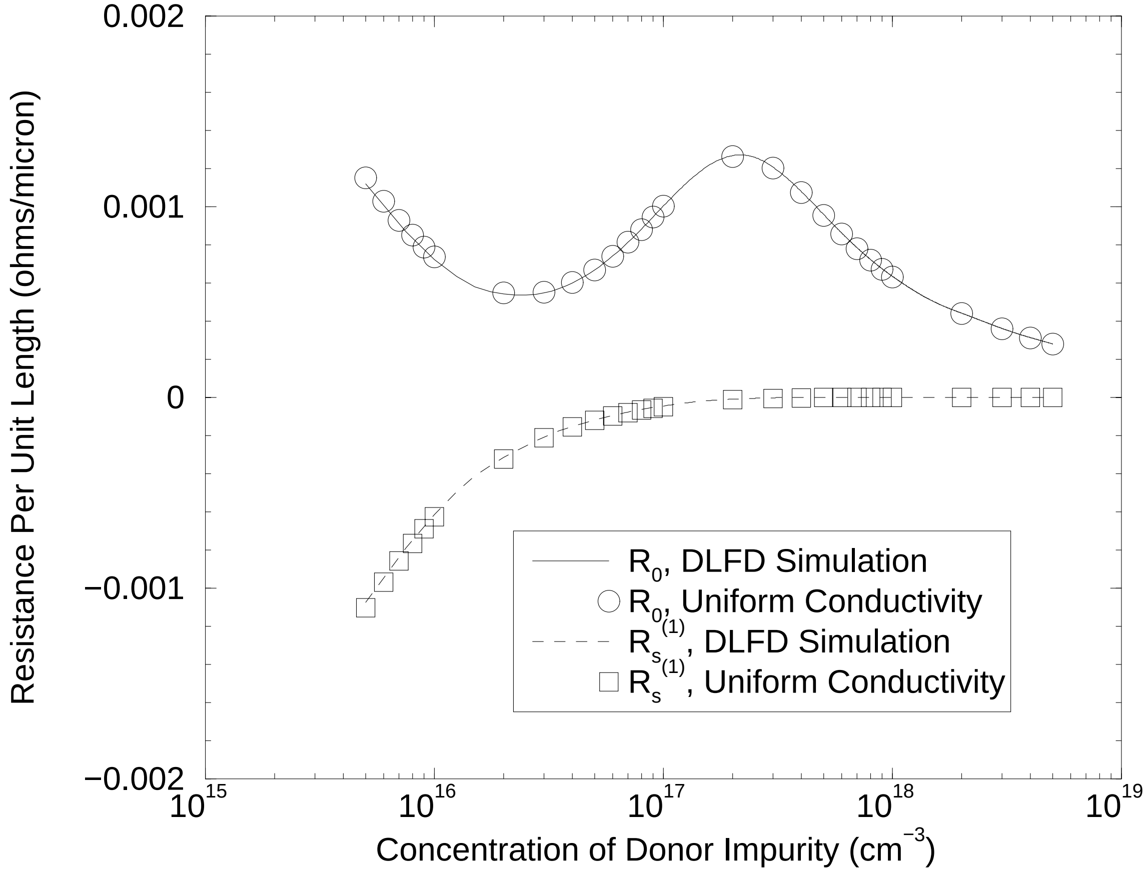

Figure 6.28: Equivalent circuit elements $R_0$ and $R_s^{(1)}$ versus doping rate.

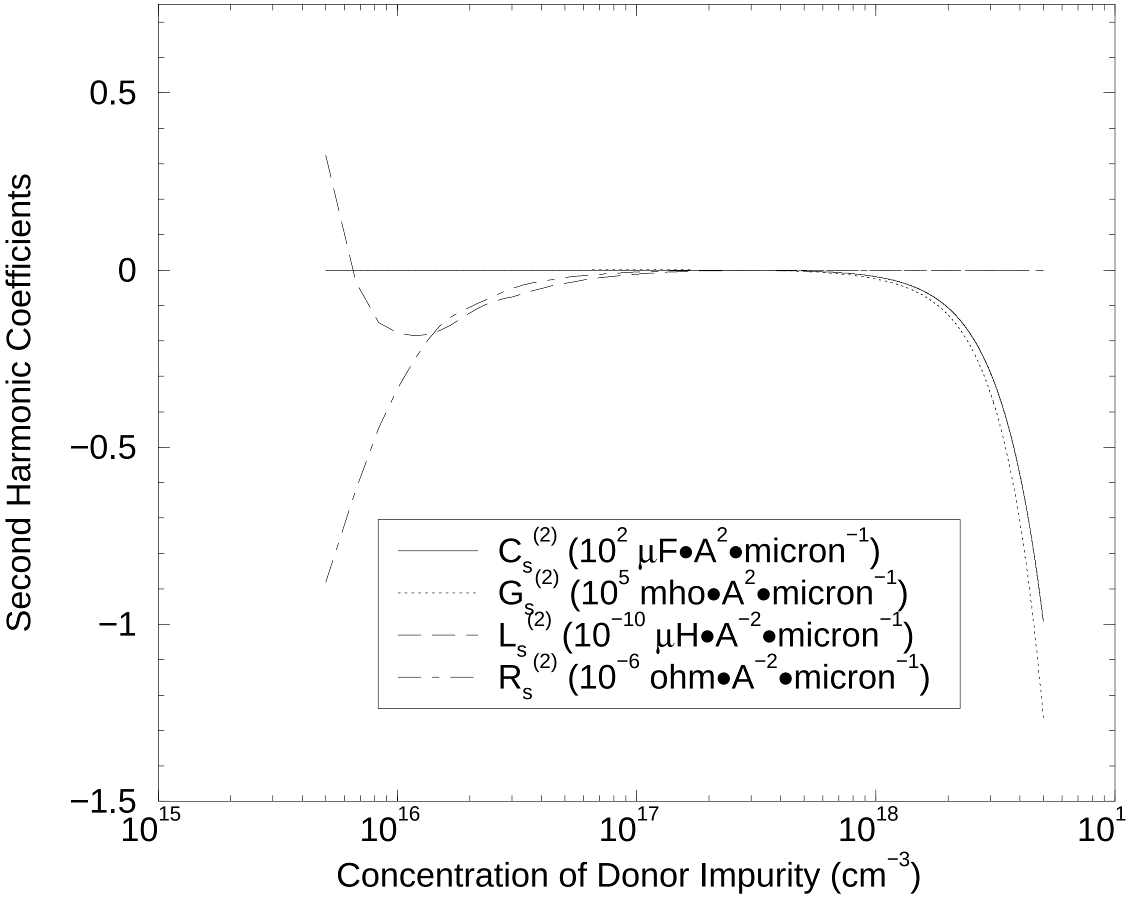

Figure 6.29: Equivalent circuit elements $C_s^{(2)}$, $G_s^{(2)}$, $L_s^{(2)}$ and $R_s^{(2)}$ versus doping rate.

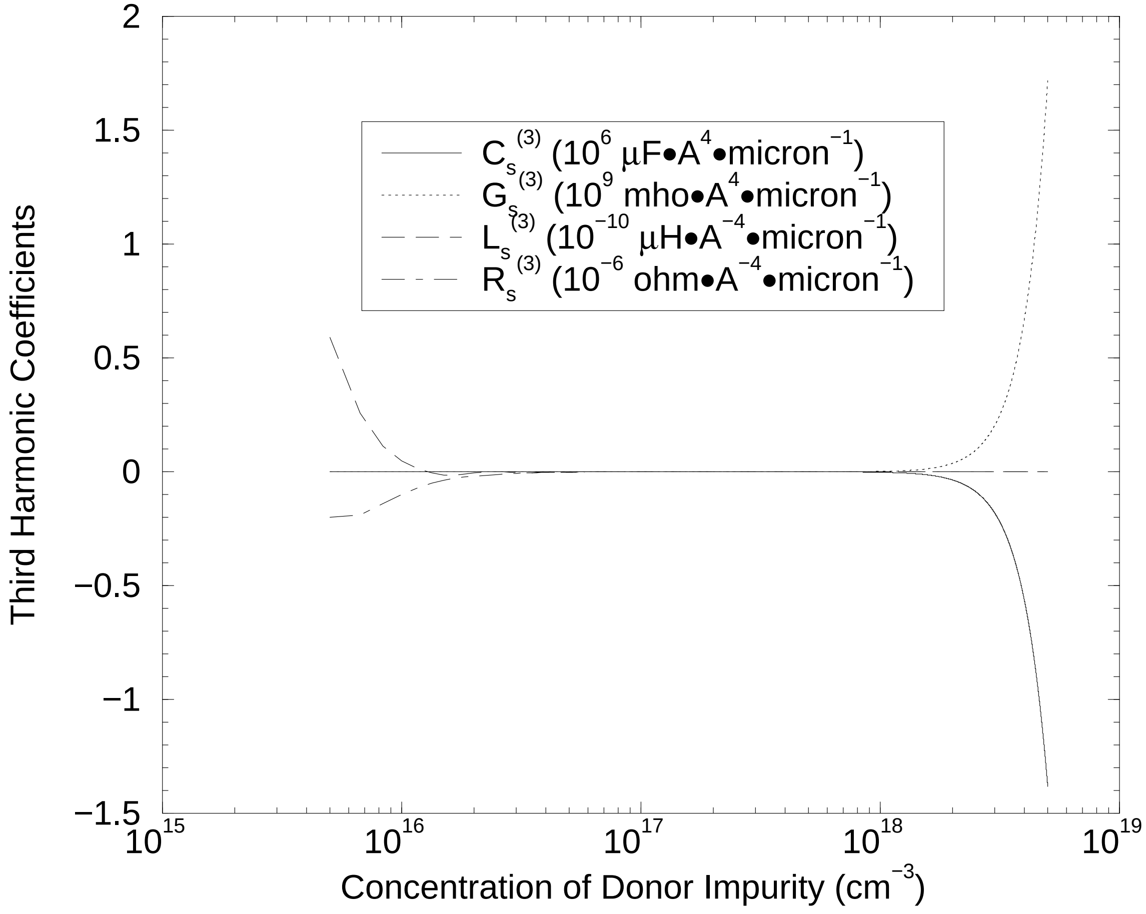

Figure 6.30: Equivalent circuit elements $C_s^{(3)}$, $G_s^{(3)}$, $L_s^{(3)}$ and $R_s^{(3)}$ versus doping rate.

### 6.2.4: NONLINEARITY VERSUS INSULATOR THICKNESS

Figure 6.31 through Figure 6.36 depict the linear and nonlinear equivalent circuit elements versus the insulator thickness. The insulator thickness is varied over a range from $h_d = 0.1\,\mu\text{m}$ to $h_d = 1\,\mu\text{m}$; the operating frequency is assumed to be 6.4 GHz with no external bias applied to the MIS structure. All other parameters are the same as those used for the example in subsection 6.2.2, except for the insulator thickness that varies over a range from $h_d = 0.1\,\mu\text{m}$ to $h_d = 1\,\mu\text{m}$. The operating frequency is assumed to be 6.4 GHz, and no external bias is applied to this MIS structure.

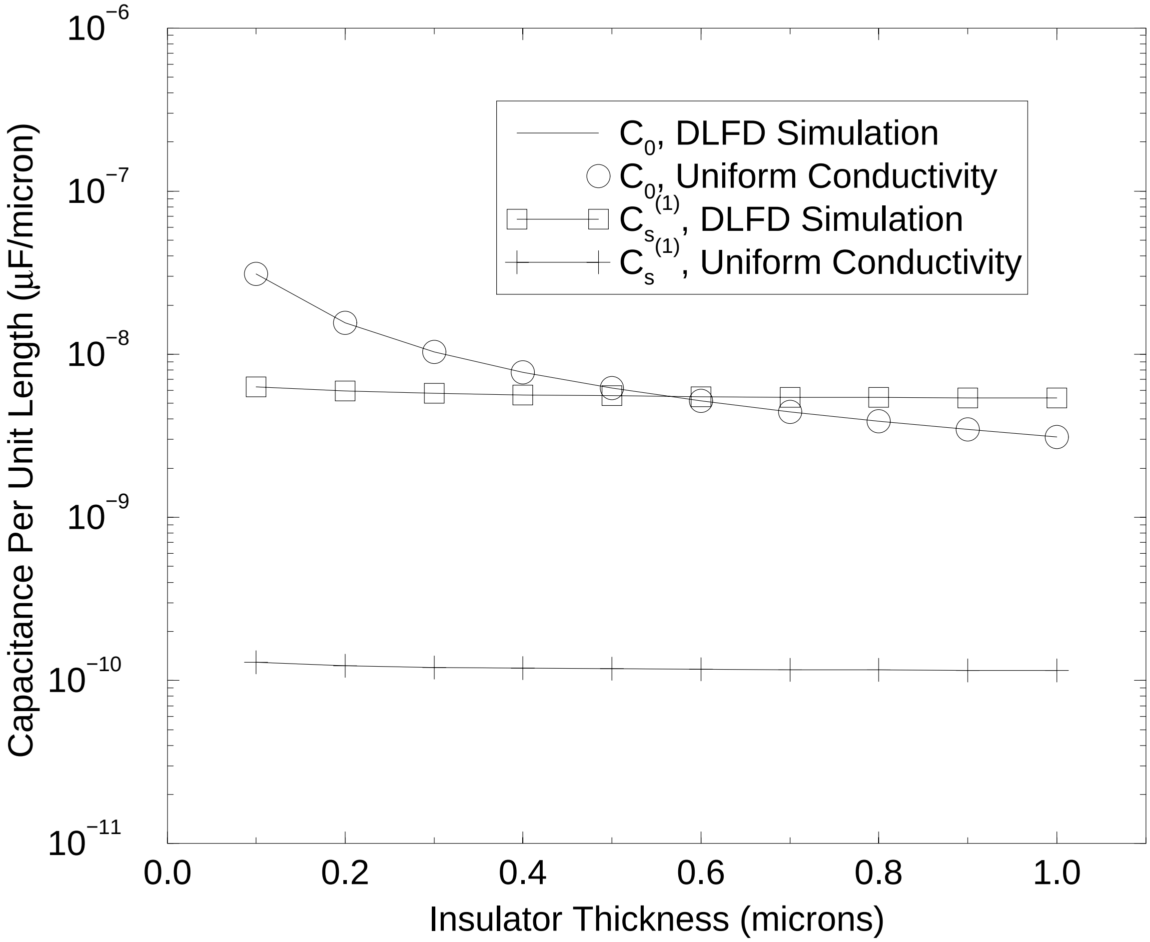

Figure 6.31: Equivalent circuit elements $C_0$ and $C_s^{(1)}$ versus insulator thickness.

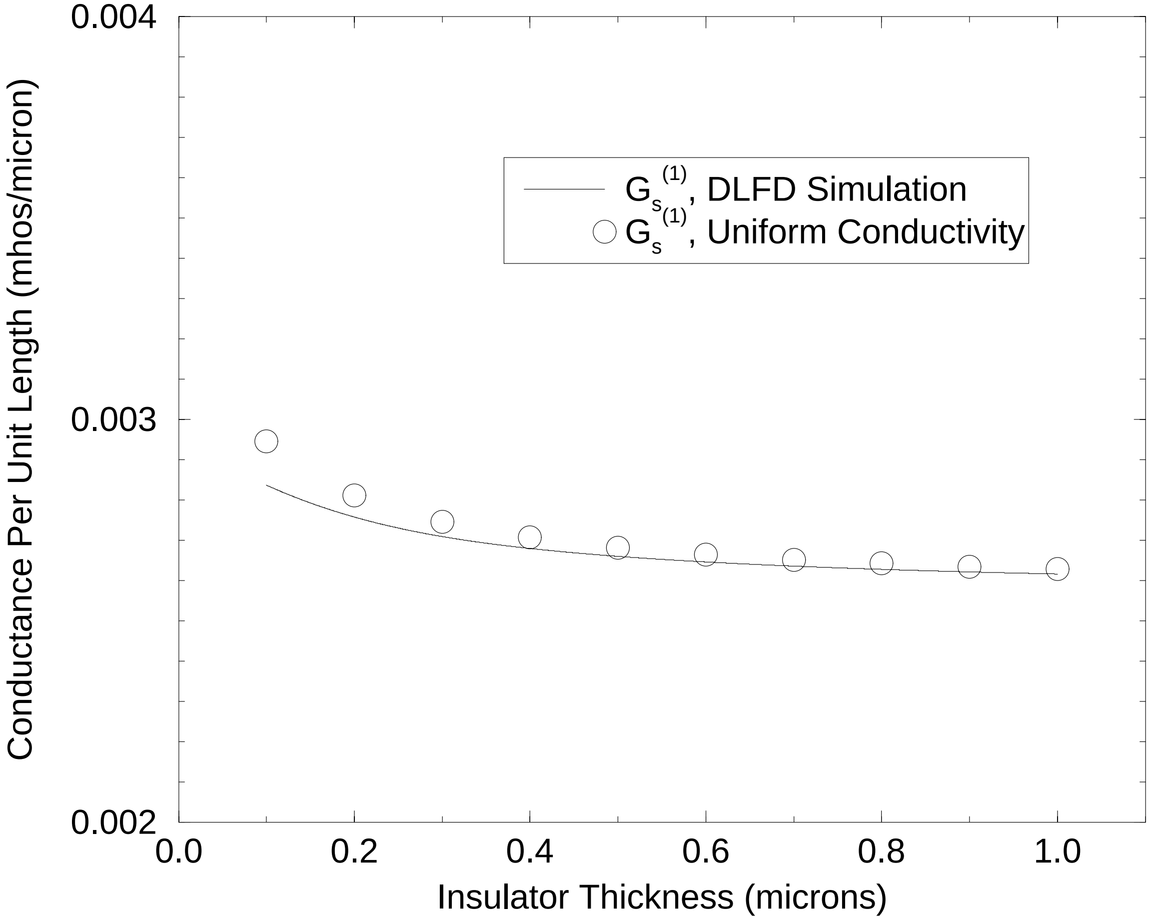

Figure 6.32: Equivalent circuit element $G_s^{(1)}$ versus insulator thickness.

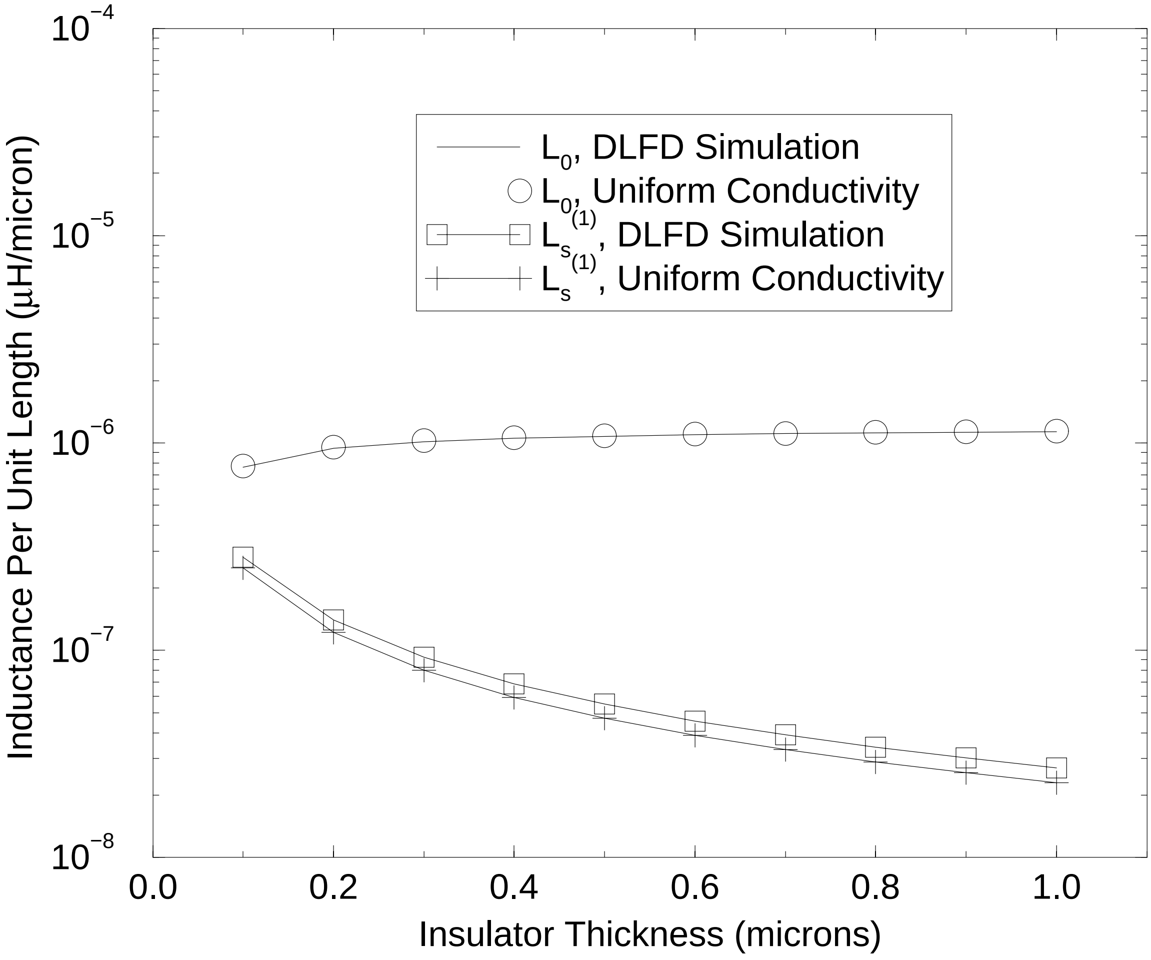

Figure 6.33: Equivalent circuit elements $L_0$ and $L_s^{(1)}$ versus insulator thickness.

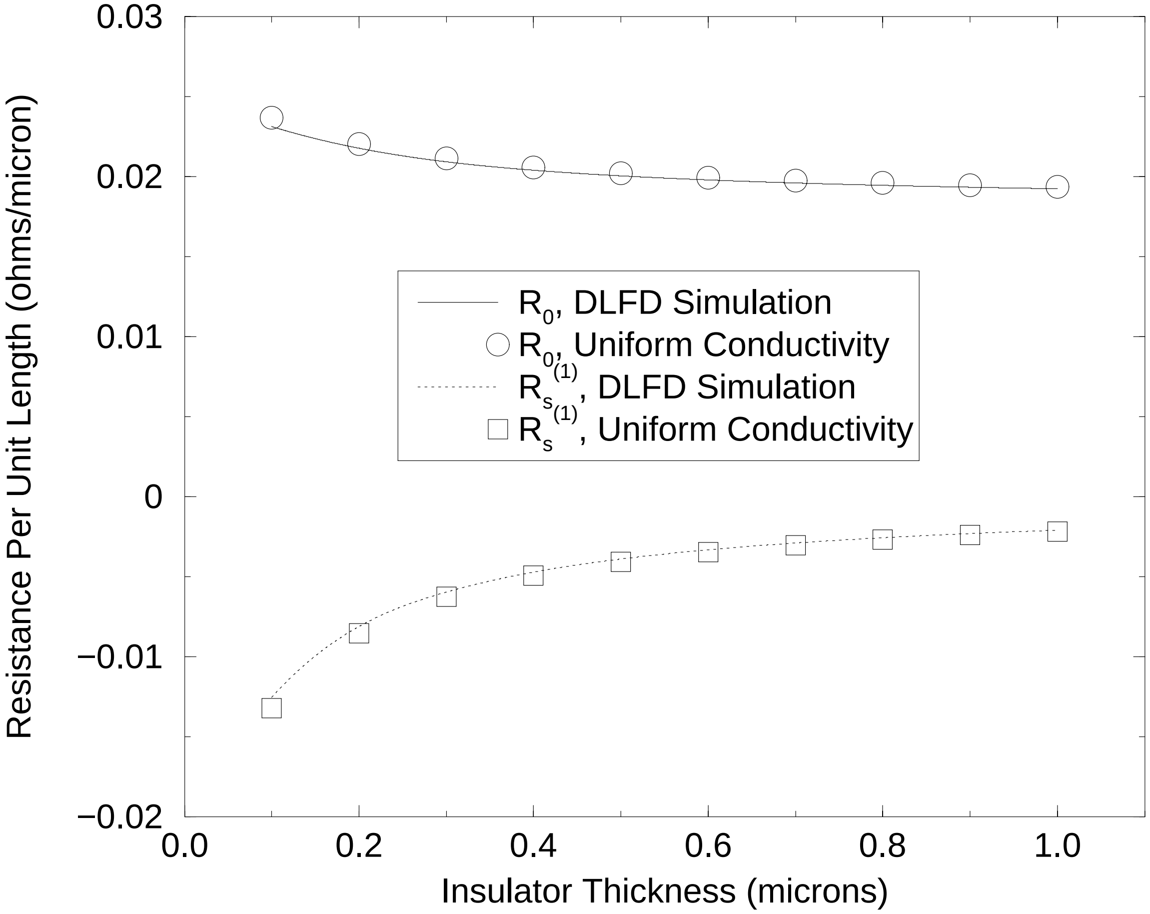

Figure 6.34: Equivalent circuit elements $R_0$ and $R_s^{(1)}$ versus insulator thickness.

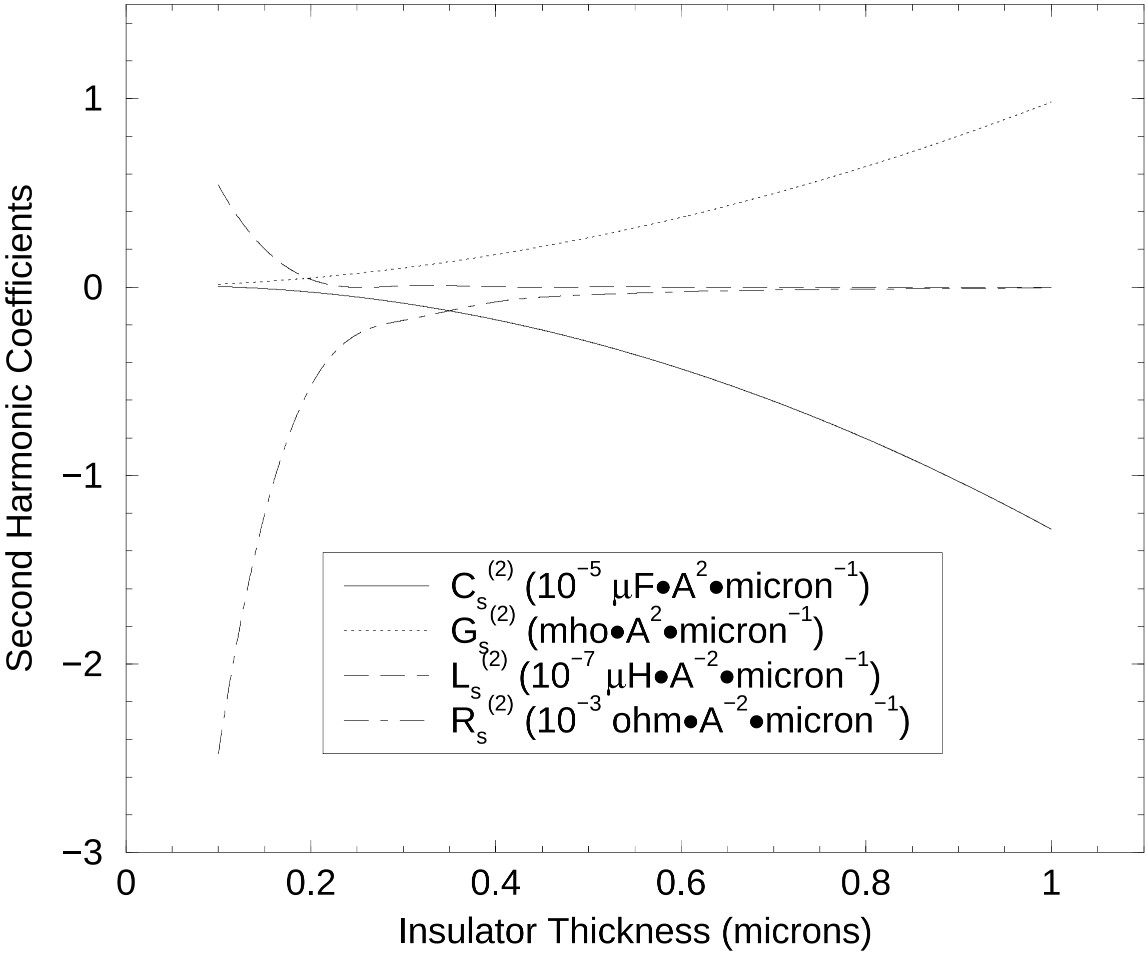

Figure 6.35: Equivalent circuit elements $C_s^{(2)}$, $G_s^{(2)}$, $L_s^{(2)}$ and $R_s^{(2)}$ versus insulator thickness.

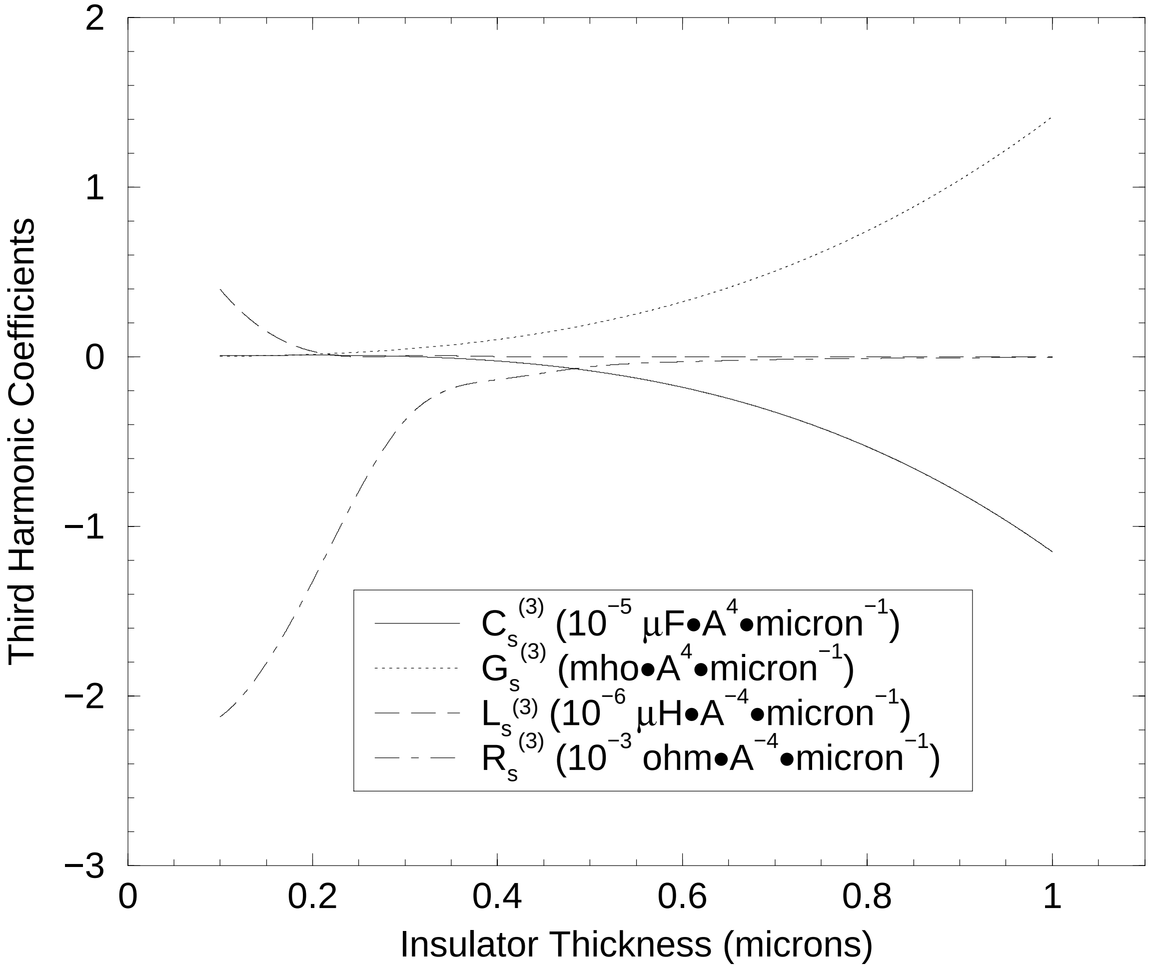

Figure 6.36: Equivalent circuit elements $C_s^{(3)}$, $G_s^{(3)}$, $L_s^{(3)}$ and $R_s^{(3)}$ versus insulator thickness.

For linear circuit elements, the results obtained using the uniform conductivity model are also shown in the plots for linear circuit elements. Note that the uniform conductivity model is unable to compute nonlinear circuit elements. It is well known that the insulator layer decouples the conductor strip from the semiconductor substrate and consumes the major portion of the voltage drop. As the insulator thickness increases, it is expected that the electromagnetic field decreases within the semiconductor substrate and thus the MIS structure exhibits less severe nonlinearity. As the insulator layer becomes thicker, smaller $\left|L_s^{(m)}\right|$ and $\left|R_s^{(m)}\right|$ as well as larger $\left|C_s^{(m)}\right|$ and $\left|G_s^{(m)}\right|$ are observed for $m = 2$ and $m = 3$ as expected in Figure 6.31 through Figure 6.36, which again indicates less nonlinear behavior.

## 6.3: SUMMARY

In this chapter, the device level frequency domain (DLFD) simulation and circuit model extraction schemes have been applied to practical design problems. Numerical results have been presented to validate the computer software implementations and demonstrate capabilities of the device level simulation scheme as well as the circuit model extraction. Good agreement was observed between the results computed by the device level approach and the measurements or previously published data.

The device level simulation is able to compute the propagation characteristics, electromagnetic field distributions, and carrier concentrations for the fundamental mode and high order harmonics. Numerical results demonstrated that the device level simulation provides the capabilities of studying field-carrier interactions, semiconductor substrate loss and nonlinearity, slow-wave effect, external bias effect, and screening effect of charged carriers.

The circuit model extraction for MIS interconnects is based on the device level simulation results. The energy-based approach was used for construction of the equivalent circuit model. The equivalent circuit model consists of an equivalent transmission line, which mimics the energy transport characteristics of the actual MIS interconnect. Numerical results from the circuit model extraction were presented to illustrate various effects of MIS interconnects including nonlinearity, voltage controllability, dependence on impurity doping, and impact of insulator thickness.

# CHAPTER 7: CONCLUSIONS

Prediction of electrical performance for on-chip interconnects is a crucial task in modern integrated circuit designs. Metal-insulator-semiconductor (MIS) interconnects, being one of the most elementary components in the modern integrated circuits, have been attracting a great deal of attention. Popular approaches for analysis of MIS interconnects are generally involved with electromagnetic problems, in which semiconductor substrates are simply treated as lossy materials and characterized in terms of conductivity or complex dielectric constant. Based on electromagnetic problems alone, these approaches may be unable to provide sufficient insight to various effects of MIS interconnects caused by particle-field interactions. In order to gain detailed knowledge on electrical performance of MIS interconnects, one needs to investigate MIS interconnects in a microscopic level, namely, to treat semiconductor substrates as solid state plasmas.

The nonlinear nature of semiconductor substrates has been generally ignored in most previous work. The question when to include the semiconductor nonlinearity, however, has not been answered quantitatively. In order to address the nonlinearity, the device level approach, which includes the nonlinear characteristics in the motion equations of charged carriers, can be utilized to facilitate the analysis of MIS interconnects.

The contour integral based approach, which has been widely employed to construct equivalent circuit models for interconnects, may be not applicable to MIS interconnects due to the presence of longitudinal electric field in TM waves. The energy-based approach can be employed to establish equivalent circuit models for MIS interconnects. The energy-based approach builds an equivalent circuit model based on the power equivalence between the circuit model and the original MIS interconnect.

## 7.1: SUMMARY

In this work, coupled electromagnetic and device level investigations of MIS interconnects have been presented. A device level simulation based on Maxwell's equations and the motion equations of charged carriers was first presented to study the propagation characteristics of MIS interconnects. Based on the device level simulation, a rigorous circuit model extraction was then proposed for MIS interconnects.

The basic theory for analysis of MIS interconnects was established upon electromagnetic theory and semiconductor physics. In order to investigate field-carrier interactions between electromagnetic fields and charged carriers, semiconductor substrates have been described as solid state plasmas. Maxwell's equations govern the electromagnetic fields, whereas the concentrations of charged carriers are determined by their motion equations. By combining Maxwell's equations and the motion equations of charged carriers, the device level formulae for analyzing MIS interconnects were developed.

The nonlinearity in the motion equations gives rise to signal distortions, which are best studied using harmonics in the frequency domain. By using Fourier analysis, the frequency domain formulae for various harmonics were derived from the time domain formulae. The frequency domain formulae reveal a nice property that any given harmonic depends on the lower order harmonics only. Hence, the frequency domain formulae can be recursively solved in a manner from a lower order harmonic to a higher order harmonic, starting from the static solution.

The device level frequency domain (DLFD) simulation was developed for investigating the wave propagation characteristics along MIS interconnects by virtue of the general frequency domain formulae. For simplicity, an MIS interconnect was modeled as a parallel-plate waveguide structure for the device level simulation. The boundary conditions were carefully studied and properly devised.

The finite element method was utilized for discretization of the basic equations. The weak formulation was developed for each harmonic. By virtue of Galerkin's method and the finite element discretization, a set of algebraic equations was obtained for each harmonic. For the fundamental mode, a set of nonlinear equations was derived. Multi-dimensional Newton's method was applied to solve the set of nonlinear equations simultaneously, which reduced the number of iterations considerably. For a high order harmonic, a set of linear equations was solved. Sparse matrix techniques were used for improving computational speed and saving memory space.

The nonlinearity in the motion equations of charged carriers was preserved and included in the formulae. Thus, this approach is suitable for both small-signal and large-signal analyses. The boundary layer nature of the problem under study was manifested theoretically and treated in a numerically consistent manner through adaptive finite element discretization. This device level simulation can provide quantitative predictions to propagation and attenuation constants as well as detailed field and carrier distributions of the fundamental mode and high order harmonics. This proposed device level simulation scheme is capable of studying detailed field-carrier interaction mechanisms, semiconductor substrate loss and nonlinearity, slow-wave effect, external bias effect, and screening effect of charged carriers. It was shown that higher order harmonics due to semiconductor nonlinearity are confined within the semiconductor and do not penetrate into the insulator in MIS waveguide structures.

Based on the device level simulation, a rigorous modeling scheme for metal-insulator-semiconductor (MIS) interconnects was introduced. The energy-based approach was used for construction of the equivalent circuit model from the device level simulation results. The equivalent circuit model consists of an equivalent transmission line, which mimics the energy transport characteristics of the actual MIS interconnect.

The equivalent circuit model, which retains information about the semiconductor substrate effects obtained from the device level simulation, provides a generalized nonlinear and electronic tunable circuit model suitable for both small-signal and large-signal analyses. The equivalent circuit model also provides a unified set of formulae for the entire frequency-conductivity domain and is valid for a wide range of frequency and impurity doping level.

The device level frequency domain (DLFD) simulation of wave propagation along MIS interconnects was implemented within the PROPHET framework. In order to perform the device level simulation for wave propagation, electromagnetic analysis capability was added into the PROPHET framework. More than two dozens of physical operators were developed in the PROPHET framework for the device level simulation. The derivative nodal operator as well as scalar field concept were introduced the PROPHET framework to support the newly created physical operators. The extraction of an equivalent circuit model for MIS interconnects was implemented as a standalone program using the C++ language.

The device level frequency domain (DLFD) simulation and circuit model extraction schemes were applied to practical design problems. Numerical results were presented to validate the computer software implementations and demonstrate capabilities of the device level simulation scheme as well as the circuit model extraction. Good agreement was observed between the results computed by the device level approach and the measurements or previously published data.

Numerical results demonstrated that the device level simulation provides the capabilities of studying field-carrier interactions, semiconductor substrate loss and nonlinearity, slow-wave effect, external bias effect, and screening effect of charged carriers. Moreover, numerical results were presented to illustrate interesting properties of the nonlinear and electronic tunable circuit model of MIS interconnects, including nonlinearity, external bias effects, dependence on impurity doping, and impact of insulator thickness.

## 7.2: FUTURE WORK

The metal loss and fringing effects of conducting lines have been extensively studied within the (pure) electromagnetic analysis framework. The current work has been mainly focusing on the device level investigations of semiconductor effects. Nevertheless, these conductor effects can be incorporated into the device level simulation as well.

The current work can be extended to include the metal loss of imperfect conductors such as signal lines. The metal loss can be added into the device level simulation by introducing finite conductivity into the conductors. The effects of finite conductivity of conductors can be modeled by an impedance boundary condition [56, 89, 90].

In order to include the fringing effects, the conducting signal line must be treated as a conductor with finite thickness and finite width during the device level simulation. The electromagnetic fields can no longer be confined between the signal line and the ground plane. Moreover, the fringing fields destroy the uniformity along the $y$ direction. Hence, both the $x$ and $y$ dimensions must be discretized numerically. In addition, absorbing boundary conditions will be needed for the open region. Alternatively, instead of using differential equations, an integral equation formulation for electromagnetic fields may be utilized to confine the problem in a smaller solution region [90].

The current work can be used to design and analyze new integrated devices that make use of electronic tunability of MIS structures. One good example of such devices could be an electronic tunable clock distribution network, which can intelligently adjust the delays among different clock distribution branches. The delay adjustment over a clock net can be realized using the slow-wave effect and applied external bias. Electronic controllability of MIS structures provides a great possibility for designing electronic self-adjustable devices. The current work can be served as a simulation platform for exploring new integrated devices.

The slow-wave effect allows designing smaller components for RF, analog, and microwave applications. The typical slow-wave components include delay lines, phase shifters, band-pass filters, etc. In addition, these slow-wave components can be made to be electronic tunable. The current work can be employed to analyze and verify these electronic tunable slow-wave component designs.

The substrate noise due to semiconductor nonlinearity can be rigorously investigated using the current work. The current work can be applied to study signal integrity related to nonlinear substrate noise, which could not be properly addressed by other existing approaches. On the other hand, semiconductor nonlinearity can be utilized to sharpen signal pulses in practical applications. The current work provides an accurate nonlinear model for MIS structures, and thus can be applied to study nonlinear sharpening of signal pulses. Nevertheless, efficient utilization and seamless integration of such a nonlinear model within a circuit simulation environment could be a challenging task.

Measurements from the most updated integrated circuit technology are always valuable for validating the assumptions used in the simulation work. Some assumptions applicable to today’s integrated circuit technology may need to be re-examined and enhanced along the advancement and evolvement of integrated circuit technology.

# APPENDIX A: ANALYTICAL MODELING OF METAL-INSULATOR-SEMICONDUCTOR INTERCONNECTS USING THE UNIFORM CONDUCTIVITY MODEL

In this Appendix, an analytical model of MIS interconnects is presented using the energy-based approach [44]. The energy-based approach abandons the approach based on intuitively chosen contour integrals. Rather, it builds the equivalent circuit model based on the power equivalence between the circuit model and the original MIS waveguide. With respect to the frequency and the semiconductor conductivity, the fundamental TM wave mode was classified into three modes by properly dividing the frequency-conductivity domain into three regions: the slow-wave mode, the dielectric quasi-TEM mode, and the skin-effect mode, which lead to three different circuit models [6]. This new model provides a unified set of formulae for the entire frequency-conductivity domain. This new model has solid physical foundation and is valid for a wide range of frequency and impurity doping level.

## A.1: SOLUTION OF ELECTROMAGNETIC FIELDS

An MIS interconnect structure is shown in Figure 3.1. Herein, the signal line is assumed to be an ideal conductor and wide enough, so that a parallel-plate waveguide approach is applicable. The uniform conductivity model is utilized to account for impact of the semiconductor substrate.

In a parallel-plate MIS waveguide, all the physical quantities are uniformly distributed along the *y* direction. The fundamental mode in the MIS waveguide is a TM mode. For guided waves propagating along the *z* direction, one has

$$\mathbf{E}(\mathbf{r},t)=\mathbf{E}(x)\ e^{-\gamma z+j\omega t} \tag{A.1a}$$

$$\mathbf{H}(\mathbf{r},t)=\mathbf{H}(x)\ e^{-\gamma z+j\omega t} \tag{A.1b}$$

where $\gamma$ denotes the propagation constant and $\omega$ is the angular frequency. By solving Maxwell's equations under the boundary conditions on the signal line, the ground plane, and the interface between insulator and semiconductor in virtue of the transverse resonance method [46], the fundamental TM mode solution can be readily obtained as follows:

$$E_z(x)=\begin{cases}-\dfrac{Ak_1}{\gamma}\sin[k_1(x+h_d)] & -h_d\le x\le 0\\ -\dfrac{A\tilde{Q}k_2}{\gamma}\sin[k_2(x-h_c)] & 0\le x\le h_c\end{cases} \tag{A.2a}$$

$$E_x(x)=\begin{cases}A\cos[k_1(x+h_d)] & -h_d\le x\le 0\\ A\tilde{Q}\cos[k_2(x-h_c)] & 0\le x\le h_c\end{cases} \tag{A.2b}$$

$$H_y(x)=\begin{cases}\dfrac{j\omega\tilde{\varepsilon}_1A}{\gamma}\cos[k_1(x+h_d)] & -h_d\le x\le 0\\ \dfrac{j\omega\tilde{\varepsilon}_2A\tilde{Q}}{\gamma}\cos[k_2(x-h_c)] & 0\le x\le h_c\end{cases} \tag{A.2c}$$

$$E_x(x)=H_y(x)=H_z(x)=0 \tag{A.2d}$$

where $A$ is an arbitrary constant depending on the excitation magnitude, $\tilde{\varepsilon}_1=\varepsilon_1$, $\tilde{\varepsilon}_2=\varepsilon_2-j\sigma_2/\omega$, $k_i^2=\omega^2\mu_0\tilde{\varepsilon}_i+\gamma^2$, $\mu_0$ is the permeability of vacuum, $\varepsilon_1$ is the permittivity of insulator, $\varepsilon_2$ and $\sigma_2$ are, respectively, the permittivity and conductivity of semiconductor, and $\tilde{Q} = [\tilde{\varepsilon}_1 \cos(k_1 h_d)]/[\tilde{\varepsilon}_2 \cos(k_2 h_c)]$. Depending on impurity doping rate, the conductivity $\sigma_2$ can vary over a wide range. For instance, it ranges over more than four decades from 1 *S/m* to $10^5$ *S/m* in silicon substrates. The propagation constant $\gamma$ can be determined from the following equation:

$$\frac{k_1}{\tilde{\varepsilon}_1} \tan(k_1 h_d) = -\frac{k_2}{\tilde{\varepsilon}_2} \tan(k_2 h_c) \tag{A.3}$$

## A.2: ANALYTICAL CIRCUIT MODEL

A general form of a transmission line model consists of a series impedance *Z* per unit length and a shunt admittance *Y* per unit length, as shown in Figure 4.1. To build an equivalent transmission line model for an MIS interconnect, the following requirements are prescribed [44]:

- The propagation constant for the equivalent transmission line model should be identical to the propagation constant $\gamma$ of the original MIS interconnect.
- The complex time-averaged power traveling down the equivalent circuit is required to be equal to the complex time-averaged power traveling down the original MIS interconnect.

By imposing the above requirements, it can be shown that

$$Z = \gamma \frac{2P(z)}{|I(z)|^2} \tag{A.4a}$$

$$\frac{1}{Y} = \frac{1}{\gamma} \frac{2P(z)}{|I(z)|^2} \tag{A.4b}$$

where $P(z)$ denotes the complex time-averaged power traveling down the original MIS interconnect, and $I(z)$ is the current flowing through the signal line. They can be computed by

$$I(z) = \iint_{(x,y)\in \text{signal line}} \mathbf{J} \cdot \hat{\mathbf{z}}\, dxdy = wH_y\Big|_{x=-h_d} \tag{A.5a}$$

$$P(z) = \frac{1}{2T}\int_0^T \left\{ \iint_{(x,y)\in S} \left[\mathbf{E}\times\mathbf{H}^*\right]\cdot \hat{\mathbf{z}}\ dxdy \right\} dt \tag{A.5b}$$

where $T = 2\pi/\omega$, $S = [-h_d, h_c]\times[0, w]$ and $\mathbf{J}$ is the current density.

Denote

$$E_0(z) = E_x\Big|_{x=-h_d} = Ae^{-\gamma z} \tag{A.6}$$

Substitution of (A.2a), (A.2b), (A.2c) and (A.2d) in (A.5a) and (A.5b) leads to

$$I(z) = \frac{j\omega\tilde{\varepsilon}_1 w}{\gamma} E_0(z) \tag{A.7a}$$

$$P(z) = \frac{\gamma K_d}{j2\omega\tilde{\varepsilon}_1 w}\left|I(z)\right|^2 + \frac{\gamma K_c}{j2\omega\tilde{\varepsilon}_2 w}\left|Q\right|^2\left|I(z)\right|^2 \tag{A.7b}$$

where $Q = \cos(k_1 h_d)/\cos(k_2 h_c)$ and the positive real constants $K_d$ and $K_c$ are given by

$$\begin{aligned} K_d &= \int_{-h_d}^{0} \left|\cos[k_1(x+h_d)]\right|^2 dx \\ &= \frac{1}{2}\left\{\frac{\sin[2\operatorname{Re}(k_1)h_d]}{2\operatorname{Re}(k_1)} + \frac{\sinh[2\operatorname{Im}(k_1)h_d]}{2\operatorname{Im}(k_1)}\right\} \end{aligned} \tag{A.8a}$$

$$\begin{aligned} K_c &= \int_0^{h_c} \left|\cos\left[k_2\left(x-h_c\right)\right]\right|^2 dx \\ &= \frac{1}{2}\left\{\frac{\sin\left[2\operatorname{Re}\left(k_2\right)h_c\right]}{2\operatorname{Re}\left(k_2\right)} + \frac{\sinh\left[2\operatorname{Im}\left(k_2\right)h_c\right]}{2\operatorname{Im}\left(k_2\right)}\right\} \end{aligned} \tag{A.8b}$$

Note that (A.7a) has been exploited during the evaluation of (A.7b).

The first term in (A.7b) is due to the power flowing in the insulator layer, whereas the second term represents the contribution from the power flowing in the semiconductor layer. Note that $K_d \approx h_d$ as $\left|k_1 h_d\right| << 1$ and $K_c \approx h_c$ as $\left|k_2 h_c\right| << 1$. Hence, $K_d$ and $K_c$ can be defined as equivalent thickness of the insulator layer and the semiconductor layer respectively.

Based on (A.4a), (A.4b), and (A.7b), one can write $Z = \left(R_0 + j\omega L_0\right) + \left(R_s + j\omega L_s\right)$ and $\frac{1}{Y} = \frac{1}{G_0 + j\omega C_0} + \frac{1}{G_s + j\omega C_s}$ and assign

$$\begin{aligned} R_0 + j\omega L_0 &= \frac{K_d}{j\omega\tilde{\varepsilon}_1 w}\gamma^2, & \frac{1}{G_0 + j\omega C_0} &= \frac{K_d}{j\omega\tilde{\varepsilon}_1 w} \\ R_s + j\omega L_s &= \frac{K_c\left|Q\right|^2}{j\omega\tilde{\varepsilon}_2 w}\gamma^2, & \frac{1}{G_s + j\omega C_s} &= \frac{K_c\left|Q\right|^2}{j\omega\tilde{\varepsilon}_2 w} \end{aligned} \tag{A.9}$$

Then, one obtains

$$R_0 = \frac{2\alpha\beta K_d}{\omega\varepsilon_1 w},\ G_0 = 0,\ L_0 = \frac{K_d}{\varepsilon_1 w}\frac{\left(\beta^2-\alpha^2\right)}{\omega^2},\ C_0 = \frac{\varepsilon_1 w}{K_d} \tag{A.10a}$$

$$R_s = \frac{K_c\left|Q\right|^2}{\left|\tilde{\varepsilon}_2\right|^2 w}\frac{\left[2\alpha\beta\varepsilon_2 - \left(\beta^2-\alpha^2\right)\frac{\sigma_2}{\omega}\right]}{\omega}, \qquad G_s = \frac{\sigma_2 w}{K_c\left|Q\right|^2} \tag{A.10b}$$

$$L_s = \frac{K_c|Q|^2}{|\tilde{\varepsilon}_2|^2 w} \frac{\left[\left(\beta^2 - \alpha^2\right)\varepsilon_2 + 2\alpha\beta\frac{\sigma_2}{\omega}\right]}{\omega^2}, \quad C_s = \frac{\varepsilon_2 w}{K_c|Q|^2} \tag{A.10c}$$

Therefore, one obtains a linearized version of the equivalent transmission line model for MIS interconnects (see Figure 4.3). Circuit elements $R_0$, $L_0$, and $C_0$ are, respectively, the resistance, inductance, and capacitance per unit length due to electromagnetic field in the insulator layer, whereas circuit elements $R_s$, $L_s$, $C_s$, and $G_s$ denote the resistance, inductance, capacitance, and conductance per unit length due to electromagnetic field in the semiconductor substrate respectively. Circuit element $R_c$ denotes the resistance per unit length over the signal line, which is not studied here since the signal line has been treated as an ideal conductor.

Note that $R_0$ is nonzero even if the insulator medium is lossless. Equation (A.10a) implies that $R_0 \to 0$ as $\alpha \to 0$. Hence, the existence of nonzero $R_0$ is an indirect consequence of the semiconductor loss, which impacts on the electromagnetic field in the insulator layer.

When the semiconductor loss is small, i.e., the ratio $f/\sigma_2$ is large, the semiconductor acts like a dielectric. In the practical situation of $\varepsilon_1 h_d << \varepsilon_2 h_c$, most of the wave energy propagates in the semiconductor layer with the velocity nearly equal to $1/\sqrt{\varepsilon_2}$ times the light velocity in vacuum, i.e., $\beta \approx \omega\sqrt{\mu_0\varepsilon_2}$. Moreover, one has $|k_2| \to 0$, $Q \approx 1$, $K_d \approx h_d$, $K_c \approx h_c$, and $\alpha << \beta$. Hence, the new model specified by (A.10a), (A.10b), and (A.10c) reduces to the dielectric quasi-TEM circuit model presented in [6] at this limit.

## A.3: SUMMARY

An analytical model of MIS interconnects has been presented using the uniform conductivity model and the energy-based approach. The uniform conductivity model simplified the semiconductor description and resulted in a pure electromagnetic problem. A linearized model of MIS interconnects was obtained by solving such a pure electromagnetic problem. At the quasi-TEM limit, this linearized model reduces to the existing model that was obtained using the contour integral based approach. Nevertheless, this analytical model provides no knowledge about some important effects caused by field-carrier interactions such as nonlinearity, electronic controllability, and screening effect of charged carriers.

# APPENDIX B: A SAMPLE PROPHET SCRIPT FILE

A sample PROPHET script file is shown below to illustrate usage of the newly created physical operators, derivative nodal operator, and scalar field feature during device level frequency domain (DLFD) simulation and electromagnetic analysis. This script is able to compute the propagation factor as well as the electromagnetic fields and carrier concentrations for the static solution, the fundamental mode, the second harmonic, and the third harmonic.

**A SAMPLE PROPHET SCRIPT FILE**

```
system name=static_equation
+ sysvars=psi,electrons,holes,Exr0
+ tmpvars=ncr01,ncj01,ncr0,ncj0
+ nterm=8
+  term0=dirichlet.em_device_dirichlet(netdope|psi,electrons,holes)
       @{anode/oxide,silicon/cathode}
+  term1=box_div.lapflux(psi|psi)@{silicon,oxide}
+  term2=nodal.potflux(electrons,holes,netdope|psi)@{silicon}
+  term3=box_div.drift_diffusion(psi,electrons|electrons)@{silicon}
+  term4=box_div.drift_diffusion(psi,holes|holes)@{silicon}
+  term5=nodal.self(Exr0|Exr0)@{silicon}
+  term6=dnodal.deriv_x(psi|Exr0)@{silicon}
+  term7=constraint.continuity(psi|psi)@{silicon/oxide}
+ nfunc=2
+  func0=cmplx_diff(holes,zero,electrons,zero|ncr01,ncj01)@{silicon}
+  func1=cmplx_sum(ncr01,ncj01,netdope,zero|ncr0,ncj0)@{silicon}

system name=pure_em_equations
+ sysvars=Ezr,Ezj,Exr,Exj,Hyr,Hyj,alfa,beta,pwr,pwj
+ tmpvars=sgmr,sgmj
+ nterm=16
+  term0=-1*box_div.lapflux(Ezr|Ezr)@{silicon}
+  term1=-1*box_div.lapflux(Ezj|Ezj)@{silicon}
+  term2=volume.em_prop(Ezr,Ezj,alfa,beta,sgmr,sgmj|Ezr,Ezj)@{silicon}
+  term3=volume.em_prop(Exr,Exj,alfa,beta,sgmr,sgmj|Exr,Exj)@{silicon}
+  term4=dnodal.em_field_Ex_1d(Ezr,Ezj,alfa,beta|Exr,Exj)@{silicon}
```

```
+  term5=-1*volume.self(Hyr|Hyr)@{silicon}
+  term6=-1*volume.self(Hyj|Hyj)@{silicon}
+  term7=dnodal.em_field_Hy_prop(Ezr,Ezj,Exr,Exj,alfa,beta|Hyr,Hyj)
         @{silicon}
+  term8=dirichlet.default_dirichlet(0|Ezr,Ezj)@{silicon/cathode}
+  term9=dirichlet.em_dirichlet_1d(Ezr,Ezj,Hyr,Hyj,alfa,beta,sgmr,sgmj
          |Ezr,Ezj)@{silicon/oxide}
+  term10=interface.em_cal_eigen_1d(Ezr,Ezj,Hyr,Hyj,alfa,beta|alfa,
          beta)@{silicon/oxide}
+  term11=volume.copy(zero|alfa)@{silicon}
+  term12=volume.copy(zero|beta)@{silicon}
+  term13=volume.em_power(Exr,Exj,Hyr,Hyj|pwr,pwj)@{silicon}
+  term14=-1*volume.self(pwr|pwr)@{silicon}
+  term15=-1*volume.self(pwj|pwj)@{silicon}
+ nfunc=1
+  func0=em_conductivity(electrons,zero,holes,zero|sgmr,sgmj)@{silicon}

system name=first_mode
+ sysvars=Ezr,Ezj,Exr,Exj,Hyr,Hyj,alfa,beta,nr,nj,pr,pj,Jnxr3,Jnxj3,
          Jpxr3,Jpxj3,pwr,pwj
+ tmpvars=Jnzr3,Jnzj3,Jpzr3,Jpzj3,Jnxr1,Jnxj1,Jpxr1,Jpxj1,Jnxr2,Jnxj2,
          Jpxr2,Jpxj2,Jnxr,Jnxj,Jpxr,Jpxj,Jnzr,Jnzj,Jpzr,Jpzj,Jnxrt,
          Jnxjt,Jpxrt,Jpxjt,ncr,ncj,unr,unj,upr,upj,Jzr,Jzj,Jxr,Jxj,
          sgmr,sgmj
+ nterm=37
+  term0=-1*box_div.lapflux(Ezr|Ezr)@{silicon}
+  term1=-1*box_div.lapflux(Ezj|Ezj)@{silicon}
+  term2=volume.em_prop(Ezr,Ezj,alfa,beta,sgmr,sgmj|Ezr,Ezj)@{silicon}
+  term3=volume.em_source_prop(Jzr,Jzj,ncr,ncj,alfa,beta|Ezr,Ezj)
         @{silicon}
+  term4=volume.em_prop(Exr,Exj,alfa,beta,sgmr,sgmj|Exr,Exj)@{silicon}
+  term5=dnodal.em_field_Ex_1d(Ezr,Ezj,alfa,beta,Jxr,Jxj|Exr,Exj)
         @{silicon}
+  term6=-1*volume.self(Hyr|Hyr)@{silicon}
+  term7=-1*volume.self(Hyj|Hyj)@{silicon}
+  term8=dnodal.em_field_Hy_prop(Ezr,Ezj,Exr,Exj,alfa,beta|Hyr,Hyj)
         @{silicon}
+  term9=dirichlet.default_dirichlet(0|Ezr,Ezj)@{silicon/cathode}
+  term10=dirichlet.em_dirichlet_1d(Ezr,Ezj,Hyr,Hyj,alfa,beta,sgmr,sgmj
          |Ezr,Ezj)@{silicon/oxide}
+  term11=interface.em_cal_eigen_1d(Ezr,Ezj,Hyr,Hyj,alfa,beta
          |alfa,beta)@{silicon/oxide}
+  term12=volume.copy(zero|alfa)@{silicon}
+  term13=volume.copy(zero|beta)@{silicon}
+  term14=box_div.em_dix_xy(nr,nj|nr,nj)@{silicon}
+  term15=volume.em_carrier_prop(nr,nj,Jnzr3,Jnzj3,unr,unj,alfa,beta
          |nr,nj)@{silicon}
+  term16=dnodal.em_carrier_field0(nr,nj,zero,zero,alfa,beta|nr,nj)
          @{silicon}
```

```
+  term17=dnodal.em_carrier_field(electrons,zero,ncr,ncj,Exr,Exj
          |nr,nj)@{silicon}
+  term18=dnodal.em_carrier_field(nr,nj,ncr0,ncj0,Exr0,zero|nr,nj)
          @{silicon}
+  term19=box_div.em_dix_xy(pr,pj|pr,pj)@{silicon}
+  term20=volume.em_carrier_prop(pr,pj,Jpzr3,Jpzj3,upr,upj,alfa,beta
          |pr,pj)@{silicon}
+  term21=dnodal.em_carrier_field0(pr,pj,zero,zero,alfa,beta|pr,pj)
          @{silicon}
+  term22=dnodal.em_carrier_field(holes,zero,ncr,ncj,Exr,Exj|pr,pj)
          @{silicon}
+  term23=dnodal.em_carrier_field(pr,pj,ncr0,ncj0,Exr0,zero|pr,pj)
          @{silicon}
+  term24=dirichlet.default_dirichlet(0|nr,nj,pr,pj)@{silicon/cathode}
+  term25=-1*interface.em_third_kind(Jnxr1,Jnxj1,Jnxr2,Jnxj2,zero,zero
          |nr,nj)@{silicon/oxide}
+  term26=-1*interface.em_third_kind(Jpxr1,Jpxj1,Jpxr2,Jpxj2,zero,zero
          |pr,pj)@{silicon/oxide}
+  term27=-1*volume.self(Jnxr3|Jnxr3)@{silicon}
+  term28=-1*volume.self(Jnxj3|Jnxj3)@{silicon}
+  term29=-1*volume.self(Jpxr3|Jpxr3)@{silicon}
+  term30=-1*volume.self(Jpxj3|Jpxj3)@{silicon}
+  term31=dnodal.em_dix_x(nr,nj|Jnxr3,Jnxj3)@{silicon}
+  term32=dnodal.em_dix_x(pr,pj|Jpxr3,Jpxj3)@{silicon}
+  term33=interface.em_boundary_Ex_1d(Exr,Exj,alfa,beta|Exr,Exj)
          @{silicon/oxide}
+  term34=volume.em_power(Exr,Exj,Hyr,Hyj|pwr,pwj)@{silicon}
+  term35=-1*volume.self(pwr|pwr)@{silicon}
+  term36=-1*volume.self(pwj|pwj)@{silicon}
+ nfunc=20
+  func0=cmplx_diff(pr,pj,nr,nj|ncr,ncj)@{silicon}
+  func1=em_drift0(electrons,zero,Exr,Exj|Jnxr1,Jnxj1)@{silicon}
+  func2=em_drift0(holes,zero,Exr,Exj|Jpxr1,Jpxj1)@{silicon}
+  func3=em_drift(nr,nj,Exr0,zero|Jnxr2,Jnxj2)@{silicon}
+  func4=em_drift(pr,pj,Exr0,zero|Jpxr2,Jpxj2)@{silicon}
+  func5=cmplx_sum(Jnxr2,Jnxj2,Jnxr3,Jnxj3|Jnxr,Jnxj)@{silicon}
+  func6=cmplx_sum(Jpxr2,Jpxj2,Jpxr3,Jpxj3|Jpxr,Jpxj)@{silicon}
+  func7=cmplx_sum(Jnxr1,Jnxj1,Jnxr,Jnxj|Jnxrt,Jnxjt)@{silicon}
+  func8=cmplx_sum(Jpxr1,Jpxj1,Jpxr,Jpxj|Jpxrt,Jpxjt)@{silicon}
+  func9=em_drift_dix_prop(nr,nj,zero,zero,alfa,beta|Jnzr,Jnzj)
         @{silicon}
+  func10=em_drift_dix_prop(pr,pj,zero,zero,alfa,beta|Jpzr,Jpzj)
          @{silicon}
+  func11=cmplx_sum(Jnxr,Jnxj,Jpxr,Jpxj|Jxr,Jxj)@{silicon}
+  func12=cmplx_sum(Jnzr,Jnzj,Jpzr,Jpzj|Jzr,Jzj)@{silicon}
+  func13=em_conductivity(electrons,zero,holes,zero|sgmr,sgmj)
          @{silicon}
+  func14=400*self(pr|unr)@{silicon}
+  func15=400*self(pj|unj)@{silicon}
```

```
+  func16=400*self(pr|upr)@{silicon}
+  func17=400*self(pj|upj)@{silicon}
+  func18=em_dix_prop(nr,nj,alfa,beta|Jnzr3,Jnzj3)@{silicon}
+  func19=em_dix_prop(pr,pj,alfa,beta|Jpzr3,Jpzj3)@{silicon}

system name=second_mode
+ sysvars=E2zr,E2zj,E2xr,E2xj,H2yr,H2yj,n2r,n2j,p2r,p2j,J2nxr3,J2nxj3,
          J2pxr3,J2pxj3,pw2r,pw2j
+ tmpvars=J2nzr3,J2nzj3,J2pzr3,J2pzj3,J2nxr1,J2nxj1,J2pxr1,J2pxj1,
          J2nxr2,J2nxj2,J2pxr2,J2pxj2,J2nxr,J2nxj,J2pxr,J2pxj,J2nzr,
          J2nzj,J2pzr,J2pzj,J2nxrt,J2nxjt,J2pxrt,J2pxjt,n2cr,n2cj,u2nr,
          u2nj,u2pr,u2pj,J2zr,J2zj,J2xr,J2xj
+ nterm=35
+  term0=-1*box_div.lapflux(E2zr|E2zr)@{silicon}
+  term1=-1*box_div.lapflux(E2zj|E2zj)@{silicon}
+  term2=volume.em_prop(E2zr,E2zj,alfa,beta,sgmr,sgmj|E2zr,E2zj)
         @{silicon}
+  term3=volume.em_source_prop(J2zr,J2zj,n2cr,n2cj,alfa,beta|E2zr,E2zj)
         @{silicon}
+  term4=volume.em_prop(E2xr,E2xj,alfa,beta,sgmr,sgmj|E2xr,E2xj)
         @{silicon}
+  term5=dnodal.em_field_Ex_1d(E2zr,E2zj,alfa,beta,J2xr,J2xj|E2xr,E2xj)
         @{silicon}
+  term6=-1*volume.self(H2yr|H2yr)@{silicon}
+  term7=-1*volume.self(H2yj|H2yj)@{silicon}
+  term8=dnodal.em_field_Hy_prop(E2zr,E2zj,E2xr,E2xj,alfa,beta
         |H2yr,H2yj)@{silicon}
+  term9=dirichlet.default_dirichlet(0|E2zr,E2zj)
         @{silicon/cathode,silicon/oxide}
+  term10=box_div.em_dix_xy(n2r,n2j|n2r,n2j)@{silicon}
+  term11=volume.em_carrier_prop(n2r,n2j,J2nzr3,J2nzj3,u2nr,u2nj,alfa,
          beta|n2r,n2j)@{silicon}
+  term12=dnodal.em_carrier_field0(nr,n2r,nj,n2j,zero,Ezr,zero,Ezj,
          alfa,beta|n2r,n2j)@{silicon}
+  term13=dnodal.em_carrier_field(electrons,zero,n2cr,n2cj,E2xr,E2xj
          |n2r,n2j)@{silicon}
+  term14=dnodal.em_carrier_field(nr,nj,ncr,ncj,Exr,Exj|n2r,n2j)
          @{silicon}
+  term15=dnodal.em_carrier_field(n2r,n2j,ncr0,ncj0,Exr0,zero|n2r,n2j)
          @{silicon}
+  term16=box_div.em_dix_xy(p2r,p2j|p2r,p2j)@{silicon}
+  term17=volume.em_carrier_prop(p2r,p2j,J2pzr3,J2pzj3,u2pr,u2pj,alfa,
          beta|p2r,p2j)@{silicon}
+  term18=dnodal.em_carrier_field0(pr,p2r,pj,p2j,zero,Ezr,zero,Ezj,
          alfa,beta|p2r,p2j)@{silicon}
+  term19=dnodal.em_carrier_field(holes,zero,n2cr,n2cj,E2xr,E2xj
          |p2r,p2j)@{silicon}
+  term20=dnodal.em_carrier_field(pr,pj,ncr,ncj,Exr,Exj|p2r,p2j)
          @{silicon}
```

```
+  term21=dnodal.em_carrier_field(p2r,p2j,ncr0,ncj0,Exr0,zero|p2r,p2j)
          @{silicon}
+  term22=dirichlet.default_dirichlet(0|n2r,n2j,p2r,p2j)
          @{silicon/cathode}
+  term23=-1*interface.em_third_kind(J2nxr1,J2nxj1,J2nxr2,J2nxj2,zero,
          zero|n2r,n2j)@{silicon/oxide}
+  term24=-1*interface.em_third_kind(J2pxr1,J2pxj1,J2pxr2,J2pxj2,zero,
          zero|p2r,p2j)@{silicon/oxide}
+  term25=-1*volume.self(J2nxr3|J2nxr3)@{silicon}
+  term26=-1*volume.self(J2nxj3|J2nxj3)@{silicon}
+  term27=-1*volume.self(J2pxr3|J2pxr3)@{silicon}
+  term28=-1*volume.self(J2pxj3|J2pxj3)@{silicon}
+  term29=dnodal.em_dix_x(n2r,n2j|J2nxr3,J2nxj3)@{silicon}
+  term30=dnodal.em_dix_x(p2r,p2j|J2pxr3,J2pxj3)@{silicon}
+  term31=interface.em_boundary_Ex_1d(E2xr,E2xj,alfa,beta,E2zr,E2zj
          |E2xr,E2xj)@{silicon/oxide}
+  term32=volume.em_power(E2xr,E2xj,H2yr,H2yj|pw2r,pw2j)@{silicon}
+  term33=-1*volume.self(pw2r|pw2r)@{silicon}
+  term34=-1*volume.self(pw2j|pw2j)@{silicon}
+ nfunc=19
+  func0=cmplx_diff(p2r,p2j,n2r,n2j|n2cr,n2cj)@{silicon}
+  func1=em_drift0(electrons,zero,E2xr,E2xj|J2nxr1,J2nxj1)@{silicon}
+  func2=em_drift0(holes,zero,E2xr,E2xj|J2pxr1,J2pxj1)@{silicon}
+  func3=em_drift(nr,n2r,nj,n2j,Exr0,Exr,zero,Exj|J2nxr2,J2nxj2)
         @{silicon}
+  func4=em_drift(pr,p2r,pj,p2j,Exr0,Exr,zero,Exj|J2pxr2,J2pxj2)
         @{silicon}
+  func5=cmplx_sum(J2nxr2,J2nxj2,J2nxr3,J2nxj3|J2nxr,J2nxj)@{silicon}
+  func6=cmplx_sum(J2pxr2,J2pxj2,J2pxr3,J2pxj3|J2pxr,J2pxj)@{silicon}
+  func7=cmplx_sum(J2nxr1,J2nxj1,J2nxr,J2nxj|J2nxrt,J2nxjt)@{silicon}
+  func8=cmplx_sum(J2pxr1,J2pxj1,J2pxr,J2pxj|J2pxrt,J2pxjt)@{silicon}
+  func9=em_drift_dix_prop(nr,n2r,nj,n2j,zero,Ezr,zero,Ezj,alfa,beta
         |J2nzr,J2nzj)@{silicon}
+  func10=em_drift_dix_prop(pr,p2r,pj,p2j,zero,Ezr,zero,Ezj,alfa,beta
          |J2pzr,J2pzj)@{silicon}
+  func11=cmplx_sum(J2nxr,J2nxj,J2pxr,J2pxj|J2xr,J2xj)@{silicon}
+  func12=cmplx_sum(J2nzr,J2nzj,J2pzr,J2pzj|J2zr,J2zj)@{silicon}
+  func13=400*self(p2r|u2nr)@{silicon}
+  func14=400*self(p2j|u2nj)@{silicon}
+  func15=400*self(p2r|u2pr)@{silicon}
+  func16=400*self(p2j|u2pj)@{silicon}
+  func17=em_dix_prop(n2r,n2j,alfa,beta|J2nzr3,J2nzj3)@{silicon}
+  func18=em_dix_prop(p2r,p2j,alfa,beta|J2pzr3,J2pzj3)@{silicon}

system name=third_mode
+ sysvars=E3zr,E3zj,E3xr,E3xj,H3yr,H3yj,n3r,n3j,p3r,p3j,J3nxr3,J3nxj3,
          J3pxr3,J3pxj3,pw3r,pw3j
+ tmpvars=J3nzr3,J3nzj3,J3pzr3,J3pzj3,J3nxr1,J3nxj1,J3pxr1,J3pxj1,
          J3nxr2,J3nxj2,J3pxr2,J3pxj2,J3nxr,J3nxj,J3pxr,J3pxj,J3nzr,
```

```
          J3nzj,J3pzr,J3pzj,J3nxrt,J3nxjt,J3pxrt,J3pxjt,n3cr,n3cj,u3nr,
          u3nj,u3pr,u3pj,J3zr,J3zj,J3xr,J3xj
+ nterm=37
+  term0=-1*box_div.lapflux(E3zr|E3zr)@{silicon}
+  term1=-1*box_div.lapflux(E3zj|E3zj)@{silicon}
+  term2=volume.em_prop(E3zr,E3zj,alfa,beta,sgmr,sgmj|E3zr,E3zj)
         @{silicon}
+  term3=volume.em_source_prop(J3zr,J3zj,n3cr,n3cj,alfa,beta|E3zr,E3zj)
         @{silicon}
+  term4=volume.em_prop(E3xr,E3xj,alfa,beta,sgmr,sgmj|E3xr,E3xj)
         @{silicon}
+  term5=dnodal.em_field_Ex_1d(E3zr,E3zj,alfa,beta,J3xr,J3xj|E3xr,E3xj)
         @{silicon}
+  term6=-1*volume.self(H3yr|H3yr)@{silicon}
+  term7=-1*volume.self(H3yj|H3yj)@{silicon}
+  term8=dnodal.em_field_Hy_prop(E3zr,E3zj,E3xr,E3xj,alfa,beta
         |H3yr,H3yj)@{silicon}
+  term9=dirichlet.default_dirichlet(0|E3zr,E3zj)
         @{silicon/cathode,silicon/oxide}
+  term10=box_div.em_dix_xy(n3r,n3j|n3r,n3j)@{silicon}
+  term11=volume.em_carrier_prop(n3r,n3j,J3nzr3,J3nzj3,u3nr,u3nj,alfa,
          beta|n3r,n3j)@{silicon}
+  term12=dnodal.em_carrier_field0(nr,n2r,n3r,nj,n2j,n3j,zero,Ezr,E2zr,
          zero,Ezj,E2zj,alfa,beta|n3r,n3j)@{silicon}
+  term13=dnodal.em_carrier_field(electrons,zero,n3cr,n3cj,E3xr,E3xj
          |n3r,n3j)@{silicon}
+  term14=dnodal.em_carrier_field(nr,nj,n2cr,n2cj,E2xr,E2xj|n3r,n3j)
          @{silicon}
+  term15=dnodal.em_carrier_field(n2r,n2j,ncr,ncj,Exr,Exj|n3r,n3j)
          @{silicon}
+  term16=dnodal.em_carrier_field(n3r,n3j,ncr0,ncj0,Exr0,zero|n3r,n3j)
          @{silicon}
+  term17=box_div.em_dix_xy(p3r,p3j|p3r,p3j)@{silicon}
+  term18=volume.em_carrier_prop(p3r,p3j,J3pzr3,J3pzj3,u3pr,u3pj,alfa,
          beta|p3r,p3j)@{silicon}
+  term19=dnodal.em_carrier_field0(pr,p2r,p3r,pj,p2j,p3j,zero,Ezr,E2zr,
          zero,Ezj,E2zj,alfa,beta|p3r,p3j)@{silicon}
+  term20=dnodal.em_carrier_field(holes,zero,n3cr,n3cj,E3xr,E3xj
          |p3r,p3j)@{silicon}
+  term21=dnodal.em_carrier_field(pr,pj,n2cr,n2cj,E2xr,E2xj|p3r,p3j)
          @{silicon}
+  term22=dnodal.em_carrier_field(p2r,p2j,ncr,ncj,Exr,Exj|p3r,p3j)
          @{silicon}
+  term23=dnodal.em_carrier_field(p3r,p3j,ncr0,ncj0,Exr0,zero|p3r,p3j)
          @{silicon}
+  term24=dirichlet.default_dirichlet(0|n3r,n3j,p3r,p3j)
          @{silicon/cathode}
+  term25=-1*interface.em_third_kind(J3nxr1,J3nxj1,J3nxr2,J3nxj2,zero,
          zero|n3r,n3j)@{silicon/oxide}
```

```
+  term26=-1*interface.em_third_kind(J3pxr1,J3pxj1,J3pxr2,J3pxj2,zero,
          zero|p3r,p3j)@{silicon/oxide}
+  term27=-1*volume.self(J3nxr3|J3nxr3)@{silicon}
+  term28=-1*volume.self(J3nxj3|J3nxj3)@{silicon}
+  term29=-1*volume.self(J3pxr3|J3pxr3)@{silicon}
+  term30=-1*volume.self(J3pxj3|J3pxj3)@{silicon}
+  term31=dnodal.em_dix_x(n3r,n3j|J3nxr3,J3nxj3)@{silicon}
+  term32=dnodal.em_dix_x(p3r,p3j|J3pxr3,J3pxj3)@{silicon}
+  term33=interface.em_boundary_Ex_1d(E3xr,E3xj,alfa,beta,E3zr,E3zj
          |E3xr,E3xj)@{silicon/oxide}
+  term34=volume.em_power(E3xr,E3xj,H3yr,H3yj|pw3r,pw3j)@{silicon}
+  term35=-1*volume.self(pw3r|pw3r)@{silicon}
+  term36=-1*volume.self(pw3j|pw3j)@{silicon}
+ nfunc=19
+  func0=cmplx_diff(p3r,p3j,n3r,n3j|n3cr,n3cj)@{silicon}
+  func1=em_drift0(electrons,zero,E3xr,E3xj|J3nxr1,J3nxj1)@{silicon}
+  func2=em_drift0(holes,zero,E3xr,E3xj|J3pxr1,J3pxj1)@{silicon}
+  func3=em_drift(nr,n2r,n3r,nj,n2j,n3j,Exr0,Exr,E2xr,zero,Exj,E2xj
         |J3nxr2,J3nxj2)@{silicon}
+  func4=em_drift(pr,p2r,p3r,pj,p2j,p3j,Exr0,Exr,E2xr,zero,Exj,E2xj
         |J3pxr2,J3pxj2)@{silicon}
+  func5=cmplx_sum(J3nxr2,J3nxj2,J3nxr3,J3nxj3|J3nxr,J3nxj)@{silicon}
+  func6=cmplx_sum(J3pxr2,J3pxj2,J3pxr3,J3pxj3|J3pxr,J3pxj)@{silicon}
+  func7=cmplx_sum(J3nxr1,J3nxj1,J3nxr,J3nxj|J3nxrt,J3nxjt)@{silicon}
+  func8=cmplx_sum(J3pxr1,J3pxj1,J3pxr,J3pxj|J3pxrt,J3pxjt)@{silicon}
+  func9=em_drift_dix_prop(nr,n2r,n3r,nj,n2j,n3j,zero,Ezr,E2zr,zero,
         Ezj,E2zj,alfa,beta|J3nzr,J3nzj)@{silicon}
+  func10=em_drift_dix_prop(pr,p2r,p3r,pj,p2j,p3j,zero,Ezr,E2zr,zero,
          Ezj,E2zj,alfa,beta|J3pzr,J3pzj)@{silicon}
+  func11=cmplx_sum(J3nxr,J3nxj,J3pxr,J3pxj|J3xr,J3xj)@{silicon}
+  func12=cmplx_sum(J3nzr,J3nzj,J3pzr,J3pzj|J3zr,J3zj)@{silicon}
+  func13=400*self(p3r|u3nr)@{silicon}
+  func14=400*self(p3j|u3nj)@{silicon}
+  func15=400*self(p3r|u3pr)@{silicon}
+  func16=400*self(p3j|u3pj)@{silicon}
+  func17=em_dix_prop(n3r,n3j,alfa,beta|J3nzr3,J3nzj3)@{silicon}
+  func18=em_dix_prop(p3r,p3j,alfa,beta|J3pzr3,J3pzj3)@{silicon}

# add parameter for memory management
dbase prefix=library/math
dbase create name=memory.size ival=60

# add parameter for static_equation
dbase prefix=library/math/systems/static_equation/math.static_equation
             /pde
dbase create name=method sval="direct"
dbase create name=maxNewton ival=2000

# add parameter for pure_em_equations
```

```
dbase prefix=library/math/systems/zero_mode/math.zero_mode/pde
dbase create name=method sval="direct"
dbase create name=maxNewton ival=500
dbase create name=harmonic_order ival=1
dbase create name=initialize_eigen ival=1

# add parameter for first_mode
dbase prefix=library/math/systems/first_mode/math.first_mode/pde
dbase create name=method sval="direct"
dbase create name=maxNewton ival=20000
dbase create name=NewtonMaxUpd rval=1.0e36
dbase create name=NewtonUpd rval=1e-5
dbase create name=harmonic_order ival=1
dbase create name=initialize_eigen ival=0

# add parameter for second_mode
dbase prefix=library/math/systems/second_mode/math.second_mode/pde
dbase create name=method sval="direct"
dbase create name=maxNewton ival=2000
dbase create name=NewtonMaxUpd rval=1.0e36
dbase create name=NewtonUpd rval=1e-5
dbase create name=harmonic_order ival=2

# add parameter for third_mode
dbase prefix=library/math/systems/third_mode/math.third_mode/pde
dbase create name=method sval="direct"
dbase create name=maxNewton ival=2000
dbase create name=NewtonMaxUpd rval=1.0e72
dbase create name=NewtonUpd rval=1e-5
dbase create name=harmonic_order ival=3

# add general physics parameters
dbase prefix=library/physics
dbase create name=frequency rval=5.0e3
dbase create name=magnitude rval=1.0e-6

# create new names to database
dbase prefix=library/physics/silicon
dbase createlist name=Exr0
dbase createlist name=Ezr
dbase createlist name=Ezj
[Here, the 'dbase createlist' commands for Exr, Exj, Hyr, Hyj,
 alfa, beta, nr, nj, pr, pj, Jnxr3, Jnxj3, Jpxr3, Jpxj3, pwr, pwj,
 E2zr, E2zj, E2xr, E2xj, H2yr, H2yj, n2r, n2j, p2r, p2j, J2nxr3,
 J2nxj3, J2pxr3, J2pxj3, pw2r, pw2j, E3zr, E3zj, E3xr, E3xj, H3yr,
 H3yj, n3r, n3j, p3r, p3j, J3nxr3, J3nxj3, J3pxr3, J3pxj3, pw3r, and
 pw3j are omitted for conciseness]

# create background and scale settings
```

```
dbase create name=electrons/background rval=1e4
dbase create name=electrons/scale rval=1.e14
dbase create name=holes/background rval=0
dbase create name=holes/scale rval=1.e-4
dbase create name=Exr0/background rval=0
dbase create name=Exr0/scale rval=1.e-5
dbase create name=Ezr/background rval=0
dbase create name=Ezr/scale rval=1.e-15
dbase create name=Ezj/background rval=0
dbase create name=Ezj/scale rval=1.e-15
[Here, the ‘background’ and ‘scale’ settings for Exr, Exj, Hyr, Hyj,
 alfa, beta, nr, nj, pr, pj, Jnxr3, Jnxj3, Jpxr3, Jpxj3, pwr, pwj,
 E2zr, E2zj, E2xr, E2xj, H2yr, H2yj, n2r, n2j, p2r, p2j, J2nxr3,
 J2nxj3, J2pxr3, J2pxj3, pw2r, pw2j, E3zr, E3zj, E3xr, E3xj, H3yr,
 H3yj, n3r, n3j, p3r, p3j, J3nxr3, J3nxj3, J3pxr3, J3pxj3, pw3r, and
 pw3j are omitted for conciseness]

# add physics parameters related to silicon
dbase prefix=library/physics/silicon
dbase create name=psi/Dix sval="11.9*8.85418e-12*1.0e6"
dbase create name=electrons/mobility sval="1500*1e8"
dbase create name=electrons/Dix sval="1500*1e8*kTq"
dbase create name=electrons/collision_time sval="2.2156e-7"
dbase create name=holes/mobility sval="450*1e8"
dbase create name=holes/Dix sval="450*1e8*kTq"
dbase create name=holes/collision_time sval="5.2706e-8"
dbase create name=nr/mobility sval="1500*1e8"
dbase create name=nr/Dix sval="1500*1e8*kTq"
dbase create name=nr/collision_time sval="2.2156e-7"
dbase create name=pr/mobility sval="450*1e8"
dbase create name=pr/Dix sval="450*1e8*kTq"
dbase create name=pr/collision_time sval="5.2706e-8"
dbase create name=permittivity rval=11.9
dbase create name=permeability rval=1
dbase prefix=library/physics/silicon/Ezr
dbase create name=Dix rval=1
dbase prefix=library/physics/silicon/Ezj
dbase create name=Dix rval=1
dbase prefix=library/physics/silicon/Exr
dbase create name=Dix rval=1
dbase prefix=library/physics/silicon/Exj
dbase create name=Dix rval=1
dbase prefix=library/physics/silicon/nr
dbase create name=esign rval=-1
dbase prefix=library/physics/silicon/pr
dbase create name=esign rval=1
[Here, the parameters settings for E2zr, E2zj, E2xr, E2xj, n2r, n2j,
 p2r, p2j, E3zr, E3zj, E3xr, E3xj, n3r, n3j, p3r, and p3j are omitted
 for conciseness]
```

```
# add physics parameters related to oxide
dbase prefix=library/physics/oxide
dbase create name=psi/Dix sval="3.9*8.85418e-12*1.0e6"
dbase create name=ni-sze rval=0.0

# add boundary conditions and boundary parameters
dbase prefix=library/physics/silicon
dbase create name=Ezr/permittivity1.oxide rval=3.9
dbase create name=Ezr/permeability1.oxide rval=1
dbase create name=Ezr/thickness1.oxide rval=0.05
dbase create name=Ezr/permittivity2.oxide rval=11.9
dbase create name=Ezr/permeability2.oxide rval=1
dbase create name=Ezr/thickness2.oxide rval=100
dbase create name=Ezr/dirichlet.cathode rval=0
dbase create name=Ezj/dirichlet.cathode rval=0
dbase create name=Exr/permittivity1.oxide rval=3.9
dbase create name=Exr/permeability1.oxide rval=1
dbase create name=Exr/thickness1.oxide rval=0.05
dbase create name=Exr/permittivity2.oxide rval=11.9
dbase create name=Hyr/permittivity1.oxide rval=3.9
dbase create name=Hyr/permeability1.oxide rval=1
dbase create name=Hyr/thickness1.oxide rval=0.05
dbase create name=Hyr/permittivity2.oxide rval=11.9
dbase create name=electrons/permittivity1.oxide rval=3.9
dbase create name=electrons/permeability1.oxide rval=1
dbase create name=electrons/thickness1.oxide rval=0.05
dbase create name=electrons/permittivity2.oxide rval=11.9
dbase create name=holes/permittivity1.oxide rval=3.9
dbase create name=holes/permeability1.oxide rval=1
dbase create name=holes/thickness1.oxide rval=0.05
dbase create name=holes/permittivity2.oxide rval=11.9
dbase create name=nr/dirichlet.cathode rval=0
dbase create name=nj/dirichlet.cathode rval=0
dbase create name=pr/dirichlet.cathode rval=0
dbase create name=pj/dirichlet.cathode rval=0
[Here, the boundary parameters settings for E2zr, E2zj, E2xr, E2xj,
 H2yr, H2yj, n2r, n2j, p2r, p2j, E3zr, E3zj, E3xr, E3xj, H3yr, H3yj,
 n3r, n3j, p3r, and p3j are omitted for conciseness]

# mesh description
grid mat=silicon xloc=0,0.001,0.01,0.1,1,10,100
                 xdel=0.00001,0.00005,0.0005,0.005,0.05,0.5,5
deposit mat=oxide thick=0.05 xdel=0.002

# boundary specification
boundary xmin=-0.05 xmax=-0.05 name=anode
boundary xmin=100.0 xmax=100.0 name=cathode
```

```
# impurity concentration specification
field set=netdope val="1e17"

# field initial setting
field set=zero value=0
field set=alfa type=scalar value=0.000
field set=beta type=scalar value=0.0065
field set=Ezr  value=1e-15
field set=Ezj  value=1e-15
[Here, the 'field' initial settings for Exr, Exj, Hyr, Hyj, nr, nj,
 pr, pj, Jnxr3, Jnxj3, Jpxr3, Jpxj3, E2zr, E2zj, E2xr, E2xj, H2yr,
 H2yj, n2r, n2j, p2r, p2j, J2nxr3, J2nxj3, J2pxr3, J2pxj3, E3zr, E3zj,
 E3xr, E3xj, H3yr, H3yj, n3r, n3j, p3r, p3j, J3nxr3, J3nxj3, J3pxr3,
 And J3pxj3 are omitted for conciseness]

# scalar field initial setting
field set=alfa type=scalar value=0.000
field set=beta type=scalar value=0.0065
field set=pwr  type=scalar value=0.00
field set=pwj  type=scalar value=0.00
field set=pw2r type=scalar value=0.00
field set=pw2j type=scalar value=0.00
field set=pw3r type=scalar value=0.00
field set=pw3j type=scalar value=0.00

# solve the static equations
bias initial system=static_equation temper=27
bias system=static_equation voltage=0.1 elec=anode temper=27

# solve the pure EM problem based on the uniform conductivity model
solve system=pure_em_equations
save pas=output/power0_v0.pas_0.1p
dump solution outf=output/power0_v0.out_0.1p

# solve the fundamental mode equations
solve system=first_mode
save pas=output/power1_v0.pas_0.1p
dump solution outf=output/power1_v0.out_0.1p

# solve the second harmonic equations
solve system=second_mode
save pas=output/power2_v0.pas_0.1p
dump solution outf=output/power2_v0.out_0.1p

# solve the third harmonic equations
solve system=third_mode
save pas=output/power3_v0.pas_0.1p
dump solution outf=output/power3_v0.out_0.1p
```

```
# graphic plotting for some variables
graph elem=psi  log=0 ymin=-2   ymax=2
graph elem=Exr0 log=0 ymin=-8   ymax=2

graph new.window elem=netdope   log=1 ymin=15 ymax=18
graph elem=electrons log=1 ymin=1  ymax=18
graph elem=holes     log=1 ymin=1  ymax=18

graph new.window elem=Hyr  log=0 ymin=-4e-9   ymax=4e-9
graph elem=Hyj  log=0 ymin=-4e-9   ymax=4e-9
graph elem=Ezr  log=0 ymin=-4e-9   ymax=4e-9
graph elem=Ezj  log=0 ymin=-4e-9   ymax=4e-9
graph elem=Exr  log=0 ymin=-4e-9   ymax=4e-9
graph elem=Exj  log=0 ymin=-4e-9   ymax=4e-9

graph new.window elem=nr   log=1 ymin=1 ymax=10
graph elem=nj   log=1 ymin=1 ymax=10
graph elem=pr   log=1 ymin=1 ymax=10
graph elem=pj   log=1 ymin=1 ymax=10
```

# APPENDIX C: DATA STRUCTURES FOR CIRCUIT MODEL EXTRACTION PROGRAM

In this appendix, data structures for the circuit model extraction program are enclosed. The circuit model extraction program can extract the equivalent linear and nonlinear circuit elements from the device level frequency domain (DLFD) simulation results as well as compute the equivalent linear circuit elements based on the uniform conductivity model.

```
class MISBaseParam
{
  // calculate basic parameters such as wave number, equivalent
  // thickness, etc.
  public:

    struct layer_info_s
    {
        Real    thick;     // thickness of the layer
        Complex epsilon;   // permittivity of the layer
        Real    mu;        // permeability of the layer
        Real    freq;      // operating frequency
        Complex gamma;     // propagation factor
    };

    typedef struct layer_info_s *layer_info;

    MISBaseParam(layer_info info);

    ~MISBaseParam();

    Complex& GetWaveNum() { return wave_num; }
    Real GetEqvThick() { return eqv_thick; }

  protected:

    layer_info info;
```

```
    Real omega;
    Complex wave_num;
    Real eqv_thick;

  private:

    void init();

    void calcWaveNum();
    void calcEqvThick();
};
```

```
class MISLayer : public MISBaseParam
{
  // calculate common parts of circuit parameters using
  // the energy based method for each individual layer
  public:

    MISLayer(MISBaseParam::layer_info info);

    ~MISLayer();

    virtual int DoExtraction();

    Real GetR() { return res; }
    Real GetL() { return ind; }
    Real GetG() { return cond; }
    Real GetC() { return cap; }

  private:

    int calcRLCG();

    Real res, ind, cond, cap;
};
```

```
class MISWaveNumAndZ0
{
  // calculate line parameters such as propogation constant,
  // characterization impedance, etc.
  public:

    MISWaveNumAndZ0(Real freq, Real C, Real L, Real R = 0.0,
                            Real G = 0.0);

    ~MISWaveNumAndZ0();
```

```

    Complex& GetWaveNum() { return wave_num; }
    Complex& GetZ0() { return char_imp; }
    Real GetFreeSpaceWaveNum() { return wave_num0; }

  private:

    Real freq, C, L, R, G;
    Complex wave_num;
    Complex char_imp;
    Real wave_num0;

    void calc();
};
```

```
class MISInsulator
{
  // calculate R0, L0, C0, and G0 using the energy based method
  public:

    struct insul_info_s
    {
        Real    width;     // width of signal line
        Real    thick_d;   // thickness of dielectric layer
        Complex epsilon_d; // permittivity of dielectric layer
        Real    mu_d;      // permeability of dielectric layer
        Real    freq;      // operating frequency
        Complex gamma;     // propagation factor
    };

    typedef struct insul_info_s *insul_info;

    MISInsulator(insul_info info);
    MISInsulator() { this->info = 0; }

    ~MISInsulator();

    void SetInfo(insul_info info);

    virtual int DoExtraction();

    Real GetR0() { return res0; }
    Real GetL0() { return ind0; }
    Real GetG0() { return cond0; }
    Real GetC0() { return cap0; }

    Complex& GetWaveNum() { return kd; }
    Real GetEqvThick() { return eqv_thick; }
```

```
  private:

    insul_info info;

    Real res0, ind0, cond0, cap0;

    Complex kd;
    Real eqv_thick;
};
```

```
class MISSemicond
{
  // calculate Rs, Ls, Cs, and Gs using the energy based method and
  // uniform conductivity model
  public:

    struct semicond_info_s
    {
        Real    width;     // width of signal line
        Real    thick_c;   // thickness of semiconductor layer
        Complex epsilon_c; // permittivity of semiconductor layer
        Real    mu_c;      // permeability of semiconductor layer
        Complex sigma_c;   // conductivity of semiconductor layer
        Real    freq;      // operating frequency
        Complex gamma;     // propagation factor
    };

    typedef struct semicond_info_s *semicond_info;

    MISSemicond(semicond_info info);
    MISSemicond() { this->info = 0; }

    ~MISSemicond();

    void SetInfo(semicond_info info);

    virtual int DoExtraction();

    Real GetR() { return res; }
    Real GetL() { return ind; }
    Real GetG() { return cond; }
    Real GetC() { return cap; }

    Complex& GetWaveNum() { return kc; }
    Real GetEqvThick() { return eqv_thick; }

  private:
```

```
    semicond_info info;

    Real res, ind, cond, cap;

    Complex kc;
    Real eqv_thick;
};
```

```
class MISCircuit : public MISInsulator
{
  // main routines: perform device level modeling and compute
  // linear and nonlinear circuit parameters R0, L0, C0, G0,
  // Rs, Ls, Cs, and Gs
  public:

    struct mis_info_s
    {
        Real    width;     // width of signal line
        Real    thick_d;   // thickness of dielectric layer
        Real    epsilon_d; // permittivity of dielectric layer
        Real    mu_d;      // permeability of dielectric layer
        Real    thick_c;   // thickness of semiconductor layer
        Real    freq;      // operating frequency
        Complex gamma;     // propagation factor
        int     m;         // total number of harmonics
        Complex *power;    // normalized power for each harmonic
    };

    typedef struct mis_info_s *mis_info;

    MISCircuit(mis_info info);

    ~MISCircuit();

     int DoExtraction();

     Real *GetRs() { return res; }
     Real *GetLs() { return ind; }
     Real *GetGs() { return cond; }
     Real *GetCs() { return cap; }

     Real GetRs(int m) { return res[m-1]; }
     Real GetLs(int m) { return ind[m-1]; }
     Real GetGs(int m) { return cond[m-1]; }
     Real GetCs(int m) { return cap[m-1]; }

  protected:
```

```
    mis_info info;

    int calcRLGC();

  private:

    Real res0, ind0, cap0;
    Real *res, *ind, *cond, *cap;

    Real omega;
    Real cur_mag;

    void init();

    void calcCurrentMag();
};
```

```
class MISCircuit0
{
  // build equivalent linear circuit model using the energy
  // based method and uniform conductivity model
  public:

    struct mis0_info_s
    {
        Real    width;     // width of signal line
        Real    thick_d;   // thickness of dielectric layer
        Complex epsilon_d; // permittivity of dielectric layer
        Real    mu_d;      // permeability of dielectric layer
        Real    thick_c;   // thickness of semiconductor layer
        Complex epsilon_c; // permittivity of semiconductor layer
        Real    mu_c;      // permeability of semiconductor layer
        Real    n0;        // electron density
        Real    p0;        // hole density
        Real    mob_n;     // electron mobility
        Real    mob_p;     // hole mobility
        Real    tao_n;     // electron relaxation time
        Real    tao_p;     // hole relaxation time
        Real    freq;      // operating frequency
    };

    typedef struct mis0_info_s *mis0_info;

    MISCircuit0(mis0_info info);
    MISCircuit0() { this->info = 0; }

    ~MISCircuit0();
```

```
    void SetInfo(mis0_info info);

    virtual int DoExtraction();

    Real GetR0() { return res0; }
    Real GetL0() { return ind0; }
    Real GetG0() { return cond0; }
    Real GetC0() { return cap0; }

    Real GetR() { return res; }
    Real GetL() { return ind; }
    Real GetG() { return cond; }
    Real GetC() { return cap; }

    Complex& GetPropFac() { return gamma; }
    Real GetQFac() { return qfac; }

    Complex& GetInsulWaveNum() { return kd; }
    Real GetInsulEqvThick() { return eqv_thick_d; }
    Complex& GetSemicondWaveNum() { return kc; }
    Real GetSemicondEqvThick() { return eqv_thick_c; }

    void CalcEMFieldInSemicond(FILE *coord, FILE *field = 0);

  private:

    mis0_info info;

    Real res0, ind0, cond0, cap0;
    Real res, ind, cond, cap;

    Complex sigma_c;   // conductivity of semiconductor layer
    Complex gamma;     // propagation factor
    Real    qfac;      // square of magnitude of Q factor

    Complex kd;
    Real eqv_thick_d;
    Complex kc;
    Real eqv_thick_c;

    void init();

    void calcSigma();
    void calcPropFac();
    void calcQFac();
};
```

# BIBLIOGRAPHY

[1] H. B. Bakoglu, *Circuits, Interconnections and Packaging for VLSI*. Addison-Wesley Publishing Co., Reading, MA, 1990.

[2] D. C. Edelstein, G. A. Sai-Halasz, Y. Mii, “VLSI on-chip interconnection performance simulations and measurements,” *IBM J. Res. Develop.*, vol.39, pp.383-401, July 1995.

[3] T. M. Hyltin, “Microstrip transmission on semiconductor dielectrics,” *IEEE Trans. Microwave Theory Tech.*, vol.MTT-13, pp.777-781, Nov. 1965.

[4] H. Guckel, P. A. Brennan, and I. Palocz, “A parallel-plate wave-guide approach to micro-miniaturized planar transmission lines for integrated circuits,” *IEEE Trans. Microwave Theory Tech.*, vol.MTT-15, pp.468-476, Aug. 1967.

[5] H. Hasegawa, M. Furukawa, and H. Yanai, “Slow wave propagation along a microstrip line on Si-SiO2 system,” *Proc. IEEE* (Lett.), vol.59, pp.297-299, Feb. 1971.

[6] H. Hasegawa, M. Furukawa, and H. Yanai, “Properties of microstrip line on Si-SiO2 system,” *IEEE Trans. Microwave Theory Tech.*, vol.MTT-19, pp.869-881, Nov. 1971.

[7] J. M. Jaffe, “A high-frequency variable delay line,” *IEEE Trans. Electron Devices*, vol.ED-19, pp.1292-1294, Dec. 1972.

[8] D. Jager and W. Rabus “Bias dependent phase delay of Schottky contact microstrip lines,” *Electron. Lett.*, vol.9, no.9, pp.201-203, 1973.

[9] D. Jager, W. Rabus, and W. Eichkoff, “Bias dependent small-signal parameters of Schottky contact microstrip lines,” *Solid-State Electron.*, vol.17, pp.777-783, 1974.

[10] G. W. Hughes and R. M. White, “Microwave properties of nonlinear MIS and Schottky-barrier microstrip,” *IEEE Trans. Electron Devices*, vol.ED-22, pp.945-956, Oct. 1975.

[11] D. Jager, "Slow-wave propagation along variable Schottky-contact microstrip line," *IEEE Trans. Microwave Theory Tech.*, vol.MTT-24, pp.566-573, Sept. 1976.

[12] H. Hasegawa and H. Okizaki, “M.I.S. and Schottky slow-wave coplanar stripline on GaAs substrates,” *Electron. Lett.*, vol.13, no.22, pp.663-664, 1977.

[13] P. Kennis and L. Faucon, "Rigorous analysis of planar M.I.S. transmission lines," *Electron. Lett.*, vol.17, no.13, pp.454-456, 1981.

[14] Y. Fukuoka and T. Itoh, “Analysis of slow-wave phenomena in coplanar waveguide on a semiconductor substrate,” *Electron. Lett.*, vol.18, no.14, pp.589-590, July 1982.

[15] V. M. Hietala, Y. R. Kwon, and K. S. Champlin, “Low-loss slow-wave propagation along a microstructure transmission line on a silicon surface,” *Electron. Lett.*, vol.22, no.14, pp.755-756, July 1986.

[16] K. Wu, “New prospective coplanar metal-insulator-semiconductor (MIS) monolithic structure,” *Electron. Lett.*, vol.24, no.5, pp.262-264, March 1988.

[17] K. Goossen and R. B. Hammond, “Modeling of picosecond pulse propagation in microstrip interconnections on integrated circuits,” *IEEE Trans. Microwave Theory Tech.*, vol.MTT-37, pp.469-478, March 1989.

[18] K. Wu and R. Vahldieck, “Propagation characteristics of MIS transmission lines with inhomogeneous doping profile,” *IEEE Trans. Microwave Theory Tech.*, vol.MTT-38, pp.1872-1878, Dec. 1990.

[19] S. Zaage and E. Grotelushen “Characterization of the broadband transmission behavior of interconnections on silicon substrates,” *IEEE Trans. Components, Hybrids, Manufact. Tech. (Part B),* vol.16, pp.686-691, Nov. 1993.

[20] E. Groteluschen, L. S. Dutta, and S. Zaage, “Quasi-analytical analysis of the broadband properties of multiconductor transmission lines on semiconductor substrates,” *IEEE Trans. Components, Hybrids, Manufact. Tech. (Part B)*, vol.17, pp.376-382, Aug. 1994.

[21] V. Milanovic, M. Ozgur, D. C. Degroot, J. A. Hargon, M. Gaitan, and M. E. Zaghloul, “Characterization of broadband transmission for coplanar waveguides on CMOS silicon substrates,” *IEEE Trans. Microwave Theory Tech.*, vol.MTT-46, pp.632-640, May 1998.

[22] R. E. Neidert and C. M. Krone, “Voltage variable microwave phase shifter,” *Electron. Lett.*, vol.21, pp.626-628, 1985.

[23] J. Margarshack, “A new digital phase shifter architecture suitable for MMIC’s,” *IEEE Trans. Microwave Theory Tech.*, vol.MTT-42, pp.154-156, Jan. 1994.

[24] S. G. Ingram and J. C. Clifton, “The use of active travelling-wave structures in GaAs MMIC’s,” *IEEE Trans. Microwave Theory Tech.*, vol.MTT-44, pp.956-960, June 1996.

[25] S. Sali, “Modeling of resistive and geometrical discontinuities in microstrip interconnections on integrated circuits,” *Proc. IEE*, vol.137, pt. H, no.5, pp.893-897, May 1990.

[26] J. K. Wee, Y. J. Park, H. S. Min, D. H. Cho, M. H. Seung, and H. S. Park, “Modeling the substrate effect in interconnect line characteristics of high-speed VLSI circuits,” *IEEE Trans. Microwave Theory Tech.*, vol.MTT-46, pp.1436-1443, Oct. 1998.

[27] C. Seguinot, P. Kennis, P. Pribetich, J. F. Legier, “Analytical model of the Schottky contact coplanar line,” *Proc. 14th European Microwave Conference*, pp.160-165, Sept. 1984.

[28] D. F. Williams, “Metal-insulator-semiconductor transmission lines,” *IEEE Trans. Microwave Theory Tech.*, vol.MTT-47, pp.176-181, Feb. 1999.

[29] Y. Fukuoka and T. Itoh, "Analysis of slow-wave phenomena in coplanar waveguide on a semiconductor substrate," *Electron. Lett.*, vol.18, pp.589-590, July 1982.

[30] Y. Fukuoka, Y. Shih, and T. Itoh, “Analysis of slow-wave coplanar waveguide for monolithic integrated circuits,” *IEEE Trans. Microwave Theory Tech.*, vol.MTT-31, pp.567-573, July 1983.

[31] R. Sorrentino, G. Leuzzi, and A. Silbermann, “Characteristics of metal-insulator-semiconductor coplanar waveguide for monolithic microwave circuits,” *IEEE Trans. Microwave Theory Tech.*, vol.MTT-32, pp.410-416, Oct. 1984.

[32] T. G. Livernois and P. B. Katehi, “A generalized method for deriving the space-domain Green’s function in a shielded, multilayer substrate structure with applications to MIS transmission lines,” *IEEE Trans. Microwave Theory Tech.*, vol.MTT-37, pp.1761-1767, Nov. 1989.

[33] J. P. K. Gilb and C. A. Balanis, “MIS slow-wave structures over a wide range of parameters,” *IEEE Trans. Microwave Theory Tech.*, vol.MTT-40, pp.2148-2154, Dec. 1992.

[34] J. C. Liou and K. M. Lau, “Analysis of slow-wave transmission lines on multi-layered semiconductor structures including conductor loss,” *IEEE Trans. Microwave Theory Tech.*, vol.MTT-41, pp.814-829, May 1993.

[35] K. Wu and R. Vahldieck, “Hybrid-mode analysis of homogeneously and inhomogeneously doped low-loss slow-wave coplanar transmission lines,” *IEEE Trans. Microwave Theory Tech.*, vol.MTT-39, pp.1348-1360, Aug. 1991.

[36] S. Chen, R. Vahldieck, and J. Huang, “Rigorous analysis of mode propagation and field scattering in silicon-based coplanar MIS slow wave structures with abrupt transitions to transmission lines on normal substrate,” *IEEE Trans. Microwave Theory Tech.*, vol.MTT-44, pp.2487-2494, May 1996.

[37] T. Shibata and E. Sano, “Characterization of MIS structure coplanar transmission lines for investigation of signal propagation in integrated circuits,” *IEEE Trans. Microwave Theory Tech.*, vol.MTT-38, pp.881-890, July 1990.

[38] M. Aubourg, J. Villotte, F. Godon, and Y. Garault, “Finite element analysis of lossy waveguide – applications to microstrip lines on semiconductor substrate,” *IEEE Trans. Microwave Theory Tech.*, vol.MTT-31, pp.326-330, April 1983.

[39] C. Tzuang and T. Itoh, “Finite element analysis of slow-wave Schottky contact printed lines,” *IEEE Trans. Microwave Theory Tech.*, vol.MTT-34, pp.1483-1489, Dec. 1986.

[40] J. J. Kucera and R. J. Gutmann, "Effect of finite metallization and inhomogeneous dopings on slow-wave-mode propagation," *IEEE Trans. Microwave Theory Tech.*, vol.MTT-45, pp.1807-1810, Oct. 1997.

[41] C. M. Krowne and G. B. Tait, “Propagation in layered biased semiconductor structures based on transport analysis,” *IEEE Trans. Microwave Theory Tech.*, vol.MTT-37, pp.711-722, April 1989.

[42] K. Han and T. T. Y. Wong, “Space-charge wave considerations in MIS waveguide analysis,” *IEEE Trans. Microwave Theory Tech.*, vol.MTT-39, pp.1126-1132, July 1991.

[43] Y. R. Kwon, V. M. Hietala, and K. S. Champlin, “Quasi-TEM analysis of slow-wave mode propagation on coplanar microstructure MIS transmission lines,” *IEEE Trans. Microwave Theory Tech.*, vol.MTT-35, pp.545-551, June 1987.

[44] J. R. Brews, “Transmission line models for lossy waveguide interconnections in VLSI,” *IEEE Trans. Electron. Devices,* vol. ED-33, pp. 1356-1365, Sept. 1986.

[45] J. A. Stratton, *Electromagnetic Theory*. NY: McGraw-Hill, 1941.

[46] R. E. Collin, *Field Theory of Guided Waves,* 2nd edition. NY: IEEE Press, 1991.

[47] S. Ramo, J. R. Whinnery, and T. Van Duzer, *Fields and Waves in Communication Electronics*, 3rd edition. NY: John Wiley & Sons, 1994.

[48] R. F. Harrington, *Time-Harmonic Electromagnetic Fields*. NY: McGraw-Hill, 1961.

[49] C. A. Balanis, *Advanced Engineering Electromagnetics*. NY: John Wiley & Sons, 1989.

[50] S. M. Sze, *Physics of Semiconductor Devices*, $2^{nd}$ edition. NY: John Wiley & Sons, 1981.

[51] S. Selberherr, *Analysis and Simulation of Semiconductor Devices*. NY: Springer-Verlag, 1984.

[52] R. W. Dutton and Z. Yu, *Technology CAD – Computer Simulation of IC Processes and Devices*. Boston, MA: Kluwer AcademicPublishers, 1993.

[53] K. D. Paulsen and D. R. Lynch, “Elimination of vector parasites in finite element Maxwell solutions,” *IEEE Trans. Microwave Theory Tech.*, vol.MTT-39, pp.395-404, March 1991.

[54] C. W. Crowley, P. P. Silvester, and H. Hurwitz, “Covariant projection elements for 3D vector field problems,” *IEEE Trans. Magnetics*, vol.MAG-24, pp.397-400, 1988.

[55] K. Ise, K. Inoue, and M. Koshiba, “Three-dimensional finite-element solution of dielectric scattering obstacles in a rectangular waveguide,” *IEEE Trans. Microwave Theory Tech.*, vol.MTT-38, pp.1352-1329, Sept. 1990.

[56] J. Jin, *The Finite Element Method in Electromagnetics*. NY: John Wiley & Sons, 1993.

[57] C. Bender and S. Orszag, *Advanced Mathematical Methods for Engineers*. NY: McGraw-Hill, 1978.

[58] E. Zauderer, *Partial Differential Equations of Applied Mathematics*, $2^{nd}$ edition. NY: John Wiley & Sons, 1989.

[59] T. J. R. Hughes, *The Finite Element Method: Linear Static and Dynamic Finite Element Analysis*. Englewood Cliffs, NJ: Prentice-Hall, 1987.

[60] O. C. Zienkiewicz and R. L. Taylor, *The Finite Element Method*, 4th edition. NY: McGraw-Hill, 1989.

[61] D. S. Burnett, *Finite Element Analysis, From Concepts to Applications*. Reading, MA: Addison-Wesley, 1987.

[62] R. D. Cook, *Concepts and Applications of Finite Element Analysis*. NY: John Wiley & Sons, 1981.

[63] K. H. Huebner, *The Finite Element Method for Engineers*. NY: John Wiley & Sons, 1975.

[64] F. S. Acton, *Numerical Methods That Works*. Washington: Mathematical Association of America, 1970.

[65] J. Ortega and W. Rheinboldt, *Iterative Solution of Nonlinear Equations in Several Variables*. NY: Academic Press, 1970.

[66] J. E. Dennis and R. B. Schnabel, *Numerical Methods for Unconstrained Optimization and Nonlinear Equations*. Englewood Cliffs, NJ: Prentice-Hall, 1983.

[67] G. H. Golub and C. F. Van Loan, *Matrix Computations*, 3rd edition. Baltimore, MD: Johns Hopkins University Press, 1996.

[68] R. P. Tewarson, *Sparse Matrices*. NY: Academic Press, 1973.

[69] D. E. Knuth, *The Art of Computer Programming*. Reading, MA: Addison-Wesley, 1968.

[70] J. R. Bunch and D. J. Rose, *Sparse Matrix Computations*. NY: Academic Press, 1976.

[71] A. R. Djordjevic, T. K. Sarkar, and G. F. Harrington, “Time-domain response of multiconductor transmission lines,” *Proc. IEEE*, vol.75, pp.743-764, June 1987.

[72] J. E. Schutt-Aine and R. Mittra, “Nonlinear transient analysis of coupled transmission lines,” *IEEE Trans. Circuits Syst.*, vol.36, pp.959-967, July 1989.

[73] T. Dhaene, L. Martens, and D. D. Zutter, "Transient simulation of arbitrary nonuniform interconnection structures characterized by scattering parameters," *IEEE Trans. Circuits Syst.*, vol.39, pp.928-937, Nov. 1992.

[74] G. W. Pan, G. Wang, and B. K. Gilbert, "Analysis of nonlinear termination networks for coupled lossy and dispersive transmission lines," *IEEE Trans. Microwave Theory Tech.*, vol.MTT-41, pp.531-535, March 1993.

[75] R. Griffith, E. Chiprount, Q. J. Zhang, and M. S. Nakhla, "A CAD framework for simulation and optimization of high-speed VLSI interconnects," *IEEE Trans. Circuits Syst.*, vol.39, pp.893-906, Nov. 1992.

[76] E. C. Chang and S. M. Kang, "Computationally efficient simulation of a lossy transmission line with skin effect by using numerical inversion of Laplace transform," *IEEE Trans. Circuits Syst.*, vol.39, pp.861-868, Nov. 1992.

[77] R. Griffith and M. S. Nakhla, "Time-domain analysis of lossy coupled transmission lines," *IEEE Trans. Microwave Theory Tech.*, vol.MTT-38, pp.1480-1487, Oct. 1990.

[78] L. T. Pillage and R. A. Rohrer, "Asymptotic waveform evaluation for timing analysis," *IEEE Trans. Computer-Aided Design*, vol.9, pp.352-366, April 1990.

[79] J. E. Bracken, V. Raghavan, and R. A. Rohrer, "Interconnect simulation with asymptotic waveform evaluation (AWE)," *IEEE Trans. Circuits Syst.*, vol.39, pp. 869-878, Nov. 1992.

[80] T. K. Tang and M. S. Nakhla, "Analysis of high speed VLSI interconnects using the asymptotic waveform evaluation technique," *IEEE Trans. Computer-Aided Design*, vol.11, pp.341-352, March 1992.

[81] V. Raghavan, and R. A. Rohrer, "AWESpice: A general tool for the efficient and accurate simulation of interconnect problems," *29th Proc. ACM/IEEE Design Automation Conference*, pp.87-92, 1992.

[82] S. Lin and E. S. Kuh, “Transient simulation of lossy interconnects based on the recursive convolution formulation,” *IEEE Trans. Circuits Syst.*, vol.39, pp.879-892, Nov. 1992.

[83] F. Y. Chang, “Transient simulation of nonuniform coupled lossy transmission lines characterized with frequency-dependent parameters, part II: discrete-time analysis,” *IEEE Trans. Circuits Syst.*, vol.39, pp.907-927, Nov. 1992.

[84] F. Fallside and D. T. Bickley, “Nonlinear delay line with constant characteristic impedance,” *Proc. IEE*, vol.113, pp.263-270, Feb. 1966.

[85] S. K. Mullick, “Propagation of signals in nonlinear transmission lines,” *IBM J. Res. Develop.*, vol.11, pp.558-562, Sept. 1967.

[86] M. M. Turner, G. Branch, and P. W. Smith, “Methods of theoretical analysis and computer modeling of the shaping of electrical pulses by nonlinear transmission lines and lumped-element delay lines,” *IEEE Trans. Electron Devices*, vol.ED-38, pp.810-816, April 1991.

[87] C. S. Rafferty and R. K. Smith, “Solving partial differential equations with the PROPHET simulator,” Technical Report, Bell Laboratories, Lucent Technologies, December 1997.

[88] J. R. Munkres, *Analysis on Manifolds*. MA: Addison-Wesley, 1991.

[89] T. B. A. Senior, “Impedance boundary conditions for imperfectly conducting surface,” *Appl. Sci. Res. B*, vol.8, pp.418-436, 1960.

[90] J. J. H. Wang, *Generalized Moment Methods in Electromagnetics: Formulation and Computer Solution of Integral Equations*. NY: John Wiley & Sons, 1991.